arXiv:2510.14656v2 [stat.ML] 21 Jun 2026

Inverse Problem for Partial Differential Equations with Jump Discontinuities in Coefficients by Two-stage Physics-Informed Deep Learning and Statistical Mixture Models

Zhikun Zhang[a,b], Guanyu Pan[c,f], Xiangjun Wang[b], Yong Xu[a,e], Guangtao Zhang[d,f,*]

[a] *School of Mathematics and Statistics, Northwestern Polytechnical University, Xi'an 710072, China*

[b] *School of Mathematics and Statistics, Huazhong University of Science and Technology, Wuhan 430074, China*

[c] *School of Mathematics and Computational Science, Xiangtan University, Xiangtan 411105, China*

[d] *Department of Ocean Science and Engineering and Center for Complex Flows and Soft Matter Research, Southern University of Science and Technology, Guangdong 518055, China*

[e] *MOE Key Laboratory for Complexity Science in Aerospace, Northwestern Polytechnical University, Xi'an, 710072, China*

[f] *SandGold AI Research, Guangzhou 510642, China*

Abstract

Inverse problems involving partial differential equations (PDEs) with discontinuous coefficients arise widely in the modeling of complex spatiotemporal systems with uncertain dynamics and heterogeneous structures. Their solution remains challenging primarily because the unknown coefficient fields may exhibit abrupt temporal or spatial transitions, together with additional difficulties arising from non-smoothness, nonlinearity, and high dimensionality. This work proposes a two-stage physics-informed deep learning framework that combines neural-network-based sampling with statistical inference and constrained parameter refinement. In the first stage, a dual-network physics-informed architecture is used, where a main-network approximates the PDE solution and an auxiliary coefficient sub-network provides a relaxed continuous soft approximation of the true discontinuous coefficient field. A gradient-adaptive weighting strategy is incorporated to improve residual training and enhance sampling reliability near possible discontinuity regions. The sampled coefficient values are then analyzed using Bayesian learning for Gaussian mixture models and birth-death Markov chain model selection, which identify the number of coefficient regimes and provide candidate intervals for coefficient values and transition regions. In the second stage, the inverse problem is reformulated as a constrained physics-informed estimator, in which the coefficient is replaced by a form-consistent hard approximation explicitly represented as a piecewise-constant function over the spatiotemporal domain. Comprehensive numerical experiments on PDEs with jump-discontinuous coefficients demonstrate that the proposed framework achieves adapt-

*Corresponding author

Email addresses: zhikunzhang@nwpu.edu.cn (Zhikun Zhang), tao@sgd-ai.com (Guangtao Zhang)

ability and accurate parameter identification with acceptable computational costs compared to existing methods. Applications to solution reconstruction further illustrate its practical potential. This work provides a generalizable computational approach for inverse problems governed by PDEs with discontinuous parameter structures, particularly in non-stationary and heterogeneous systems.

Keywords: Partial Differential Equation, Inverse problem, Parameter identification, Jump-varying coefficient, Physics-informed neural networks, Gaussian mixture model, Markov chain Monte Carlo

---

Contents

1 Introduction **3**

2 Methodology **6**

2.1 Mathematical Setup 7

2.2 Neural-Network Based Sampler 9

2.3 Statistical Mixture Modeling 11

2.4 Constrained Parameter Refinement 14

3 Numerical Examples **17**

3.1 Wave Equation 19

3.2 Heat Equation 25

3.3 Burgers' Equation 28

3.4 Navier-Stokes Equation 35

3.5 Helmholtz Equation 41

4 Ablation Study of Neural Networks **47**

5 Comparison with Existing Algorithms **50**

5.1 Bayesian and Neural Networks 50

5.2 Statistical Clustering Learning 54

6 Physical Field Reconstruction **58**

7 Robustness with Observation Noise **61**

8 Limitations **65**

9 Conclusion and Discussion **66**

---

1. Introduction

Partial differential equations (PDEs) provide a fundamental framework for modeling spatiotemporal physical processes in science and engineering. In many applications, the coefficients in these equations encode material properties, transport rates, source effects, or medium-dependent parameters, and they often need to be inferred from indirect observations [1, 2]. The inverse identification of such coefficients becomes especially difficult when they vary over space and time, and the difficulty is further amplified when they contain abrupt changes or jump discontinuities. Such discontinuities lead to non-smooth parameter fields and localized transition regions, which may manifest as temporal change points, spatial interfaces, or more general spatiotemporal discontinuity sets in heterogeneous media [3, 4, 5].

Such scenarios arise in a wide range of PDE models and application domains. For example, in wave and Helmholtz equations, coefficients determine propagation speeds or medium properties, and discontinuities may correspond to layered media, inclusions, or material interfaces [6, 7, 8, 9, 10]. Heat and diffusion equations may involve discontinuous thermal conductivities or diffusivities [11, 12], while fluid and transport models may contain spatially or temporally varying viscosity, diffusivity, or source terms [13, 14]. Similar issues arise in geophysical, biological, environmental, and material systems, where effective parameters may vary across spatial sub-domains or time intervals [15, 16, 17, 18]. In these settings, the solution field may remain relatively smooth even when the underlying coefficient field is non-smooth, making coefficient recovery from state data ill-conditioned. Therefore, accurately identifying both stable coefficient values and discontinuity locations from limited observations is a central task in PDE inverse problems with heterogeneous or regime-dependent parameters. This motivates the present focus on PDE coefficients that are piecewise constant or nearly piecewise constant over spatiotemporal domains.

Classical parameter-identification methods for PDEs include regularized optimization, reduced-order modeling, and Bayesian inference. Output least-squares formulations combined with Tikhonov regularization have been used to recover conductivity or diffusion parameters [19]. Reduced-basis and model-reduction techniques can accelerate repeated forward solves and Gauss-Newton iterations in inverse PDE problems [20, 21]. Bayesian and hierarchical inference methods provide a probabilistic framework for parameter estimation and can be combined with Markov chain Monte Carlo, stochastic collocation, or sparse Bayesian learning techniques [22, 23, 24]. These methods have achieved substantial progress, but their implementation may become expensive or sensitive to discretization, prior modeling, and regularization choices when the unknown coefficient field is high-dimensional, discontinuous, or only indirectly observed. These considerations motivate data-assisted approaches that combine observational information with physical constraints.

Recently, Physics-informed neural networks (PINNs) have recently emerged as a mesh-free, data-assisted framework for PDE forward and inverse problems by penalizing the residuals of the governing

equations together with data and boundary losses [25]. PINNs have been widely used for solution approximation and inverse parameter estimation from sparse data [26]. Subsequent developments have improved their stability and expressiveness through adaptive activation functions [27], gradient-enhanced formulations [28], constrained architectures [29], and residual or self-adaptive weighting strategies [30, 31, 32, 33]. For inverse problems with variable coefficients, additional network components or branch-network structures have also been introduced to approximate coefficient functions and to address the mismatch between the dimensionality of the unknown coefficient and that of the solution field [34, 35, 36, 37]. These methods provide useful tools for learning smoothly varying coefficients from data, but their performance may deteriorate when the target coefficient contains sharp jump discontinuities.

Despite these advances, discontinuous coefficient identification remains difficult for standard PINNs and existing variable-coefficient extensions. Conversely, a purely discrete parameterization requires prior knowledge of the number of regimes and the approximate locations of change points or interfaces, which are usually unavailable. As a result, the plateau values of piecewise-constant coefficients may be biased, and the corresponding change points or spatial interfaces may be inaccurately localized. Adaptive weighting can improve training stability, but it does not by itself convert a smooth coefficient approximation into a discontinuous representation. Conversely, a purely discrete parameterization requires prior knowledge of the number of regimes and the approximate locations of change points or interfaces, which are usually unavailable. These observations motivate a framework that combines continuous neural approximation, statistical regime extraction, and constrained discontinuous-parameter refinement.

This work develops a two-stage physics-informed learning framework for PDE inverse problems with jump-discontinuous coefficients. In the first stage, a gradient-adaptive weighted sub-main PINNs (GWS-PINNs) architecture, is employed as a neural-network sampler. The main-network approximates the PDE solution, while the auxiliary coefficient sub-network learns a smoothed continuous surrogate of the underlying piecewise-constant coefficient field over the spatiotemporal interior. To improve sampling stability near possible discontinuity interfaces, a gradient-adaptive weighting strategy is incorporated into the physics residual, which suppresses the influence of high-gradient transition regions and enhances the reliability of coefficient samples in approximately constant regimes. The sampled coefficient values are then processed by a statistical mixture learner. Specifically, a Bayesian Gaussian mixture model (GMM) is used to extract discrete coefficient levels, while a birth-death Markov chain (BDMC) is adopted as a model-selection mechanism to infer the number of coefficient states. For multi-dimensional spatial or spatiotemporal coefficients, a dimension-by-dimension or flattened sampling procedure maps the coefficient samples to one-dimensional sequences for statistical inference and then maps the inferred transition information back to the original domain. This statistical step provides admissible intervals for the coefficient values and localized candidate regions containing possible temporal change points or spatial discontinuity interfaces.

In the second stage, the inverse problem is reformulated as a constrained change-point detection PINNs (CCD-PINNs) estimator. Instead of continuing to represent the coefficient by a smooth neural function, the coefficient field is replaced by an explicit finite-dimensional piecewise-constant parameterization. The discrete coefficient values are optimized within the admissible intervals supplied by the mixture learner, and the corresponding change points or discontinuity boundaries are refined inside the candidate change regions. The solution network is initialized by transfer learning from the first-stage main-network, and residual collocation points are enriched near the candidate transition regions to improve sensitivity to discontinuities. A classification-based refinement mechanism is further used to sharpen the region-to-state assignment and to construct a hard piecewise-constant estimator of the coefficient field. If no parameter variation is detected, the proposed estimator naturally reduces to a standard PINN-based inverse formulation with interval-constrained constant parameters. Otherwise, it identifies both the plateau values and the associated temporal or spatial transition structures. In this way, this framework transforms a preliminary smooth coefficient surrogate into an explicit, constrained, and interpretable piecewise-constant reconstruction while simultaneously producing a high-fidelity surrogate solution.

The main contributions of this work are summarized as follows.

- For existing self-adaptive PINNs, an auxiliary coefficient sub-network is introduced for parameter inference, enabling physics-informed approximation of the coefficient variation process rather than only estimating constant trainable parameters.
- For existing variable-coefficient PINNs, a gradient-adaptive residual weighting strategy is incorporated into the sub-main-network architecture, improving the stability and accuracy of identifying jump-discontinuous coefficients and their transition regions.
- For existing change-point PINNs, a two-stage training framework connected by Bayesian statistical learning is developed. The GMM-BDMC module provides constrained prior information on candidate coefficient estimation intervals and jump-varying regions, enabling accurate temporal change-point identification and extension to multi-dimensional spatial discontinuities.
- For existing statistical mixture and switching models, regime-classification ideas from classical time-series analysis are extended to PDE-governed spatiotemporal systems by applying statistical mixture modeling to physics-informed coefficient samples, thereby broadening their applicability to complex spatiotemporal heterogeneous physical fields.

Overall, JVC-PINNs framework integrates adaptive PINNs, coefficient sub-network sampling, Bayesian mixture modeling, birth-death model selection, and constrained refinement to address inverse problems for PDEs with jump-discontinuous coefficients, where spatiotemporal heterogeneity, unknown regime numbers, uncertain transition locations, and non-smoothness solution challenges coexist.

The remainder of this paper is organized as follows. Section 2 presents the mathematical formulation of spatiotemporal systems with discontinuously varying coefficients and introduces the proposed two-stage framework, including the neural-network based sampler, the statistical model learner, and the constrained parameter refinement estimator. Section 3 reports numerical experiments on representative PDEs with jump discontinuities in their coefficients. Section 4 conducts an ablation study to evaluate the contributions of different loss components. Section 5 compares the proposed method with existing methods in terms of accuracy and computational efficiency. Section 6 presents the applications of this framework of high-resolution physical field reconstruction of PDE solution images. Section 7 investigates the robustness of the framework under different levels of observational noise and the introduction of the uncertainty quantification module. Section 8 summarizes some limitations about this framework. Finally, Section 9 concludes the paper and discusses future directions.

2. Methodology

This section presents a two-stage framework named jump varying coefficients PINNs (JVC-PINNs) for identifying discontinuously varying coefficients in PDEs by two PINNs connected via statistical mixture modeling based on Bayesian learning. After formulating the inverse problem for PDEs with finite piecewise-constant coefficients in the spatiotemporal interior, the first stage employs the GWS-PINNs sampler, in which a main-network approximates the PDE solution while an auxiliary coefficient network, regularized by a gradient-adaptive weighting strategy, produces a smoothed continuous surrogate of the coefficient field and serves as an interior sampler of the underlying piecewise-constant states. These samples are then passed to a statistical mixture method, where GMMs captures the discrete parameter levels and a BDMC adaptively determines the number of states. Meanwhile, a dimension-by-dimension flattening procedure extends this one-dimension analysis to multi-dimensional spatiotemporal coefficients and yields admissible value intervals together with candidate parameter change regions.

In the second stage, the inverse problem is recast as the CCD-PINNs estimator. Instead of continuing to approximate the coefficient field by a smooth neural function, CCD-PINNs performs constrained learning of the physical parameters and their discontinuity locations, the coefficient is reparameterized by a low-dimensional set of piecewise-constant values and change-region variables, all confined to the admissible intervals or regions supplied by the statistical learning results. Moreover, the solution network is fine-tuned through transfer learning, and residual sampling is densified inside the candidate change regions to improve sensitivity to discontinuities. In this way, the proposed framework transforms the preliminary smooth coefficient surrogate into an explicitly constrained piecewise-constant representation, while simultaneously delivering a high-fidelity surrogate solution and an interpretable reconstruction of the discontinuous coefficient field in heterogeneous spatiotemporal PDE systems. An overview of the JVC-PINNs framework is illustrated in Figure 1.

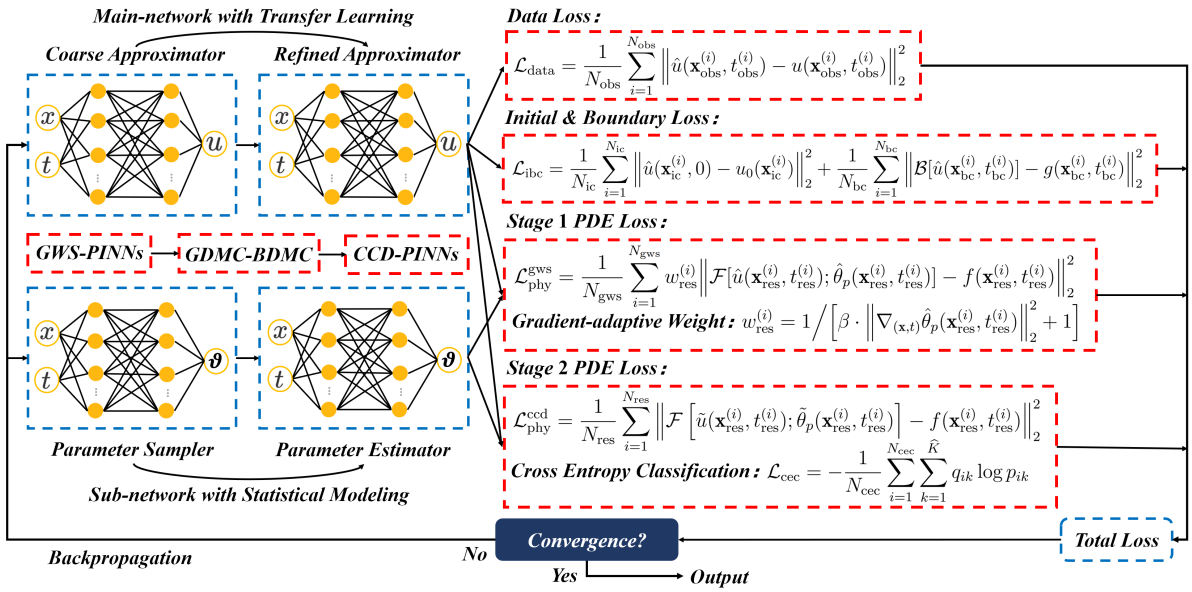


Figure 1: Schematic diagram of JVC-PINNs framework, including GWS-PINNs and CCD-PINNs, which are connected by GMM-BDMC statistical method.

2.1. Mathematical Setup

The PDEs with variable coefficients have been extensively studied in cases involving continuously varying parameters, with numerous numerical and theoretical frameworks proposed for such systems. However, scenarios where coefficients exhibit discontinuous and abrupt changes across spatiotemporal domains, often driven by underlying switching mechanisms in complex systems, remain underexplored and pose unique challenges for inverse problems. This study focuses precisely on PDEs with discontinuously varying coefficients, seeking to accurately identify and infer these parameters from observed system outputs while maintaining computational tractability and interpretability.

To begin with, considering a general initial-boundary value problem with a solution function $u(\mathbf{x}, t)$, where $\mathbf{x} = [x_1, x_2, \ldots, x_d]$ denotes the d-dimensional spatial variable, t denotes time. Let $\Omega \subset \mathbb{R}^d$ be a bounded spatial domain with boundary $\partial\Omega$ and interior Ω°, and let $[t_0, T] \subset \mathbb{R}$ be the temporal interval. The spatiotemporal domain is denoted by

$$\mathcal{Q} = \Omega \times [t_0, T], \quad \mathcal{Q}^\circ = \Omega^\circ \times (t_0, T), \tag{2.1}$$

where $\mathcal{Q}^\circ$ denotes the interior of the spatiotemporal domain. Without loss of generality, set $t_0 = 0$ in the

formulation below. The governing system is formulated as

$$\begin{cases} \mathcal{F}\big[u(\mathbf{x},t);\,\theta_p(\mathbf{x},t)\big] = f(\mathbf{x},t), & (\mathbf{x},t) \in \Omega^\circ \times (0,T], \\ \mathcal{B}[u(\mathbf{x},t)] = g(\mathbf{x},t), & (\mathbf{x},t) \in \partial\Omega \times (0,T], \\ u(\mathbf{x},0) = u_0(\mathbf{x}), & \mathbf{x} \in \Omega, \end{cases} \tag{2.2}$$

where $\mathcal{F}[\cdot]$ denotes a differential operator acting on u and its spatial-temporal derivatives, $\mathcal{B}[\cdot]$ is a boundary operator, e.g., Dirichlet, Neumann, or Robin type, $g(\mathbf{x},t)$ specifies the boundary data, $f(\mathbf{x},t)$ is a source term, $u_0(\mathbf{x})$ provides the initial condition, and $\theta_p(\mathbf{x},t)$ denotes the varying physical parameters of interest to be estimated from observations of physical field $u(\mathbf{x},t)$, which can be a single parameter or m parameters.

For the scenario when PDE coefficients vary over the spatiotemporal domain $\mathcal{Q}$, the parameter $\theta_p(\mathbf{x},t)$ may exhibit certain or random variations over space and time. This work specifically focuses on the case of finite piecewise constant coefficients, a common scenario in which PDE parameters exhibit jump discontinuities through state transitions in complex spatiotemporal systems. Given a finite partition $\{\mathcal{Q}_r\}_{r=1}^R$ of $\mathcal{Q}^\circ$ with $\bigcup_{r=1}^R \mathcal{Q}_r = \mathcal{Q}^\circ$ and $\mathcal{Q}_r \cap \mathcal{Q}_{r'} = \emptyset$ for $r \neq r'$, the coefficient field is assumed to take finitely many constant states. Let $\{\theta_k\}_{k=1}^K$ denote the distinct coefficient states and let $z : \{1,\dots,R\} \to \{1,\dots,K\}$ be the region-to-state map, where R is the number of segments, and K is the number of different parameter states. Then

$$\theta_p(\mathbf{x},t) = \sum_{r=1}^{R} \theta_{z(r)} \mathbf{1}_{\mathcal{Q}_r}(\mathbf{x},t), \tag{2.3}$$

where $K \leq R$ in general, since the same coefficient state may appear in multiple disconnected subdomains.

Further assume that the discontinuity interfaces of $\theta_p(\mathbf{x},t)$ lie strictly within the interior $\mathcal{Q}^\circ$, that is, the set of jump discontinuities in coefficients satisfies

$$\mathcal{J}_\theta := \bigcup_{\substack{r \neq r' \\ z(r) \neq z(r')}} \left(\overline{\mathcal{Q}_r} \cap \overline{\mathcal{Q}_{r'}}\right) \subset \mathcal{Q}^\circ. \tag{2.4}$$

So that parameter variations do not occur at the initial time $t_0 = 0$ or on the spatial boundary $\partial\Omega \times (0,T]$. This regularity assumption is consistent with most physical scenarios in which switching behaviors are intrinsic to the interior dynamics rather than to the imposed boundary and initial data.

With the above setup, the inverse problem addressed in this paper is stated as follows. Given the known differential operator $\mathcal{F}$, the boundary operator $\mathcal{B}$, the source f, the initial condition u_0, together with a set of discrete observations with possibly noisy $\{u(\mathbf{x}_{\text{obs}}^{(i)}, t_{\text{obs}}^{(i)})\}_{i=1}^{N_{\text{obs}}}$, the boundary data $\{g(\mathbf{x}_{\text{bc}}^{(i)}, t_{\text{bc}}^{(i)})\}_{i=1}^{N_{\text{bc}}}$ and the initial data $\{u_0(\mathbf{x}_{\text{ic}}^{(i)})\}_{i=1}^{N_{\text{ic}}}$ collected from the solution of (2.2), our goal is to

identify the discontinuously varying coefficient field $\theta_p(\mathbf{x}, t)$ of the piecewise-constant form (2.3), including the distinct coefficient states $\{\theta_k\}_{k=1}^{K}$, the partition $\{\mathcal{Q}_r\}_{r=1}^{R}$, and the region-to-state map $z(r)$. Equivalently, the task is to recover both the coefficient levels and the interior jump interfaces $\mathcal{J}_\theta$. In the purely one-dimensional temporal case, these interfaces reduce to a finite set of change points $\{\tau_l\}_{l=1}^{L}$, where L is number of candidate change regions, typically $L = R - 1$ for an ordered temporal partition. This part provides the model foundation for the inversion and identification tasks discussed in subsequent sections.

2.2. Neural-Network Based Sampler

In previous works, neural networks have been demonstrated to be a powerful universal function approximator. To address PDEs with spatiotemporal switching coefficients, one necessary modification is extending the PINNs architecture by incorporating an additional sub-network to use a secondary network to learn varying unknown parameters. This subsection introduces the first stage of our two-stage framework, in which a physics-informed deep learning model is used to construct a coefficient sampler over the spatiotemporal domain $\mathcal{Q}$, which refer to as the GWS-PINNs.

In general parameter inversion problems, given a set of observations $\{u(\mathbf{x}_{\text{obs}}^{(i)}, t_{\text{obs}}^{(i)})\}_{i=1}^{N_{\text{obs}}}$ at the training point set $\{(\mathbf{x}_{\text{obs}}^{(i)}, t_{\text{obs}}^{(i)})\}_{i=1}^{N_{\text{obs}}}$ from PDE solutions, together with the boundary data $\{g(\mathbf{x}_{\text{bc}}^{(i)}, t_{\text{bc}}^{(i)})\}_{i=1}^{N_{\text{bc}}}$ on $\partial\Omega \times (0, T]$ and the initial data $\{u_0(\mathbf{x}_{\text{ic}}^{(i)})\}_{i=1}^{N_{\text{ic}}}$ on $\Omega \times \{0\}$, and aim to infer the unknown coefficient field $\theta_p(\mathbf{x}, t)$ in the PDE system (2.2). In the standard PINNs framework [25], the solution $u(\mathbf{x}, t)$ is approximated by a neural network $\hat{u}(\mathbf{x}, t)$, and the parameters to be inferred are treated as learnable variables $\hat{\theta}_p$ optimized via stochastic gradient descent. The total loss is decomposed into a data fitting term, a PDE physics residual term, a boundary condition term, and an initial condition term, given by

$$
\begin{aligned}
\mathcal{L}_{\text{data}} &= \frac{1}{N_{\text{obs}}} \sum_{i=1}^{N_{\text{obs}}} \left\| \hat{u}(\mathbf{x}_{\text{obs}}^{(i)}, t_{\text{obs}}^{(i)}) - u(\mathbf{x}_{\text{obs}}^{(i)}, t_{\text{obs}}^{(i)}) \right\|_2^2, \\
\mathcal{L}_{\text{phy}}^{\text{std}} &= \frac{1}{N_{\text{res}}} \sum_{i=1}^{N_{\text{res}}} \left\| \mathcal{F}[\hat{u}(\mathbf{x}_{\text{res}}^{(i)}, t_{\text{res}}^{(i)}); \hat{\theta}_p] - f(\mathbf{x}_{\text{res}}^{(i)}, t_{\text{res}}^{(i)}) \right\|_2^2, \\
\mathcal{L}_{\text{bc}} &= \frac{1}{N_{\text{bc}}} \sum_{i=1}^{N_{\text{bc}}} \left\| \mathcal{B}[\hat{u}(\mathbf{x}_{\text{bc}}^{(i)}, t_{\text{bc}}^{(i)})] - g(\mathbf{x}_{\text{bc}}^{(i)}, t_{\text{bc}}^{(i)}) \right\|_2^2, \\
\mathcal{L}_{\text{ic}} &= \frac{1}{N_{\text{ic}}} \sum_{i=1}^{N_{\text{ic}}} \left\| \hat{u}(\mathbf{x}_{\text{ic}}^{(i)}, 0) - u_0(\mathbf{x}_{\text{ic}}^{(i)}) \right\|_2^2, \\
\mathcal{L}_{\text{total}} &= \gamma_0 \mathcal{L}_{\text{data}} + \gamma_1 \mathcal{L}_{\text{phy}}^{\text{std}} + \gamma_2 \mathcal{L}_{\text{bc}} + \gamma_3 \mathcal{L}_{\text{ic}},
\end{aligned}
\tag{2.5}
$$

where N_{obs}, N_{res}, N_{bc}, and N_{ic} denote the numbers of observation points, residual points, boundary points, and initial points, respectively. The nonnegative weights γ_1, γ_2 and γ_3 regulate the relative influence of the physics residual and the initial-boundary terms in the total loss, and their values need to be set appropriately based on factors such as the problem scale, the magnitude of observation noise,

and other considerations.

Since $\hat{\theta}_p$ is merely a learnable parameter updated directly through gradient descent, its convergence depends on the choice of initial values. If the initial values are inappropriate, it can lead to prolonged training times or even convergence to incorrect values. Additionally, standard PINNs can only handle parameter inversion for PDEs with constant coefficients and are not suitable for PDEs with discontinuously varying coefficients of the form (2.3). To address the parameter inversion problem for PDEs with spatiotemporal jump-varying coefficients, modifications to the standard PINNs network architecture are required.

Given that neural networks can approximate arbitrary continuous functions, recent research has explored incorporating an additional sub-network into PINNs to fit the unknown varying coefficients in PDEs [35]. To deal with the inversion and identification task of spatiotemporal varying coefficients, constructing a network architecture consisting of a main-network $\hat{u}(\mathbf{x}, t)$ that approximates the PDE solution $u(\mathbf{x}, t)$, and a sub-network $\hat{\theta}_p(\mathbf{x}, t)$ that samples the varying coefficient $\theta_p(\mathbf{x}, t)$ over the spatiotemporal domain. Since the parameter jumps are assumed to occur strictly in the interior $\mathcal{Q}^\circ$, all residual points used for the sub-network are drawn from $\mathcal{Q}^\circ$, i.e., the boundary $\partial\Omega \times (0, T]$ and the initial slice $\Omega \times \{0\}$ are excluded from parameter sampling. Replacing the scalar parameter $\hat{\theta}_p$ by the sub-network output $\hat{\theta}_p(\mathbf{x}, t)$, the data term $\mathcal{L}_{\text{data}}$, the boundary term $\mathcal{L}_{\text{bc}}$, and the initial term $\mathcal{L}_{\text{ic}}$ remain unchanged, while the PDE physics residual term is redefined as

$$\mathcal{L}_{\text{phy}}^{\text{vc}} = \frac{1}{N_{\text{res}}} \sum_{i=1}^{N_{\text{res}}} \left\| \mathcal{F}[\hat{u}(\mathbf{x}_{\text{res}}^{(i)}, t_{\text{res}}^{(i)});\ \hat{\theta}_p(\mathbf{x}_{\text{res}}^{(i)}, t_{\text{res}}^{(i)})] - f(\mathbf{x}_{\text{res}}^{(i)}, t_{\text{res}}^{(i)}) \right\|_2^2, \quad (\mathbf{x}_{\text{res}}^{(i)}, t_{\text{res}}^{(i)}) \in \mathcal{Q}^\circ. \tag{2.6}$$

On the other hand, it is necessary to further optimize the physics residual loss of standard PINNs. For parameter fields with strong discontinuities or jump regions, relying solely on sub-networks is insufficient to effectively suppress abnormal oscillation phenomena in parameter sampling results near discontinuities. To address this issue, exploring weighting strategies during PINNs training has become a mainstream approach. The study [38] proposed introducing adaptive weights into the PDE residual term, which to some extent mitigates underfitting or overfitting of the solution in discontinuous or non-smooth regions during training. Even within a neural network framework that already incorporates a sub-network, it is still possible to apply weighting to the PDE residual term. Specifically, weights that vary with gradients can be introduced into the physics residual, so that $\mathcal{L}_{\text{phy}}$ is further refined into a gradient-adaptive form as

$$\mathcal{L}_{\text{phy}}^{\text{gws}} = \frac{1}{N_{\text{res}}} \sum_{i=1}^{N_{\text{res}}} w_{\text{res}}^{(i)} \left\| \mathcal{F}[\hat{u}(\mathbf{x}_{\text{res}}^{(i)}, t_{\text{res}}^{(i)});\ \hat{\theta}_p(\mathbf{x}_{\text{res}}^{(i)}, t_{\text{res}}^{(i)})] - f(\mathbf{x}_{\text{res}}^{(i)}, t_{\text{res}}^{(i)}) \right\|_2^2, \quad (\mathbf{x}_{\text{res}}^{(i)}, t_{\text{res}}^{(i)}) \in \mathcal{Q}^\circ. \tag{2.7}$$

with

$$w_{\text{res}}^{(i)} = 1 \Big/ \left[\beta \cdot \left\| \nabla_{(\mathbf{x},t)} \hat{\theta}_p(\mathbf{x}_{\text{res}}^{(i)}, t_{\text{res}}^{(i)}) \right\|_2^2 + 1 \right], \tag{2.8}$$

where $w_{\text{res}}^{(i)} > 0$ is the gradient-adaptive weight controlling the contribution of each residual point, $\nabla_{(\mathbf{x},t)}$ denotes the spatiotemporal gradient operator acting on the sub-network output, and β is the gradient-adaptive weight hyperparameter. This mechanism down-weights residual points in regions where the sampled coefficient field exhibits large gradients near discontinuity interfaces $\mathcal{J}_\theta$, while increasing weights in smoother regions to improve accuracy. This strategy facilitates more precise estimation of $\hat{\theta}_p(\mathbf{x}, t)$, supporting accurate parameter sampling results based on the learned spatiotemporal coefficient field.

Combining the unchanged data, boundary, and initial losses with the redefined gradient-adaptive physics residual, the total loss of the GWS-PINNs sampler is given by

$$\mathcal{L}_{\text{sam}} = \gamma_0 \mathcal{L}_{\text{data}} + \gamma_1 \mathcal{L}_{\text{phy}}^{\text{gws}} + \gamma_2 \mathcal{L}_{\text{bc}} + \gamma_3 \mathcal{L}_{\text{ic}}. \tag{2.9}$$

In contrast to time-domain partitioning approaches such as DSBL [39] and BC-PINNs [34], the sub-network structure can approximate a wide range of coefficient types, including piecewise constants, stochastic time-varying parameters, spatially heterogeneous fields, and more complex distributions. In addition, GWS-PINNs flexibly directs learning within the PDE domain using adaptive weighting to suppress instability in regions of high gradient of discontinuous parameter variation, which helps to avoid numerical oscillations and overfitting phenomena in the vicinity of these regions, and thus improves the physical consistency between the neural networks and real systems.

Given observed data from PDE solutions, the main-network and sub-network respectively output $\hat{u}(\mathbf{x}, t)$ and $\hat{\theta}_p(\mathbf{x}, t)$. Physics residuals are constructed using automatic differentiation and refined by adaptive weights to form the final loss for backpropagation. Once trained, $\hat{u}(\mathbf{x}, t)$ provides a continuous approximation of the PDE solution, while $\hat{\theta}_p(\mathbf{x}, t)$ yields a continuous surrogate of the underlying piecewise-constant coefficient field. Although the sub-network output remains continuous and thus can only approximate the true jump-varying parameter (2.3) in a smoothed manner, the gradient-adaptive weighting confines the transition regions to be sufficiently narrow, so that $\hat{\theta}_p(\mathbf{x}, t)$ evaluated at a finite collection of interior points in $\mathcal{Q}^\circ$ constitutes a reliable empirical sample of the discontinuous coefficient field. These samples will then be passed to the statistical learner introduced in the next subsection, in which a GMM combined with a birth-death Markov chain is employed to extract the discrete parameter states and to locate the corresponding jump regions.

2.3. Statistical Mixture Modeling

After the first-stage training of GWS-PINNs, evaluating the sub-network $\hat{\theta}_p(\mathbf{x}, t)$ at a finite set of interior collocation points in $\mathcal{Q}^\circ$ yields a collection of samples of the underlying piecewise-constant coefficient field. By flattening these samples into a one-dimensional sequence, then obtain a sequence

$$\mathbf{y} = \{y_n\}_{n=1}^{N}, \tag{2.10}$$

where each y_n is the sub-network output at the n-th interior point under the prescribed flattening rule. For a one-dimensional temporal coefficient $\theta(t)$, the natural time ordering is used directly. For a $d+1$-dimensional spatiotemporal coefficient $\theta_p(\mathbf{x}, t)$, the flattening can be performed in different admissible ways, such as traversing the interior points along coordinate axes or randomly mixing all interior samples, as long as the multi-dimensional interior data in $\mathcal{Q}^\circ$ are transformed into a one-dimensional sequence. Since the GMM-BDMC learner depends only on the empirical distribution of the sampled coefficient values, different bijective flattening strategies lead to identical statistical targets up to permutation of sample indices. Consequently, flattening serves only as a computational representation and does not affect the subsequent recovery of discontinuity regions in the original spatiotemporal domain. After statistical inference, the identified indices can be mapped back to the original spatiotemporal domain through the inverse of the flattening operation. In this way, the inference of discontinuously varying coefficients across space and time is reduced to a unified one-dimensional statistical learning task.

Since the sub-network sampling inevitably carries bias from observation noise and network approximation error, a Gaussian assumption is adopted around each latent constant state. Combined with the finite piecewise-constant structure (2.3), the marginal distribution of y_n is modeled as a GMM

$$\Pr(y_n|\boldsymbol{\vartheta}) = \sum_{k=1}^{K} \eta_k \, f_{\mathcal{N}}(y_n;\, \mu_k, \sigma_k^2), \quad \sum_{k=1}^{K} \eta_k = 1, \tag{2.11}$$

with parameters $\boldsymbol{\vartheta} = \{\mu_k,\, \sigma_k,\, \eta_k\}_{k=1}^{K}$ and latent allocations $\mathbf{S} = \{S_n\}_{n=1}^{N}$, $S_n \in \{1, \ldots, K\}$. Here $f_{\mathcal{N}}$ denotes the univariate Gaussian density. The parameters are inferred via a Bayesian Markov chain Monte Carlo (MCMC) sampler with conditionally conjugate priors, summarized as

$$\sigma_k^2 \sim \mathcal{IG}(c_0, C_0), \quad \mu_k \mid \sigma_k^2 \sim \mathcal{N}(b_0, \sigma_k^2), \quad \boldsymbol{\eta} \sim \mathcal{D}(1, \ldots, 1), \tag{2.12}$$

where $\mathcal{N}$, $\mathcal{IG}$ and $\mathcal{D}$ denote the Gaussian, inverted-Gamma and Dirichlet distributions, respectively. Conjugacy yields closed-form Gibbs sampler updates

$$\sigma_k^2 \,|\, \mathbf{y}, \mathbf{S} \sim \mathcal{IG}(c_k(\mathbf{S}), C_k(\mathbf{S})), \quad \mu_k \,|\, \sigma_k^2, \mathbf{y}, \mathbf{S} \sim \mathcal{N}(b_k(\mathbf{S}), B_k(\mathbf{S})), \quad \boldsymbol{\eta} \,|\, \mathbf{S} \sim \mathcal{D}(e_1(\mathbf{S}), \ldots, e_K(\mathbf{S})), \tag{2.13}$$

where

$$\begin{aligned} &c_k(\mathbf{S}) = c_0 + \frac{1}{2} N_k(\mathbf{S}), \quad C_k(\mathbf{S}) = C_0 + \frac{1}{2}\left(N_k(\mathbf{S})\, s_{y,k}^2(\mathbf{S}) + \frac{N_k(\mathbf{S})}{N_k(\mathbf{S})+1} (\bar{y}_k(\mathbf{S}) - \bar{y})^2 \right), \\ &b_k(\mathbf{S}) = \frac{b_0 + N_k(\mathbf{S})\bar{y}_k(\mathbf{S})}{N_k(\mathbf{S})+1}, \quad B_k(\mathbf{S}) = \frac{\sigma_k^2}{N_k(\mathbf{S})+1}, \quad e_k(\mathbf{S}) = N_k(\mathbf{S}) + 1, \end{aligned} \tag{2.14}$$

with $N_k(\mathbf{S})$, $\bar{y}_k(\mathbf{S})$, and $s_{y,k}^2(\mathbf{S})$ denoting the count, mean, and variance of the samples allocated to component k.

A key difficulty is that the number of components K is unknown a priori of GMM. Information-criterion-based approaches require fitting all candidate models for comparison, which is computationally expensive. Instead, using a birth-death Markov chain (BDMC) mechanism that treats K itself as a random variable evolving in continuous time. For K-component GMM $\mathcal{M}_K$, a birth occurs at a constant rate $b(s) \equiv \lambda_b$, which appends a new component with weight $\eta_{K+1} \sim \mathcal{B}e(1, K)$ sampled from a Beta distribution and rescaling $\eta_j^{\text{new}} = \eta_j(1 - \eta_{K+1})$ for $j \leq K$, while each existing component k dies at rate

$$d_k = \frac{\lambda_b \cdot \Pr(\mathbf{y} \mid \mathcal{M}_{K-1}, \boldsymbol{\vartheta}^{-k}) \Pr(\mathcal{M}_{K-1})}{K \cdot \Pr(\mathbf{y} \mid \mathcal{M}_K, \boldsymbol{\vartheta}^K) \Pr(\mathcal{M}_K)}, \quad k = 1, \ldots, K, \tag{2.15}$$

where $\boldsymbol{\vartheta}_{-k}$ means remove the parameters related to the k-th component from the old GMM parameter set as

$$\boldsymbol{\vartheta}^{-k} = \{\mu_1, \cdots, \mu_{k-1}, \mu_{k+1}, \cdots, \mu_K, \sigma_1, \cdots, \sigma_{k-1}, \sigma_{k+1}, \cdots, \sigma_K, \eta_1, \cdots, \eta_{k-1}, \eta_{k+1}, \cdots, \eta_K\}, \tag{2.16}$$

with total death rate $d(s) = \sum_{k=1}^{K} d_k$ and inter-event time $\Delta s \sim \mathcal{E}(b(s) + d(s))$ from a exponential distribution. A birth is chosen with probability $b(s)/(b(s) + d(s))$ and the death of component k with probability $d_k/(b(s) + d(s))$. Between jump events, Gibbs sampling is performed at the current K to update $(\boldsymbol{\vartheta}, \mathbf{S})$. Letting T_K denote the total time that the chain spends in state $\mathcal{M}_K$ over the evolution horizon $[0, s_{\max}]$, the optimal component number is estimated as

$$\widehat{K} = \arg\max_K \frac{T_K}{s_{\max}}. \tag{2.17}$$

With $\widehat{K}$ fixed, discarding the first M_0 burn-in samples and averaging the remaining M posterior draws yields the component-wise estimates

$$\widehat{\mu}_k = \frac{1}{M} \sum_{j=1}^{M} \mu_{k,j}, \quad \widehat{\sigma}_k = \frac{1}{M} \sum_{j=1}^{M} \sigma_{k,j}, \quad k = 1, \ldots, \widehat{K}. \tag{2.18}$$

To avoid label switching, the mixture components are relabeled after each posterior draw such that $\mu_1 < \mu_2 < \cdots < \mu_{\widehat{K}}$. Through this way, the framework understood how parameters undergo discontinuous jumps in the spatiotemporal domain, simply from the discrete observations of the PDE solution training in the first-stage PINNs. For more details on mixed statistical model learning with GMM-BDMC, refer to [40].

Based on statistical mixture modeling results, the posterior moments directly provide informative search intervals that will be used to constrain the next second-stage PINNs inverse problem. For each identified state k, the candidate interval for the jump-parameter value is defined as

$$\mathcal{I}_k = \left[\, \widehat{\mu}_k - \widehat{\sigma}_k,\ \widehat{\mu}_k + \widehat{\sigma}_k \,\right], \quad k = 1, \ldots, \widehat{K}, \tag{2.19}$$

which reflects the posterior uncertainty around each discrete parameter level. Correspondingly, the one dimensional set of coefficient samples indices whose samples fall outside every $\mathcal{I}_k$ are regarded as lying in transition regions between adjacent states. Mapping these indices back to the original spatiotemporal domain through the inverse of the flattening operation yields the candidate change-point set

$$\mathcal{X} = \Big\{(\mathbf{x}, t) \in \mathcal{Q}^\circ : \hat{\theta}_p(\mathbf{x}, t) \notin \bigcup_{k=1}^{\widehat{K}} \mathcal{I}_k \Big\}. \tag{2.20}$$

The candidate change-point set is further divided according to geometric connectivity in the original spatiotemporal domain. Specifically, connected points are grouped into the same candidate change region, while disconnected parts are treated as different regions with the number of candidate change regions $\widehat{L}$ as

$$\mathcal{X} = \bigcup_{l=1}^{\widehat{L}} \mathcal{X}_l, \quad \mathcal{X}_l \cap \mathcal{X}_{l'} = \varnothing, \quad l \neq l', \tag{2.21}$$

where each $\mathcal{X}_l$ is a geometrically connected component. For purely temporal coefficients, (2.21) reduces to a finite union of candidate change-point time intervals. The pair $\big(\{\mathcal{I}_k\}_{k=1}^{\widehat{K}}, \{\mathcal{X}_l\}_{l=1}^{\widehat{L}}\big)$ provides both admissible parameter ranges and localized jump regions, which will serve in the next subsection as interval constraints on the learnable parameter vector and as a refinement indicator for residual point sampling in the second-stage PINNs inverse estimator.

The above analysis is formulated for a single jump-varying physical parameter in the spatiotemporal domain. When the governing equation contains multiple discontinuously varying number m coefficients, the GWS-PINNs sampling and GMM-BDMC inference procedures are applied to each parameter separately, producing parameter-specific admissible value intervals and candidate change regions. These statistical results are then passed individually to the subsequent CCD-PINNs refinement stage, where each coefficient is constrained and refined according to its own candidate intervals and change regions. In this way, the final jump-varying parameters are learned separately while preserving the distinct discontinuity structures of different physical coefficients.

2.4. Constrained Parameter Refinement

Based on the statistical mixture learner, the number of discrete parameter states $\widehat{K}$, the candidate parameter intervals $\{\mathcal{I}_k\}_{k=1}^{\widehat{K}}$, and the candidate jump regions $\{\mathcal{X}_l\}_{l=1}^{\widehat{L}}$ have been obtained. The fourth step of the proposed framework is a constrained parameter refinement, denoted by CCD-PINNs. Its role is not to relearn a smooth coefficient field, but to refine the piecewise-constant coefficient field (2.3) under the constraints inferred from the statistical learning step. In contrast to time-domain partitioning approaches such as CP-PINNs [36], the framework can more effectively solve inverse problems involving PDEs with spatiotemporal jump coefficients guided by prior information from statistical learning.

In the refinement stage, the main-network $\tilde{u}(\mathbf{x}, t)$ for the PDE solution is initialized by the trained main-network of the GWS-PINNs approximator in the previous stage. The coefficient values are treated as trainable variables and are constrained by

$$\theta_k \in \mathcal{I}_k, \quad k = 1, \ldots, \widehat{K}. \tag{2.22}$$

These constraints can be enforced by projection after each optimization step or by bounded reparameterization.

The refinement of jump locations is performed inside the candidate regions $\{\mathcal{X}_l\}_{l=1}^{\widehat{L}}$. Instead of assigning an independent binary classifier to each candidate region, introducing a multi-class classifier as

$$g(\mathbf{x}, t) = \left(g^{(1)}(\mathbf{x}, t), \ldots, g^{(\widehat{K})}(\mathbf{x}, t)\right) \in \mathbb{R}^{\widehat{K}}, \tag{2.23}$$

where $g^{(k)}(\mathbf{x}, t)$ denotes the logit associated with the k-th coefficient state, $\widehat{K}$ is the number of coefficient states identified by the GMM-BDMC step. For a refinement point $(\mathbf{x}_i, t_i)$, the probability that it belongs to the k-th coefficient state is defined by the softmax function

$$p_{ik} = \exp\left(g^{(k)}(\mathbf{x}_i, t_i)\right) \Big/ \sum_{j=1}^{\widehat{K}} \exp\left(g^{(j)}(\mathbf{x}_i, t_i)\right), \quad k = 1, \ldots, \widehat{K}. \tag{2.24}$$

The hidden label of $(\mathbf{x}_i, t_i)$ is assigned according to the nearest GMM state mean obtained from the statistical mixture learner

$$s_i = \arg \min_{1 \le k \le \widehat{K}} \left|\hat{\theta}_p(\mathbf{x}_i, t_i) - \widehat{\mu}_k\right|. \tag{2.25}$$

Equivalently, its one-hot representation is denoted by

$$q_{ik} = \begin{cases} 1, & k = s_i, \\ 0, & k \neq s_i. \end{cases} \tag{2.26}$$

The corresponding cross entropy classification loss is defined as

$$\mathcal{L}_{\text{cec}} = -\frac{1}{N_{\text{cec}}} \sum_{i=1}^{N_{\text{cec}}} \sum_{k=1}^{\widehat{K}} q_{ik} \log p_{ik}, \tag{2.27}$$

where N_{cls} is the number of refinement points used to train the classifier. This loss encourages each refinement point to be assigned to one of the $\widehat{K}$ coefficient states, thereby sharpening the transition regions obtained from the first-stage smooth sampler and refining the estimated region-to-state map $\hat{z}(r)$.

For one-dimensional temporal switching, the classification boundary degenerates into a set of change points. Therefore, training the classifier inside $\{\mathcal{X}_l^\tau\}_{l=1}^{\widehat{L}}$ gives the refined temporal jump locations

$$\{\widehat{\tau}_l\}_{l=1}^{\widehat{L}}, \quad \widehat{\tau}_l \in \mathcal{X}_l^\tau. \tag{2.28}$$

For multi-dimensional spatial or spatiotemporal discontinuities, the same classification procedure gives the estimated discontinuity boundary related to (2.4) as

$$\widehat{\mathcal{J}}_\theta = \bigcup_{l=1}^{\widehat{L}} \widehat{\mathcal{J}}_l, \quad \widehat{\mathcal{J}}_l \subset \mathcal{X}_l^\tau. \tag{2.29}$$

Thus, the candidate jump regions supplied by the statistical learner are further refined into either pointwise change locations or multi-dimensional jump interfaces.

With the refined coefficient values and the refined partition, the discontinuous coefficient is represented as a hard piecewise-constant function

$$\theta_p(\mathbf{x}, t) = \sum_{r=1}^{\widehat{R}} \theta_{\widehat{z}(r)} \mathbf{1}_{\widehat{\mathcal{Q}}_r}(\mathbf{x}, t), \quad \widehat{z}(r) \in \{1, \ldots, \widehat{K}\}. \tag{2.30}$$

where the subdomains $\{\widehat{\mathcal{Q}}_k\}_{k=1}^{\widehat{K}}$ are determined by $\{\widehat{\tau}_l\}_{l=1}^{\widehat{L}}$ in the one-dimensional temporal case and by $\widehat{\mathcal{J}}_\theta$ in the multi-dimensional case. Additionally, $\widehat{R}$ is the number of refined piecewise-constant subdomains, and $\widehat{z}(r)$ assigns the r-th estimated subdomain to one of the $\widehat{K}$ coefficient states.

The physics residual in the CCD-PINNs stage is obtained by replacing the smooth coefficient subnetwork with the hard piecewise-constant coefficient:

$$\mathcal{L}_{\text{phy}}^{\text{ccd}} = \frac{1}{N_{\text{ccd}}} \sum_{i=1}^{N_{\text{ccd}}} \left\| \mathcal{F}\left[\tilde{u}(\mathbf{x}_{\text{res}}^{(i)}, t_{\text{res}}^{(i)}); \tilde{\theta}_p(\mathbf{x}_{\text{res}}^{(i)}, t_{\text{res}}^{(i)})\right] - f(\mathbf{x}_{\text{res}}^{(i)}, t_{\text{res}}^{(i)}) \right\|_2^2, \quad (\mathbf{x}_{\text{res}}^{(i)}, t_{\text{res}}^{(i)}) \in \mathcal{Q}^\circ. \tag{2.31}$$

The residual set contains uniformly sampled interior points and additional points sampled from the candidate jump regions, which improves the resolution of the physics loss near discontinuities and to train the local classification loss.

Combining the data, physics, boundary, initial, and classification terms, the total loss of CCD-PINNs is defined as

$$\mathcal{L}_{\text{est}} = \gamma_0 \mathcal{L}_{\text{data}} + \gamma_1 \mathcal{L}_{\text{phy}}^{\text{CCD}} + \gamma_2 \left(\mathcal{L}_{\text{bc}} + \mathcal{L}_{\text{ic}}\right) + \gamma_3 \mathcal{L}_{\text{cec}}, \tag{2.32}$$

where γ_3 is a new nonnegative weight.

The final output of the constrained refinement stage is the hard piecewise-constant estimator from

sub-network related to (2.3) as

$$\tilde{\theta}_p(\mathbf{x},t)=\begin{cases}\hat{\theta}_1, & (\mathbf{x},t)\in\widehat{\mathcal{Q}}_1,\\ \hat{\theta}_2, & (\mathbf{x},t)\in\widehat{\mathcal{Q}}_2,\\ \vdots & \vdots\\ \hat{\theta}_{\widehat{K}}, & (\mathbf{x},t)\in\widehat{\mathcal{Q}}_{\widehat{K}},\end{cases}\tag{2.33}$$

where $\{\widehat{\mathcal{Q}}_k\}_{k=1}^{\widehat{K}}$ is determined by the estimated temporal change points $\{\widehat{\tau}_l\}_{l=1}^{\widehat{L}}$ or by the estimated multi-dimensional discontinuity boundary $\widehat{\mathcal{J}}_\theta$. The refinement solution $\tilde{u}(\mathbf{x},t)$ from main work is also output.

For the case with multiple discontinuously varying parameters, suppose that there are m coefficient fields to be estimated, denoted by $\{\theta_p^{(j)}(\mathbf{x},t)\}_{j=1}^m$. The constrained refinement stage outputs a hard piecewise-constant estimator for each parameter separately, given by

$$\left(\tilde{\theta}_p^{(1)}(\mathbf{x},t),\cdots,\tilde{\theta}_p^{(m)}(\mathbf{x},t)\right)=\left(\sum_{r=1}^{\widehat{R}^{(1)}}\hat{\theta}^{(1)}_{\hat{z}^{(1)}(r)}\mathbf{1}_{\widehat{\mathcal{Q}}_r^{(1)}}(\mathbf{x},t),\ \cdots,\ \sum_{r=1}^{\widehat{R}^{(m)}}\hat{\theta}^{(m)}_{\hat{z}^{(m)}(r)}\mathbf{1}_{\widehat{\mathcal{Q}}_r^{(m)}}(\mathbf{x},t)\right).\tag{2.34}$$

Here, $\widehat{R}^{(j)}$, $\widehat{\mathcal{Q}}_r^{(j)}$, and $\hat{z}^{(j)}(r)$ denote the number of refined subdomains, the r-th estimated subdomain, and the corresponding region-to-state map for the j-th parameter, respectively. Each parameter is refined according to its own admissible value intervals and candidate change regions obtained from the statistical mixture modeling step.

In summary, this framework presents a two-stage methodology for identifying discontinuously varying coefficients in PDEs. The first stage introduces a gradient-adaptive weighted sub-main physics-informed neural network, where a main-network approximates the PDE solution and a sub-network generates a smooth surrogate of the underlying piecewise-constant coefficients. These samples are then processed using a Bayesian GMM with a BDMC to identify discrete parameter levels and localize candidate jump regions. In the second stage, the continuous surrogate is replaced with a finite-dimensional step-function representation. The coefficient values are refined within $\{\mathcal{I}_k\}_{k=1}^{\widehat{K}}$, while the change points or discontinuity boundaries are refined inside $\{\mathcal{J}_l^\tau\}_{l=1}^{\widehat{L}}$ through constrained local multi-class classification. The novelty lies in combining adaptive weighting, sub-network coefficient sampling, Bayesian mixture modeling, and constrained classification-based refinement to achieve accurate reconstruction of discontinuous coefficients while reducing the search space and improving stability near discontinuities.

3. Numerical Examples

To validate the effectiveness of the proposed two-stage JVC-PINNs framework for inverse problems of PDEs with discontinuously varying coefficients, this section presents a series of numerical simulation

experiments on representative spatiotemporal dynamical systems. The proposed method first employs GWS-PINNs to generate a smooth surrogate sampler of the unknown coefficient field, then uses the GMM-BDMC statistical learner to infer the number of discrete coefficient states, admissible parameter intervals, and candidate jump regions, and finally applies CCD-PINNs to refine the piecewise-constant coefficient values and discontinuity locations under these statistical constraints. In this way, the numerical experiments evaluate not only the preliminary coefficient sampling capability of the first-stage network, but also the final constrained parameter estimation accuracy of the second-stage refinement model. The numerical simulation cases selected for this study are all derived from existing research, and reference solutions were generated using a high-precision finite element method.

For PDEs with discontinuously time-varying coefficients, wave equations, heat equations, Burgers' equations, and Navier-Stokes equations are considered. For each equation, multiple jump scenarios are designed to represent abrupt parameter changes, multi-state switching behaviors, and different jump magnitudes that may appear in complex physical systems. The numerical results are used to assess the accuracy, stability, and robustness of the proposed framework in recovering both the discrete coefficient levels and the corresponding temporal change points. In addition, the refined solution network from CCD-PINNs is examined to verify whether the learned discontinuous coefficient structure improves the physical consistency of the reconstructed PDE solution.

To further verify the applicability of the proposed method to discontinuously space-varying coefficients, specially in multi-dimensional scenarios, the wave equation and the Helmholtz equation are employed as representative spatial examples. The coefficients are configured to be piecewise constant over both regular and irregular spatial subdomains. These examples are designed to test whether the proposed pipeline framework can accurately infer discrete spatial coefficient states and refine the corresponding discontinuity interfaces. The experimental results demonstrate that the proposed JVC-PINNs framework exhibits strong adaptability and stability for jump-varying coefficient identification across different PDE types, jump patterns, and spatial structures.

Stage 1 used GWS-PINNs with a main solution network $\hat{u}$ and an auxiliary coefficient sub-network $\hat{\theta}_p$. Stage 2 used CCD-PINNs, transferred the Stage 1 solution network, and replaced the smooth coefficient network by a constrained hard piecewise-constant estimator $\tilde{\theta}_p$. Set the observation, physical residual, initial-condition, boundary-condition, and classification weights by γ_0, γ_1, γ_2, γ_3, and γ_4, respectively. The observation weight was fixed as $\gamma_0 = 1$, while γ_1-γ_3 were set case by case as reported below. Stage 2 generally uses the same weight settings as Stage 1 and the added weight fixed as $\gamma_4 = 50$ in all experiments. The classification term, when used, is a cross-entropy loss, and its classification sub-network uses ReLU activations. All other networks use tanh activations. Unless stated otherwise, gradient-adaptive weight hyperparameter $\beta = 1$ in GWS-PINNs, Adam optimizer was used, stopping was by a fixed iteration or epoch budget with blind-objective checkpoint selection, and random seeds were set for Python by

NumPy, PyTorch and CUDA. The GMM-BDMC learner used $K_{\max} = 5$, initial $K = 3$, birth rate $\lambda_b = 1$, stop time 200, 25 inner Gibbs updates, burn-in $M_0 = 2000$, posterior samples $M = 4000$, $c_0 = 2.5$, $C_0 = 0.5s_y^2$, $b_0 = \bar{y}$, where $\bar{y}$, s_y^2 are the sample mean and variance of samplers $\{y_n\}_{n=1}^N$ from GWS-PINNs. A symmetric Dirichlet $(1, \ldots, 1)$ prior for the mixture weights. The details regarding the training of neural networks will be covered after introduction of each types of PDEs. The numerical cases are conducted using the device with NVIDIA GeForce RTX 5060 Ti GPU with PyTorch 2.11.0.and cu130. The code used in this study is available at `https://github.com/Zhikun0416/Inverse-Problem-for-Partial-Differential-Equations-with-Jump-Discontinuities-in-Coefficients`.

3.1. Wave Equation

First, a 1+1D nonlinear wave equation, which means define in 1-dimensional space and 1-dimensional time, namely the Sine-Gordon equation, with a time-varying physical coefficient $\alpha(t) > 0$ is considered. This example is from [41] and the governing equation is given by

$$\begin{cases} u_{tt} = \alpha(t)u_{xx} + \sin u, & (x,t) \in U \times (0,T], \\ u(x,t) = 0, & (x,t) \in \partial U \times (0,T], \\ u_t(x,0) = 0, & x \in U, \\ u(x,0) = g(x), & x \in U. \end{cases} \tag{3.1}$$

Let $U = [0,1]$, $T = 10$, and the initial function be

$$g(x) = \sin \pi x. \tag{3.2}$$

Two different scenarios of time-varying coefficients are considered.

Case 1.1:

$$\alpha(t) = 1, \quad t \in [0,10]. \tag{3.3}$$

Case 1.2:

$$\alpha(t) = \begin{cases} 0.5, & t \in [0,5), \\ 1, & t \in [5,10]. \end{cases} \tag{3.4}$$

The spatiotemporal solution fields of these two wave equations and the corresponding two-stage parameter inversion results for the coefficient $\alpha(t)$ are shown in Figure 2. In the parameter inversion plots, the Stage 1 result represents the relaxed continuous approximation generated by the GWS-PINNs coefficient sub-network. Since the sub-network is a continuous neural function, the Stage 1 approximation

may smooth the true discontinuity and form a transition layer near the jump location. The Stage 2 result represents the hard piecewise-constant estimator refined by CCD-PINNs under the statistical constraints supplied by GMM-BDMC. The solid black line represents the actual values of the PDE coefficient jumps, while the red markers and blue dashed lines represent the approximated results of the parameters before and after the two GWS-PINNs and CCD-PINNs stages, respectively. The blue shaded coefficient bands denote the admissible parameter intervals inferred from the posterior GMM components, and the red shaded temporal bands denote the candidate change-point intervals used in the constrained refinement stage.

The mean square error (MSE) between the reference solution and the reconstructed solution is defined as

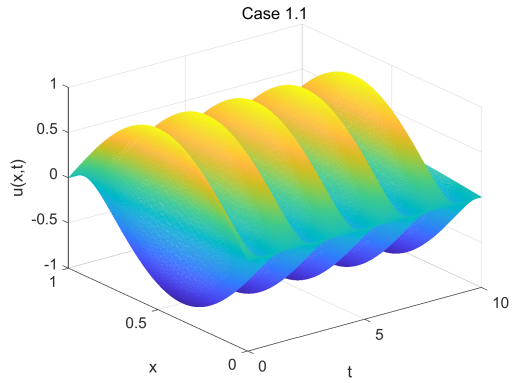
$$MSE_{\hat{u}} = \frac{1}{N_{\text{obs}}} \sum_{i=1}^{N_{\text{obs}}} \left[\hat{u}(\mathbf{x}_{\text{obs}}^{(i)}, t_{\text{obs}}^{(i)}) - u(\mathbf{x}_{\text{obs}}^{(i)}, t_{\text{obs}}^{(i)}) \right]^2, \tag{3.5}$$

where $\hat{u}$ denotes the refined solution network obtained from the first-stage GWS-PINNs, which can be replaced with $\tilde{u}$ from the second-stage CCD-PINNs. The MSE and estimated parameter values are retained to four decimal places, and the relative percentage error is retained to two decimal places. The same precision setting is adopted for the remaining numerical examples.

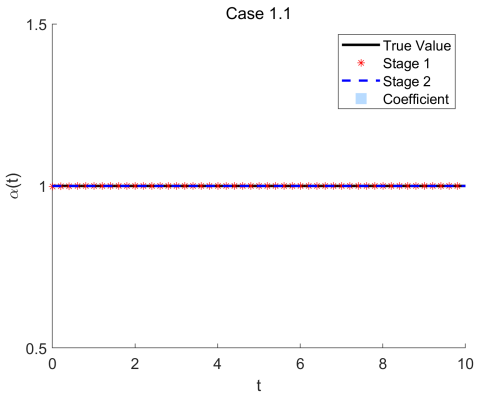
For Case 1.1 and Case 1.2 ran used seed 101, $\theta_p = \alpha(t)$ on $(x,t) \in [0,1] \times [0,10]$. The Stage 1 main-network was a Fourier-feature network with layers $[2, 200, 200, 1]$, and the coefficient network with layers $[1, 50, 50, 50, 50, 1]$. Adam ran for 5.0×10^4 iterations. The learning rate for $\hat{u}$ was 10^{-3}, and the learning rate for $\hat{\theta}_p$ was 5×10^{-4} in Case 1.1 and 10^{-3} in Case 1.2. The training sets used $50 \times 80 = 4000$ residual grid points, 6000 strict interior observation points, 4000 random initial-condition points on $t = 0$, and 4000 random boundary points split across the two spatial boundaries. The remaining loss weights were $\gamma_1 = 1$, $\gamma_2 = 1$, $\gamma_3 = 0.5$. Stage 2 sub-network used a hard-step $\alpha(t)$ initialized from GMM-BDMC intervals and Stage 1 stable-platform means, with same Adam learning rate 10^{-4} in main and sub-networks.

For Case 1.1, the GMM-BDMC statistical learner identifies $\widehat{K} = 1$, indicating that the coefficient contains only one constant state. Therefore, no temporal change point is introduced in the second-stage refinement. In this situation, CCD-PINNs automatically degenerates into a constrained constant-coefficient inverse estimator, and the estimated coefficient remains consistent with the reference value. This result confirms that the proposed framework does not artificially introduce discontinuities when the underlying PDE coefficient is constant.

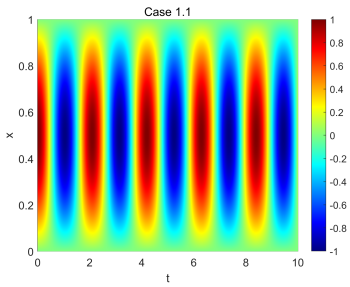
For Case 1.2, the GMM-BDMC learner identifies two coefficient states and provides admissible intervals for the two parameter values, together with a candidate temporal change-point interval. The Stage 1 coefficient approximation in GWS-PINNs is continuous and thus produces a smooth transition near the true jump time. However, this relaxed approximation still contains sufficient statistical information for



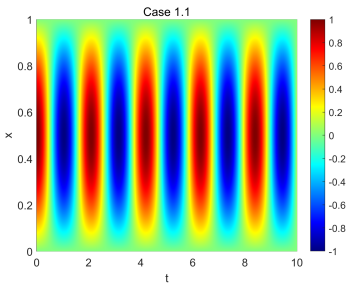
a: Spatiotemporal solution



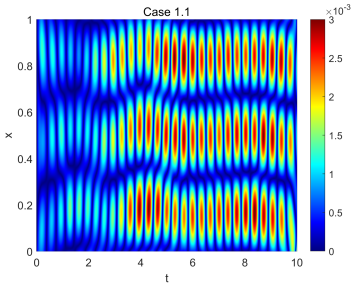
b: Parameter inverse result



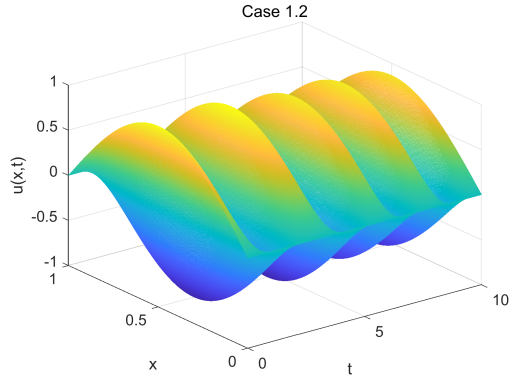
c: Reference solution



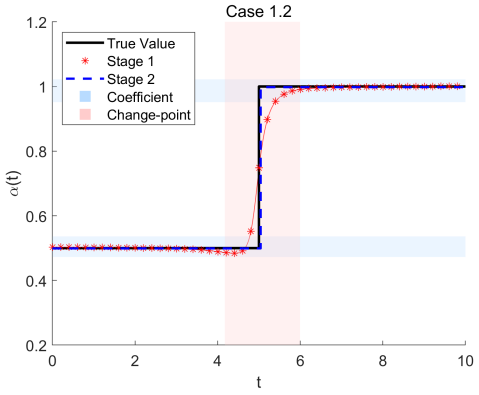
d: Predicted solution



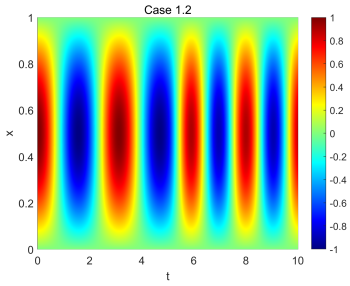
e: Absolute error



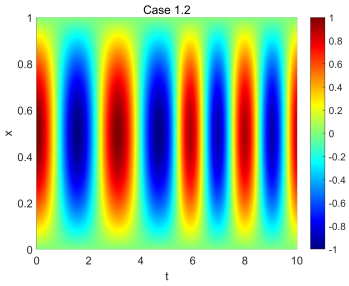
f: Spatiotemporal solution



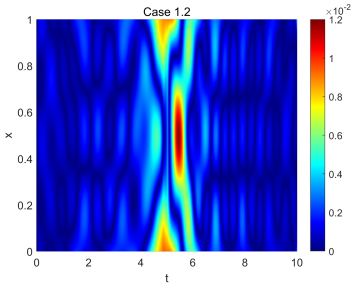
g: Parameter inverse result



h: Reference solution



i: Predicted solution



j: Absolute error

Figure 2: Numerical results for wave equations with discontinuously time varying coefficient $\alpha(t)$.

the GMM-BDMC model to separate the underlying coefficient states. The subsequent CCD-PINNs refinement further converts the continuous surrogate into a sharp step-function representation and yields a refined change point within the candidate interval. Therefore, the Stage 2 estimator provides an explicit and interpretable reconstruction of the discontinuously time-varying coefficient.

The reconstructed solution based on the second-stage main-network $\tilde{u}$ and the comparison of its absolute error with the reference solution are shown in the corresponding rows of Figure 2. The results indicate that the reconstructed solution is close to the reference solution and that the absolute error is well controlled. These observations demonstrate that the hard piecewise-constant coefficient refined by CCD-PINNs can also preserve the physical consistency of the solution approximation. The effectiveness of the proposed algorithm will be further validated in subsequent multi-dimensional spatial examples.

Next, a 2+1D linear wave equation with a 2D space-varying coefficient $\alpha(x, y)$ is considered from research [42]. The governing equation is

$$u_{tt} = \alpha(x, y)\Delta u, \quad (x, y, t) \in U \times (0, T], \tag{3.6}$$

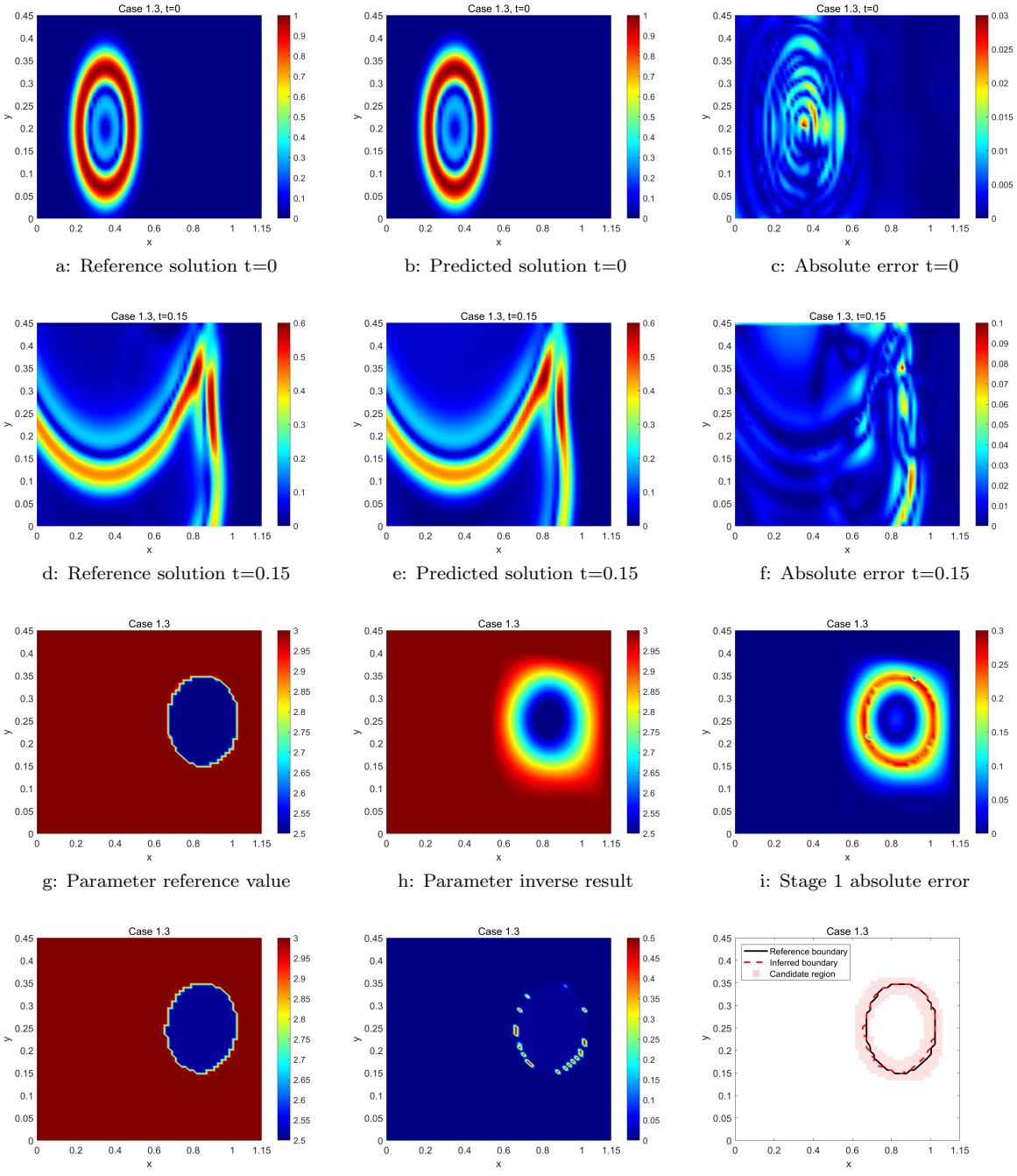
where $U = [0, 1.15] \times [0, 0.45] \subset \mathbb{R}^2$ and $T = 0.2$. The wave formation and propagation process in this spatial domain is illustrated in Figure 3. In this numerical example, an irregular approximately circular open region $U_2 \subset U$ is located on the right side of the spatial domain, and the coefficient $\alpha(x, y)$ takes different values inside and outside this region. The specific setting is as follows.

Case 1.3:

$$\alpha(x, y) = \begin{cases} 2.5, & (x, y) \in U_2, \\ 3, & (x, y) \in U \setminus U_2. \end{cases} \tag{3.7}$$

For Case 1.3, the Stage 1 used tanh layers $[3, 100, \ldots, 100, 1]$ with eight hidden layers for $\hat{u}$, tanh layers $[2, 20, 20, 20, 20, 20, 1]$ for $\hat{\theta}_p$, Adam for 2.0×10^5 epochs, learning rates 10^{-4} for both networks, Sobol PDE batches of 40000 points refreshed every 200 epochs, 3600 snapshot points per frame, and $100 \times 50 = 5000$ free-surface points with same seed 101. In the same notation, the remaining implemented weights were $\gamma_1 = \gamma_2 = \gamma_3 = 0.1$. The Case 1.3 detector used a 60×60 patch grid in $[0.55, 1.10] \times [0.05, 0.40]$, and the recorded refinement used 1000 iterations with learning rate 5×10^{-4}. The training data uses only the reference solutions for the three time slices $t = 0$, $t = 0.015$, and $t = 0.15$.

The quantitative results of the proposed JVC-PINNs framework for three cases are summarized in Table 1-4. Specifically, Table 1 reports the two-stage coefficient inversion results, where the Stage 1 column gives the admissible coefficient intervals inferred from the GWS-PINNs samples and GMM-BDMC statistical learner, and the Stage 2 column gives the refined hard piecewise-constant estimates obtained by CCD-PINNs. Table 2 presents the temporal change-point detection results for one-dimensional time-



a: Reference solution t=0 b: Predicted solution t=0 c: Absolute error t=0

d: Reference solution t=0.15 e: Predicted solution t=0.15 f: Absolute error t=0.15

g: Parameter reference value h: Parameter inverse result i: Stage 1 absolute error

j: Parameter estimate result k: Stage 2 absolute error l: Change boundary detection

Figure 3: Numerical results for the wave equation with discontinuously 2D space-varying coefficient $\alpha(x, y)$.

varying coefficients, including the candidate change-point intervals from Stage 1 and the refined change-point estimates from Stage 2. For spatially varying coefficients, treating the adjacent boundaries of two platforms with different coefficients as closed curve functions in a 2D plane, Table 3 reports the MSE of the detected jump boundaries, measuring the discrepancy between the predicted discontinuity interfaces and the reference interfaces. In addition, Table 4 compares the PDE solution approximation errors of the main-network in the two stages. The results of the subsequent examples are listed in these four tables.

For Case 1.3, the comparison between the reconstructed solution from the second-stage main-network $\tilde{u}$ and the reference solution, together with the corresponding absolute error, is shown in the first two rows of Figure 3, where two representative time instants $t = 0$ and $t = 0.15$ are selected. The spatial coefficient inversion results are presented in the third and fourth rows of Figure 3, including the Stage 1 relaxed continuous approximation, the Stage 2 hard piecewise-constant reconstruction, the admissible coefficient intervals and candidate discontinuity region inferred by GMM-BDMC, and the comparison between the predicted jump boundary and the reference discontinuity boundary. The Stage 1 result, produced by the GWS-PINNs coefficient sub-network, captures the global spatial distribution of the coefficient but smooths the discontinuity near the interface between U_2 and $U \setminus U_2$. Based on the admissible coefficient intervals and candidate discontinuity region supplied by GMM-BDMC, the Stage 2 CCD-PINNs refinement constrains the possible values of the two spatial coefficient states and sharpens the spatial jump interface into a hard piecewise-constant estimator. The reference boundary is determined by the true spatial partition between U_2 and $U \setminus U_2$, while the predicted boundary is obtained from the refined Stage 2 hard classification or piecewise-constant coefficient reconstruction. The comparison shows that the proposed framework can recover not only the two discrete coefficient levels but also the spatial interface separating different parameter states. Therefore, the two-stage structure is essential, Stage 1 provides a smooth coefficient sampler suitable for statistical mixture modeling, whereas Stage 2 sharpens the transition and produces an explicit discontinuous coefficient reconstruction.

These wave equation examples demonstrate that the proposed JVC-PINNs framework can automatically distinguish constant coefficients from jump-varying coefficients through the inferred number of GMM components $\widehat{K}$. When $\widehat{K} = 1$, no change point or interface is introduced, and the framework reduces to a constant-coefficient inverse problem. When $\widehat{K} > 1$, the statistically inferred spatiotemporal coefficient and change-point candidate intervals or change-interface regions are passed to CCD-PINNs for constrained refinement. As a result, the relaxed continuous approximation from Stage 1 is converted into an interpretable hard piecewise-constant estimator in Stage 2. The successful extension from temporal jumps to spatial discontinuity interfaces further confirms the scalability of the proposed framework for mutli-dimensional PDE inverse problems. Additional PDE types are considered in the following subsections to further examine the robustness and generality of the method.

3.2. Heat Equation

The reaction-diffusion model, also known as the Fisher equation, is considered as a 1+1D heat equation with a time-varying diffusion coefficient. In the following model, $c(t) \geq 0$ denotes the diffusion parameter, which changes over time. This example is taken from [39], and the governing equation is given by

$$\begin{cases} u_t = c(t)u_{xx} + u - u^2, & (x,t) \in U \times (0,T], \\ u(x,t) = 0, & (x,t) \in \partial U \times (0,T], \\ u(x,0) = g(x), & x \in U. \end{cases} \tag{3.8}$$

Let $U = [-6,6]$, $T = 10$, and the initial function be

$$g(x) = \begin{cases} \exp\big(10(x+1)\big), & x < -1, \\ 1, & -1 \leq x \leq 1, \\ \exp\big(-10(x+1)\big), & x > 1. \end{cases} \tag{3.9}$$

This is a non-smooth initial value scenario and two different scenarios of time-varying coefficients are considered.

Case 2.1:

$$c(t) = \begin{cases} 0.2, & t \in [0,5), \\ 0.1, & t \in [5,10]. \end{cases} \tag{3.10}$$

Case 2.2:

$$c(t) = \begin{cases} 0.05, & t \in [0,2) \cup [8,10], \\ 0.1, & t \in [2,4) \cup [6,8), \\ 0.2, & t \in [4,6). \end{cases} \tag{3.11}$$

For Case 2.1 and Case 2.2, $\theta_p = c(t)$ on $(t,x) \in [0,10] \times [-6,6]$. Case 2.1 used main-network layers $[2,50,50,50,50,1]$ and coefficient-network layers $[1,2,2,2,2,2,1]$. Case 2.2 used main-network layers $[2,20,\ldots,20,1]$ with 20 hidden layers and coefficient-network layers $[1,10,\ldots,10,1]$ with 10 hidden layers. Both cases used seed 314 and Adam optimizer, with Case 2.1 trained for 5.0×10^4 iterations and Case 2.2 trained for 2.0×10^5 iterations, learning rates 10^{-3} for $\hat{u}$ and 10^{-4} for $\hat{\theta}_p$, and exponential decay factors 0.9 and 0.8. The residual set had $50 \times 80 = 4000$ points, and the observation set had 4000 fixed randomly sampled points. Case 2.1 also used 100 initial-condition points and 200 boundary points, refreshed with the residual batch every 1000 iterations. Case 2.2 used weights were $\gamma_1 = 1$, and $\gamma_2 = \gamma_3 = 0$ due to the

non-smoothness of the initial value. Stage 2 used a hard-step $c(t)$ initialized from GMM-BDMC, with Adam learning rates 5×10^{-4} for $\tilde{u}$ and 10^{-3} for change points and heights. The configured Stage 2 budget was 2500 iterations.

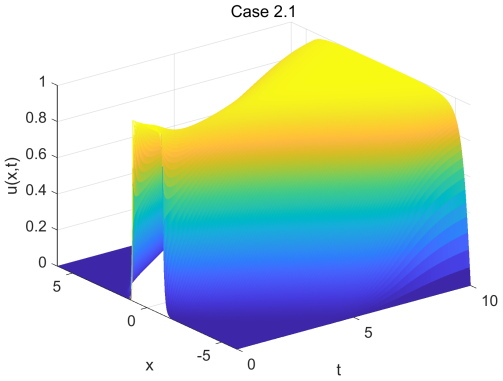
The solution plots for these two heat equation cases and the corresponding two-stage parameter inversion results for the diffusion coefficient $c(t)$ are shown in Figure 4. In the parameter inversion plots, the Stage 1 result represents the relaxed continuous coefficient approximation generated by the GWS-PINNs sub-network, while the Stage 2 result represents the hard piecewise-constant estimator refined by CCD-PINNs. The admissible coefficient intervals and candidate change-point intervals are inferred by the GMM-BDMC statistical learner and are used as constraints in the second-stage refinement. The reconstructed solution from the second-stage main-network $\tilde{u}$ and the corresponding absolute error with respect to the reference solution are also displayed in Figure 4. Table 1 reports the two-stage coefficient inversion results for $c(t)$, where the Stage 1 column gives the admissible coefficient intervals obtained from GMM-BDMC and the Stage 2 column gives the refined coefficient estimates from CCD-PINNs. Table 2 reports the temporal change-point detection results, including the candidate change-point intervals from Stage 1 and the refined change-point estimates from Stage 2. Table 4 presents the solution approximation errors of the main-network in both stages.

For Case 2.1, the GMM-BDMC learner identifies two coefficient states and one candidate change-point interval. Although the Stage 1 coefficient approximation smooths the discontinuity near the true jump time $t = 5$, it provides sufficient information for the statistical learner to infer the two diffusion states and localize the candidate transition region. The Stage 2 CCD-PINNs refinement then converts the relaxed continuous approximation into a sharp step-function estimator and produces a refined change point within the candidate interval.

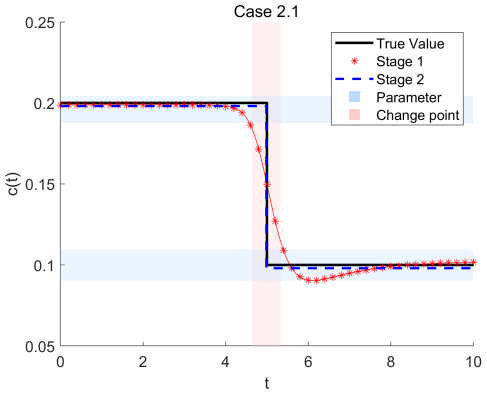
For Case 2.2, the diffusion coefficient switches among three discrete states over several temporal subintervals. The GMM-BDMC learner successfully identifies the three coefficient levels and multiple candidate change-point intervals. The Stage 1 curve captures the overall switching pattern but remains continuous near each jump. In contrast, the Stage 2 estimator recovers a hard piecewise-constant structure with refined temporal change points. These results indicate that the proposed JVC-PINNs framework is effective not only for a single jump but also for multi-state and multi-jump coefficient switching.

The results for the heat equation are consistent with those obtained for the wave equation. The first-stage GWS-PINNs sampler provides a continuous but informative approximation of the jump-varying coefficient, the GMM-BDMC statistical learner extracts the discrete coefficient states and candidate transition intervals, and the second-stage CCD-PINNs refinement yields an explicit piecewise-constant coefficient reconstruction. The reconstructed solution $\tilde{u}$ remains close to the reference solution, showing that the refined coefficient representation preserves the physical consistency of the PDE surrogate.

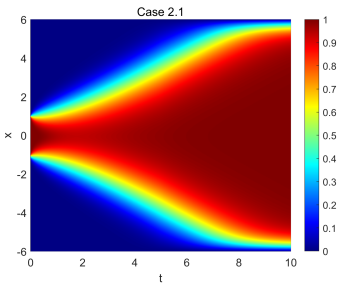
It is also worth emphasizing the role of the gradient-adaptive weighting strategy in GWS-PINNs.



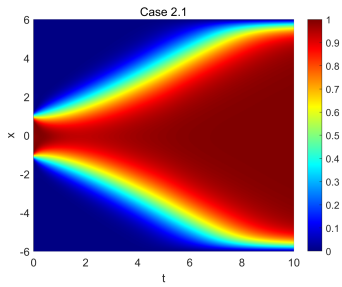
a: Spatiotemporal solution



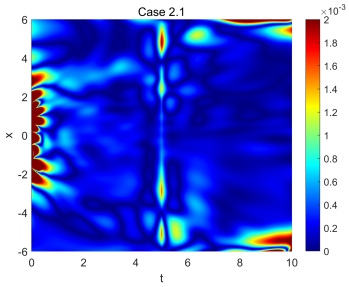
b: Parameter inverse result



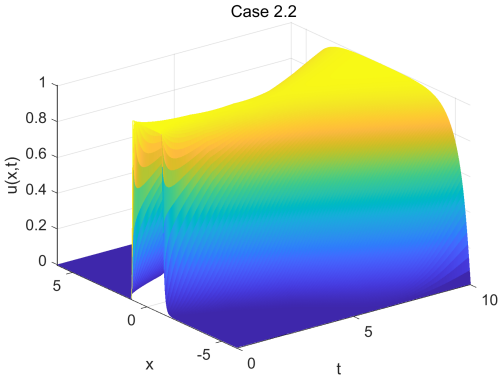
c: Reference solution



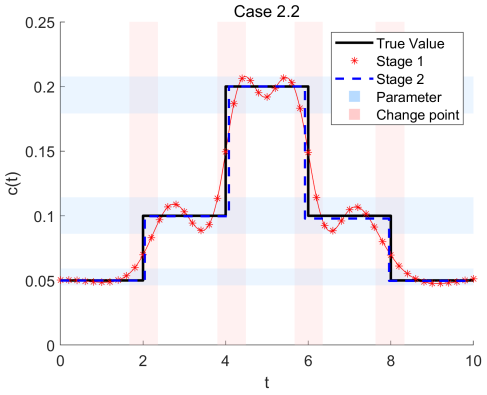
d: Predicted solution



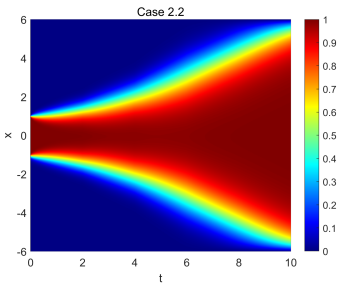
e: Absolute error



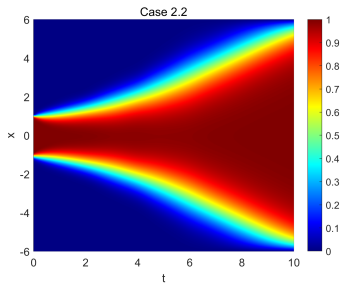
f: Spatiotemporal solution



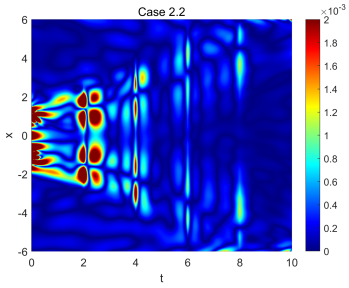
g: Parameter inverse result



h: Reference solution



i: Predicted solution



j: Absolute error

Figure 4: Numerical results for heat equations with discontinuously time varying coefficient $c(t)$.

The adaptive weight $w_{\text{res}}^{(i)}$ is not designed to increase the residual contribution near the coefficient jumps, which are usually hard-to-learn regions due to discontinuous parameter variation and possible non-smooth solution behavior. Instead, the weight becomes larger in smoother regions where the coefficient field varies slowly or remains constant. This design encourages the neural network to learn the physically consistent solution and coefficient behavior in easy-to-learn regions, while avoiding excessive fitting of the artificial transition layer near jumps. As a result, the main-network $\hat{u}(\mathbf{x}, t)$ and the coefficient sub-network $\hat{\theta}_p(\mathbf{x}, t)$ in Stage 1 can produce stable solution and coefficient surrogates. These surrogates then provide reliable samples for GMM-BDMC, enabling accurate inference of the coefficient states and candidate change-point intervals. Therefore, the gradient-adaptive weighting strategy plays an important role in improving the stability of the first-stage sampling and the accuracy of the subsequent Stage 2 constrained refinement.

3.3. Burgers' Equation

The Burgers' equation is a nonlinear second-order PDE that describes fluid motion in one-dimensional space under specific conditions. In this example, the coefficients $\lambda_1(t)$ and $\lambda_2(t)$ may exhibit temporal jumps. This example is taken from [34], and the corresponding 1+1D PDE is given by

$$\begin{cases} u_t = \lambda_1(t) u u_x + \lambda_2(t) u_{xx}, & (x,t) \in U \times (0,T], \\ u(x,t) = 0, & (x,t) \in \partial U \times (0,T], \\ u(x,0) = g(x), & x \in U. \end{cases} \tag{3.12}$$

Let $U = [-8, 8]$ and $T = 10$, with the initial value function

$$g(x) = \exp\left(-(x+1)^2\right). \tag{3.13}$$

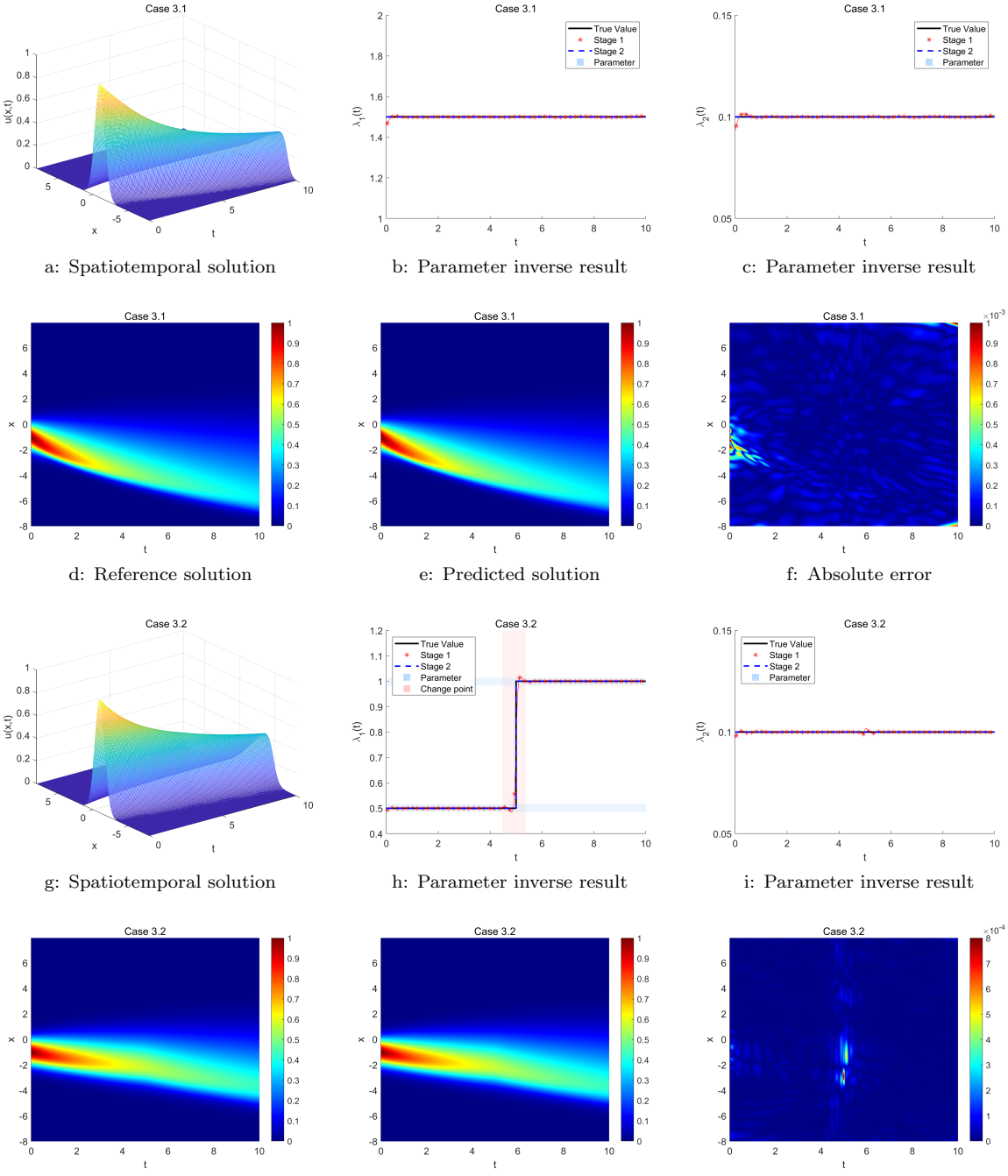
Four scenarios are considered, in which the parameters exhibit different types of temporal behavior, including constant coefficients, single-parameter jumps, multi-state switching, and simultaneous jumps of multiple coefficients.

Case 3.1:

$$\lambda_1(t) = 1.5, \quad \lambda_2(t) = 0.1, \quad t \in [0, 10]. \tag{3.14}$$

Case 3.2:

$$\lambda_1(t) = \begin{cases} 0.5, & t \in [0, 5), \\ 1, & t \in [5, 10], \end{cases} \qquad \lambda_2(t) = 0.1, \quad t \in [0, 10]. \tag{3.15}$$



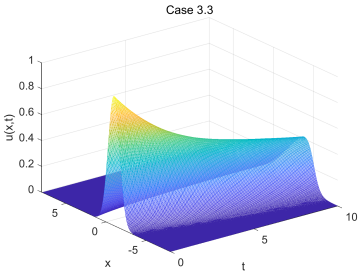
a: Spatiotemporal solution b: Parameter inverse result c: Parameter inverse result

d: Reference solution e: Predicted solution f: Absolute error

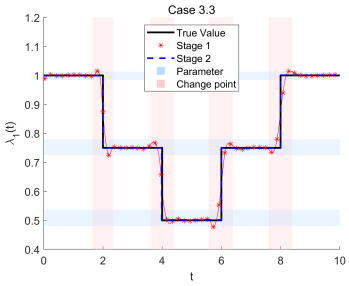
g: Spatiotemporal solution h: Parameter inverse result i: Parameter inverse result

j: Reference solution k: Predicted solution l: Absolute error

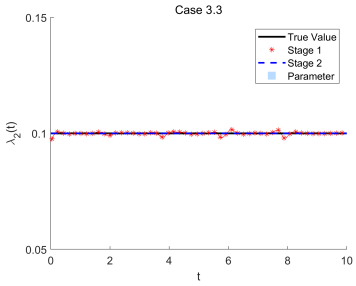
Figure 5: Numerical results for Burgers' equations with discontinuously time varying coefficients $\lambda_1(t)$ and $\lambda_2(t)$, from Case 3.1 to Case 3.2.



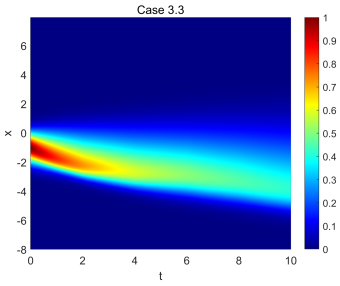
a: Spatiotemporal solution



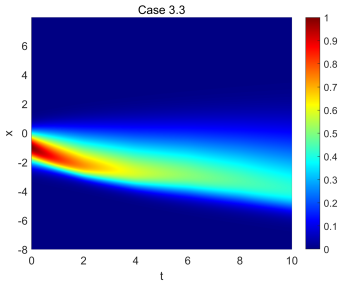
b: Parameter inverse result



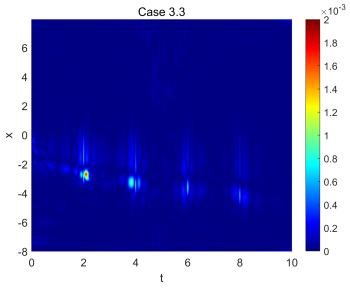
c: Parameter inverse result



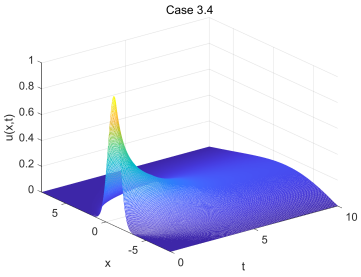
d: Reference solution



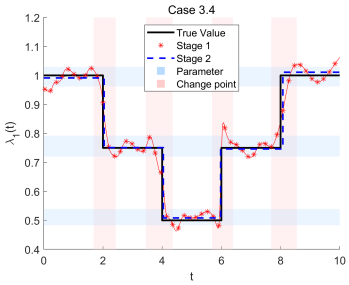
e: Predicted solution



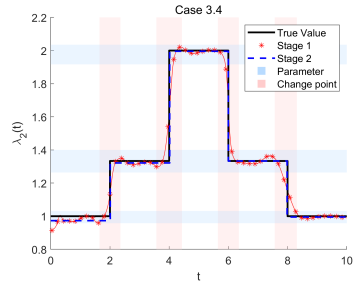
f: Absolute error



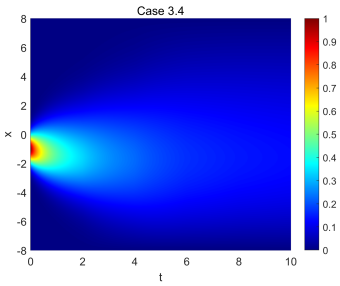
g: Spatiotemporal solution



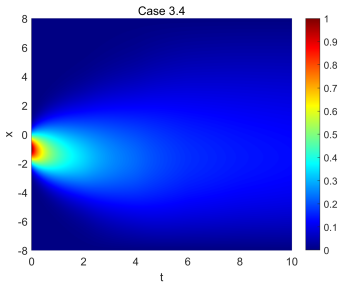
h: Parameter inverse result



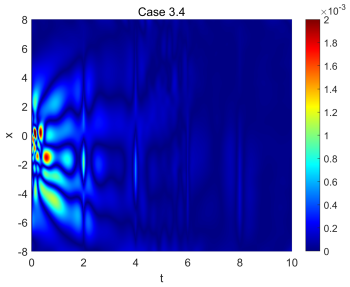
i: Parameter inverse result



j: Reference solution



k: Predicted solution



l: Absolute error

Figure 6: Numerical results for Burgers' equations with discontinuously time varying coefficients $\lambda_1(t)$ and $\lambda_2(t)$, from Case 3.3 to Case 3.4.

Case 3.3:

$$\lambda_1(t) = \begin{cases} 1, & t \in [0,2) \cup [8,10], \\ 0.75, & t \in [2,4) \cup [6,8), \\ 0.5, & t \in [4,6), \end{cases} \qquad \lambda_2(t) = 0.1, \quad t \in [0,10]. \tag{3.16}$$

Case 3.4:

$$\lambda_1(t) = \begin{cases} 1, & t \in [0,2) \cup [8,10], \\ 0.75, & t \in [2,4) \cup [6,8), \\ 0.5, & t \in [4,6), \end{cases} \qquad \lambda_2(t) = \begin{cases} 1, & t \in [0,2) \cup [8,10], \\ 4/3, & t \in [2,4) \cup [6,8), \\ 2, & t \in [4,6). \end{cases} \tag{3.17}$$

From Case 3.1 to Case 3.4, $\theta_p(t) = (\lambda_1(t), \lambda_2(t))$ on $(x,t) \in [-8,8] \times [0,10]$. The Stage 1 main-network had layers $[2, 128, 128, 128, 128, 128, 128, 1]$, and the coefficient network had layers $[1, 40, 40, 40, 40, 2]$, Adam for 2.0×10^5 iterations, learning rate 10^{-3} for both networks, decay factors 0.8 and 0.9 every 20000 iterations. The training set used a $50 \times 80 = 4000$ residual grid, 4000 random observations sampled with seed 314, 100 analytic initial-condition points with $u(x,0) = \exp[-(x+1)^2]$, and 200 homogeneous Dirichlet boundary points. The remaining loss weights were $\gamma_1 = 1$, $\gamma_2 = 0.5$ and $\gamma_3 = 0.5$. GMM-BDMC was applied separately to λ_1 and λ_2. Stage 2 used hard-step $\tilde{\lambda}_1(t)$ and $\tilde{\lambda}_2(t)$ initialized from Stage 1 stable-platform means and detector intervals. The full Stage 2 had a guarded 2500-iteration solution micro-refinement at learning rate 10^{-3} in main and sub-networks. For Case 3.5 and Case 3.6, since there are no discontinuous jumps in the parameter process, only Stage 1 was used. The main-network provided the solution approximation, and the coefficient sub-network provided the parameter samples for the sampling process, without Stage 2 CCD-PINNs refinement.

The solution images for these four Burgers' equation cases are shown in the first columns of Figure 5 and Figure 6. It can be observed that directly inferring the existence and locations of temporal coefficient jumps from the solution images is not intuitive. Therefore, these examples provide a meaningful test for the proposed JVC-PINNs framework in extracting hidden jump-varying physical coefficients from observed solution data. The two-stage parameter inversion results for $\lambda_1(t)$ and $\lambda_2(t)$ are presented in the second and third columns of Figure 5 and Figure 6. In these plots, the Stage 1 curves denote the relaxed continuous approximations generated by the GWS-PINNs coefficient sub-networks, while the Stage 2 curves denote the hard piecewise-constant estimators refined by CCD-PINNs. The admissible coefficient intervals and candidate change-point intervals are inferred by the GMM-BDMC statistical learner from the Stage 1 samples and are subsequently used as constraints in the Stage 2 refinement. Since two coefficients are involved, the statistical mixture modeling and constrained refinement are applied to $\lambda_1(t)$ and $\lambda_2(t)$ separately, allowing different parameters to have different numbers of states and different

change-point structures. The reconstructed solution images from the second-stage main-network $\tilde{u}$ and the corresponding absolute errors with respect to the reference solutions are displayed in the second and fourth rows of Figure 5 and Figure 6. Similarly, the quantitative results are summarized in Tables 1, Tables 2 and Tables 4.

Case 3.1 corresponds to the constant-coefficient setting, where both $\lambda_1(t)$ and $\lambda_2(t)$ remain unchanged over the entire time interval. For both coefficients, the GMM-BDMC learner identifies $\widehat{K} = 1$, indicating that no temporal change point is detected. Therefore, the second-stage CCD-PINNs refinement does not introduce any change-point variable and reduces to a constrained constant-coefficient inverse estimator. This confirms that the proposed framework can automatically distinguish constant coefficients from jump-varying coefficients and does not artificially create discontinuities when the underlying parameter is constant.

Case 3.2 considers a single temporal jump in $\lambda_1(t)$, while $\lambda_2(t)$ remains constant. The GMM-BDMC learner identifies two states for $\lambda_1(t)$ and one state for $\lambda_2(t)$. Accordingly, a candidate change-point interval is introduced only for $\lambda_1(t)$, while no change point is introduced for $\lambda_2(t)$. The Stage 1 approximation of $\lambda_1(t)$ captures the transition behavior but smooths the discontinuity near the jump time. The Stage 2 refinement converts this relaxed approximation into a sharp step-function estimator and produces an accurate refined change point.

Case 3.3 contains multi-state switching in $\lambda_1(t)$ and a constant $\lambda_2(t)$. The proposed framework identifies multiple coefficient states and several candidate change-point intervals for $\lambda_1(t)$, while automatically detecting that $\lambda_2(t)$ has only one constant state. The Stage 2 estimator accurately reconstructs the piecewise-constant structure of $\lambda_1(t)$ and preserves the constant behavior of $\lambda_2(t)$. This case demonstrates that the method can handle mixed situations in which only part of the physical coefficients are jump-varying.

Case 3.4 further increases the difficulty by allowing both $\lambda_1(t)$ and $\lambda_2(t)$ to switch among multiple states. The statistical learner is applied to the two parameters separately and detects the corresponding state structures and candidate change-point intervals. The Stage 2 CCD-PINNs refinement then produces hard piecewise-constant reconstructions for both coefficients. The results show that the proposed method remains effective when multiple PDE coefficients undergo simultaneous discontinuous temporal variations.

The previous examples have covered parameter non-continuous varying scenarios with no change points, a single parameter with a single change point, a single parameter with multiple change points, and multiple parameters with multiple change points. The proposed framework incorporates two additional types of parameter continuous variation patterns, trigonometric function-based and abrupt transition changes. These two extra scenarios of continuously time-varying coefficients in Burgers' equations are set as

Case 3.5:

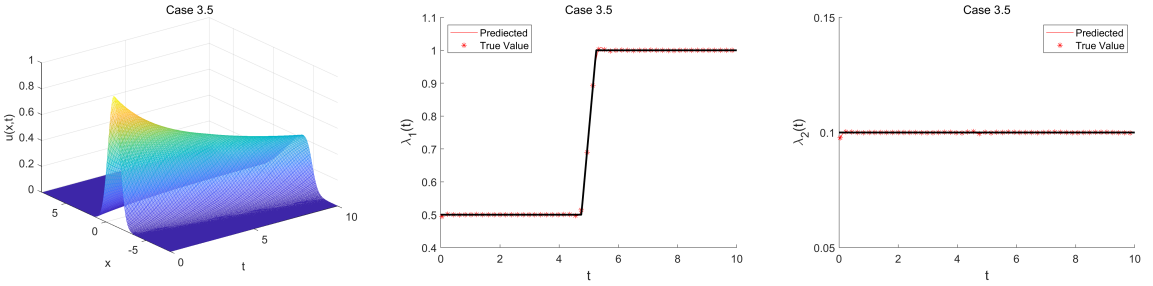
$$\lambda_1(t) = \begin{cases} 0.5, & 0 \le t < \dfrac{305}{64}, \\ \dfrac{64}{65}t - \dfrac{109}{26}, & \dfrac{305}{64} \le t < \dfrac{675}{128}, \\ 1, & \dfrac{675}{128} \le t \le 10. \end{cases} \quad \lambda_2(t) = 0.1, \quad t \in [0, 10]. \tag{3.18}$$

Case 3.6:

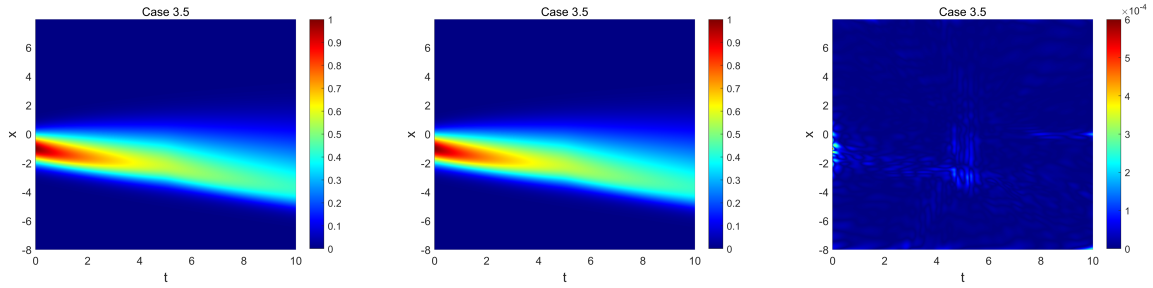
$$\lambda_1(t) = -1 - \frac{\sin t}{4}, \quad \lambda_2(t) = 0.1, \quad t \in [0, 10]. \tag{3.19}$$

The sampling results of the GWS-PINNs algorithm for the two discontinuously time varying coefficient $\lambda_1(t)$ and constant coefficient $\lambda_2(t)$ of the Burgers' equation are presented in the second and third columns, the first and third rows of Figure 7, respectively. Comparisons of the predictions of the solution images based on statistical inference results and the absolute errors with respect to the reference solutions are shown in the second and fourth rows of Figure 7. Both cases attained more effective results than the discontinuous change scenario in numerical experiments, in terms of the only Stage 1 MSE of the equation solution, shown in Table 4. Subsequent comparative studies validate that GWS-PINNs, through their improved loss function formulation, produce more ideal sampling outcomes and deliver higher precision in coefficient estimation for both time-varying and time-invariant parameters. The adaptive weighting mechanism in the loss function enables more accurate identification of equation coefficients with jump discontinuities in PDE coefficients, demonstrating superior performance in parameter inversion tasks compared to existing variable-coefficient PINNs approaches.

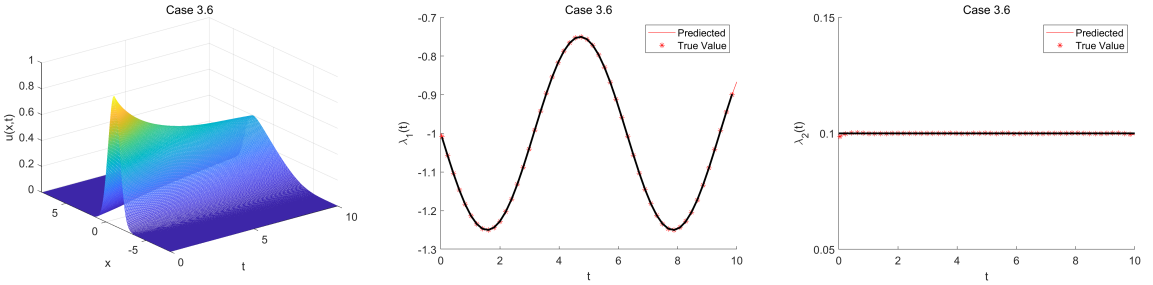
It should be noted that the proposed JVC-PINNs framework is most naturally suited to inverse problems for PDE systems with piecewise-constant coefficients over different temporal or spatial regions. Cases 3.5 and 3.6 are included to clarify the behavior of the method when the target coefficient is not genuinely discontinuous. In Case 3.5, $\lambda_1(t)$ contains a smooth transition segment and is therefore close to a piecewise-constant pattern but does not contain a sharp jump. In Case 3.6, $\lambda_1(t)$ is a continuously varying trigonometric function. These two examples show that, when no true discontinuity exists, the first-stage GWS-PINNs alone can provide accurate reconstructions of both the physical solution field and the varying coefficient field. The sub-network approximation errors for these continuous time-varying coefficient cases are reported in Table 5, confirming that Stage 1 GWS-PINNs can accurately recover both the varying coefficient $\lambda_1(t)$ and the constant coefficient $\lambda_2(t)$. The subsequent GMM-BDMC and CCD-PINNs components are specifically designed for piecewise-constant PDE coefficients. If they are forced onto continuously varying coefficients, they may introduce an inaccurate interpretation of the parameter variation behavior. Meanwhile, for the constant coefficient $\lambda_2(t)$ in these two cases, the GMM-BDMC inference gives $\widehat{K} = 1$, indicating that the statistical learner does not incorrectly introduce change points for a constant physical parameter.



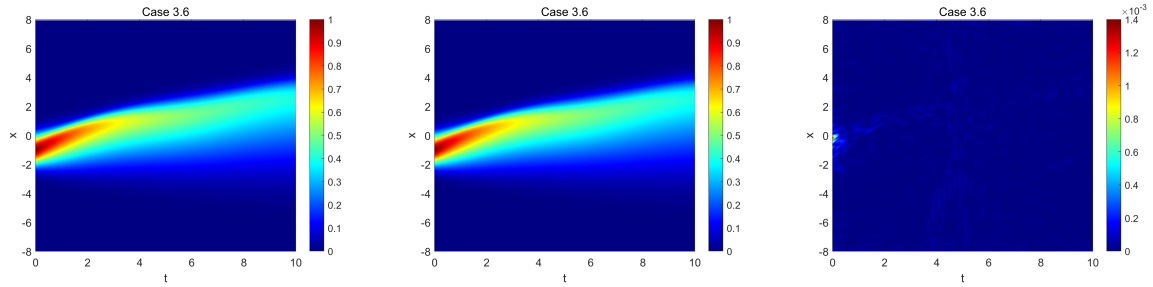
a: Spatiotemporal solution b: Parameter sample result c: Parameter sample result



d: Reference solution e: Predicted solution f: Absolute error



g: Spatiotemporal solution h: Parameter sample result i: Parameter sample result



j: Reference solution k: Predicted solution l: Absolute error

Figure 7: Numerical results for Burgers' equations with continuously time varying coefficients $\lambda_1(t)$ and $\lambda_2(t)$, from Case 3.5 to Case 3.6.

Overall, the Burgers' equation examples validate the effectiveness of the proposed JVC-PINNs framework for multi-parameter inverse problems with discontinuously time-varying coefficients. The Stage 1 GWS-PINNs sampler provides continuous but informative coefficient surrogates, the GMM-BDMC learner automatically determines the number of coefficient states and candidate change-point intervals, and the Stage 2 CCD-PINNs estimator refines the coefficient values and temporal discontinuities into explicit step-function representations. The accurate reconstruction of $\tilde{u}$ further confirms that the inferred jump-varying coefficients satisfy the governing PDE and are consistent with the observed dynamical behavior.

3.4. Navier-Stokes Equation

The Navier-Stokes equation is a fundamental model in nonlinear scientific research and characterizes the basic mechanical laws of real fluid flow. It is widely studied in fluid mechanics, applied mathematics, and numerical computation. A 2+1D incompressible Navier-Stokes equation with a time-varying viscosity coefficient $\nu(t)$ is considered in the following form

$$\begin{cases} u_t + (u \cdot \nabla)u + \nabla p = \nu(t)\Delta u + f, & (x, y, t) \in U \times (0, T], \\ \nabla \cdot u = 0, & (x, y, t) \in U \times (0, T], \\ u(x, y, 0) = u_0(x, y), & (x, y) \in U, \\ u(x, y, t) = 0, & (x, y, t) \in \partial U \times (0, T], \end{cases} \tag{3.20}$$

where $\nu(t) > 0$ denotes the viscosity coefficient, and $u = (u_1(x, y, t), u_2(x, y, t)) \in \mathbb{R}^2$ represents the velocity field. The initial condition is given by

$$u_0(x, y) = \big(g(x, y), g(x, y)\big) \in \mathbb{R}^2, \tag{3.21}$$

where

$$g(x, y) = -200\Big(x^2(1 - x)^2\Big) \cdot \Big(y(1 - y)^2 - y^2(1 - y)\Big). \tag{3.22}$$

The function $p(x, y, t) \in \mathbb{R}$ represents the fluid pressure, with the initial condition

$$p(x, y, 0) = \cos(2\pi y) \cdot \big(\pi \sin(\pi x) - 2\big). \tag{3.23}$$

The external force is denoted by $f(x, y, t) \in \mathbb{R}^2$. In this experiment, $U = [0, 1] \times [0, 1] \subset \mathbb{R}^2$, $T = 1$, and $f \equiv 0$ are used. This example is taken from [43]. The viscosity coefficient $\nu(t)$ is inversely related to the Reynolds number. Therefore, the jump varying of $\nu(t)$ may cause abrupt changes in the Reynolds number, which can bring additional challenges to numerical computation.

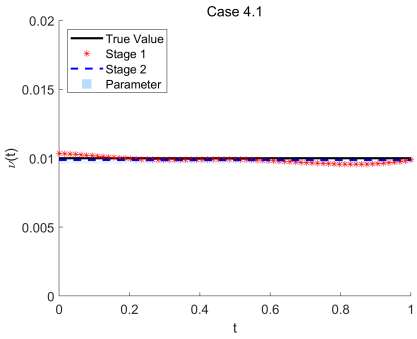
For the time-varying viscosity coefficient $\nu(t)$, eight scenarios are set as

$$
\begin{aligned}
&\textbf{Case 4.1:} \quad \nu(t) = 0.01, \quad t \in [0,1], \\
&\textbf{Case 4.2:} \quad \nu(t) = 0.01, \quad t \in [0,0.5], \quad \nu(t) = 0.02, \quad t \in [0.5,1], \\
&\textbf{Case 4.3:} \quad \nu(t) = 0.01, \quad t \in [0,0.5], \quad \nu(t) = 0.03, \quad t \in [0.5,1], \\
&\textbf{Case 4.4:} \quad \nu(t) = 0.01, \quad t \in [0,0.5], \quad \nu(t) = 0.04, \quad t \in [0.5,1], \\
&\textbf{Case 4.5:} \quad \nu(t) = 0.01, \quad t \in [0,0.5], \quad \nu(t) = 0.05, \quad t \in [0.5,1], \\
&\textbf{Case 4.6:} \quad \nu(t) = 0.01, \quad t \in [0,0.5], \quad \nu(t) = 0.06, \quad t \in [0.5,1], \\
&\textbf{Case 4.7:} \quad \nu(t) = 0.01, \quad t \in [0,0.5], \quad \nu(t) = 0.08, \quad t \in [0.5,1], \\
&\textbf{Case 4.8:} \quad \nu(t) = 0.01, \quad t \in [0,0.5], \quad \nu(t) = 0.1, \quad t \in [0.5,1].
\end{aligned}
\tag{3.24}
$$

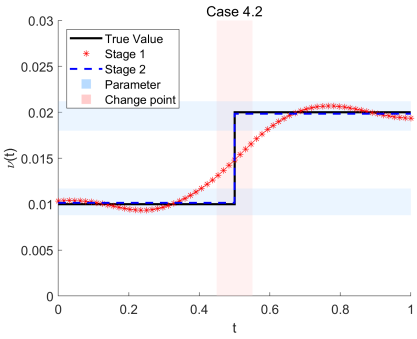
From Case 4.1 to Case 4.8, $\theta_p = \nu(t)$ for the two-dimensional incompressible Navier-Stokes system. The solution main-network for (u, v, p) used layers $[3, 20, 20, 20, 20, 20, 20, 3]$, and the viscosity parameter sub-network $\nu(t)$ used layers $[1, 20, 20, 1]$. With seed 314, Adam for 20000 iterations, learning rates 10^{-3} for the main-network and 8×10^{-4} for the sub-network with reduce factor 0.70, 5000 residual points, 5000 observation points, 1024 initial-condition points, and 4×512 boundary points. Data batches were refreshed every 5000 iterations, logs were written every 100 iterations, and full evaluation was performed every 500 iterations. The loss weights were $\gamma_1 = 1$ for the u and v residual equations, $\gamma_2 = \gamma_3 = 100$ for the u and v initial and boundary data terms, zero pressure data weights. GMM-BDMC used the common settings above with minimum variance 10^{-8} and $\alpha_f = 0.95$. Stage 2 represented $\tilde{\nu}(t)$ as a hard step function, used Adam for 5000 iterations, used learning rates 5×10^{-4} in main-network for $\tilde{u}$ and 5×10^{-3} for change points and heights in sub-network.

The two-stage viscosity coefficient inversion results for these eight cases are shown in Figure 8. The Stage 1 result corresponds to the relaxed continuous approximation generated by the GWS-PINNs coefficient sub-network. This stage provides continuous samples of $\nu(t)$ over the temporal domain and supplies the statistical input for GMM-BDMC. The GMM-BDMC learner then automatically infers the number of viscosity states, the admissible coefficient intervals, and the candidate change-point interval. The Stage 2 result corresponds to the hard piecewise-constant estimator refined by CCD-PINNs under these statistical constraints.

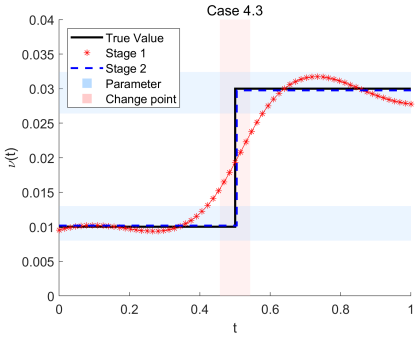
For Case 4.1, the viscosity coefficient remains constant over the whole time interval. The GMM-BDMC learner identifies $\widehat{K} = 1$, indicating that no temporal change point is detected. Therefore, no change-point variable is introduced in the CCD-PINNs refinement, and the inverse problem reduces to a constrained constant-coefficient estimation task. For Cases 4.2-4.8, the viscosity coefficient switches from 0.01 to a larger value at $t = 0.5$. In these cases, GMM-BDMC identifies two viscosity states and provides a candidate change-point interval around the true transition time. The Stage 1 curves may



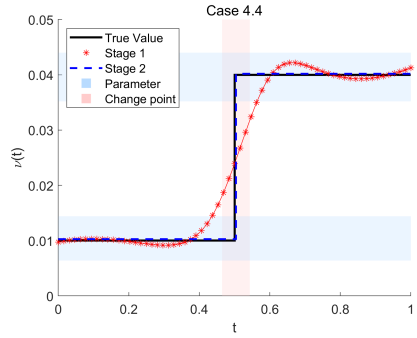
a: Parameter inverse result



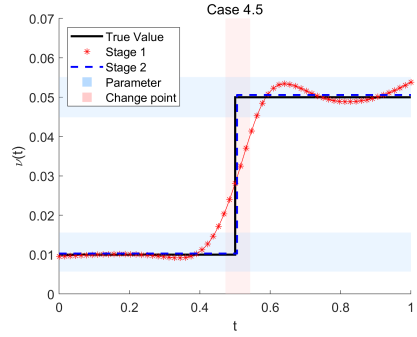
b: Parameter inverse result



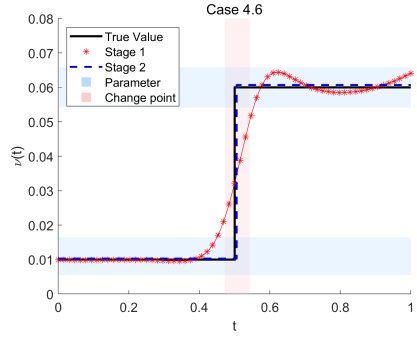
c: Parameter inverse result



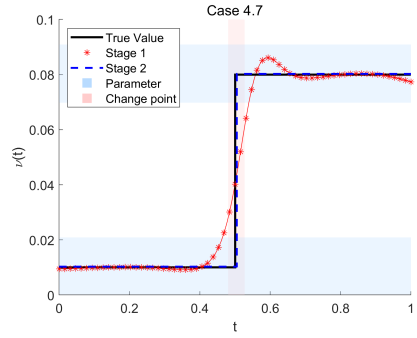
d: Parameter inverse result



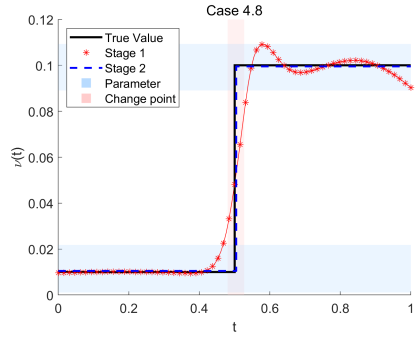
e: Parameter inverse result



f: Parameter inverse result

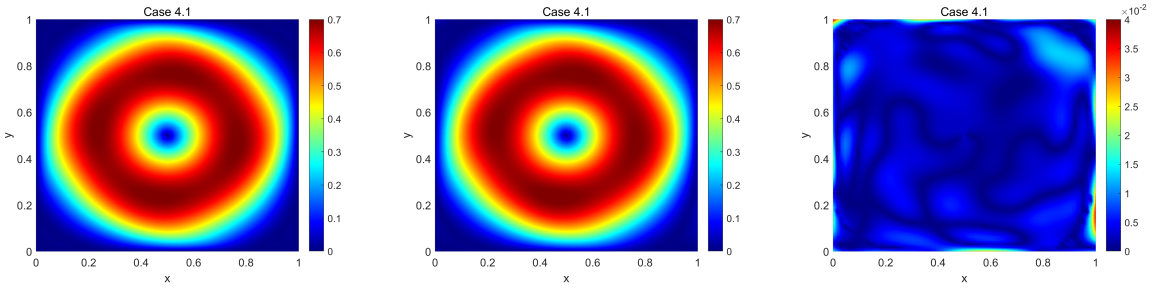


g: Parameter inverse result

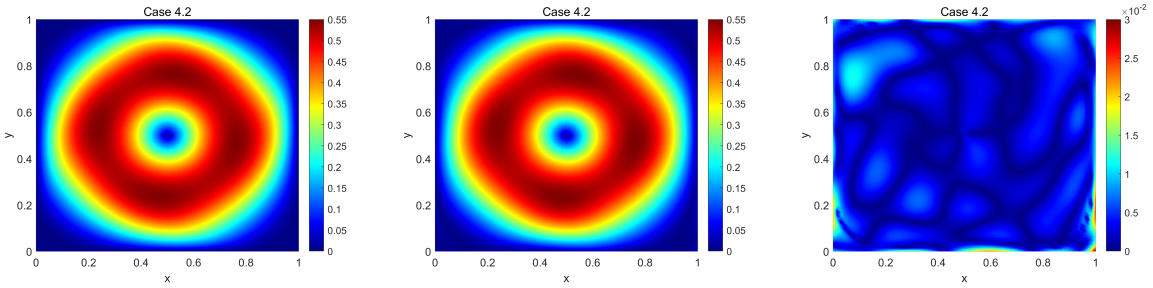


h: Parameter inverse result

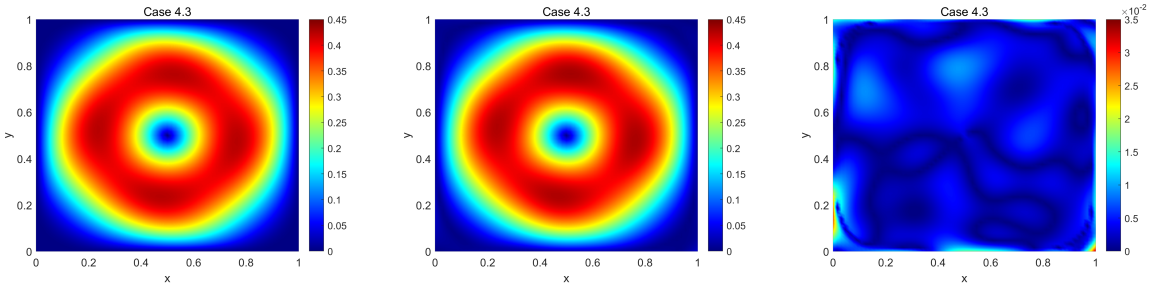
Figure 8: Numerical results for the Navier-Stokes equations with discontinuously time varying coefficient $\nu(t)$.



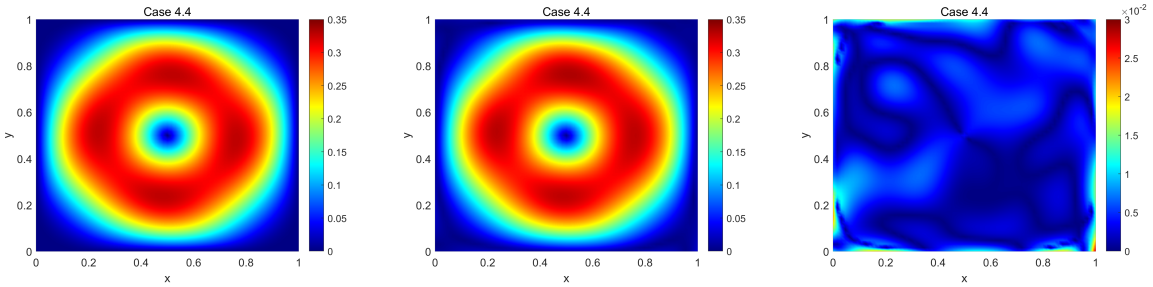
a: Reference solution b: Predicted solution c: Absolute error



d: Reference solution e: Predicted solution f: Absolute error

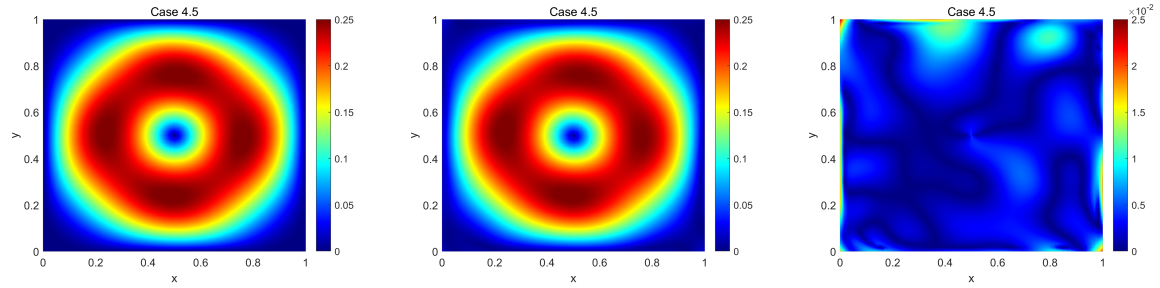


g: Reference solution h: Predicted solution i: Absolute error

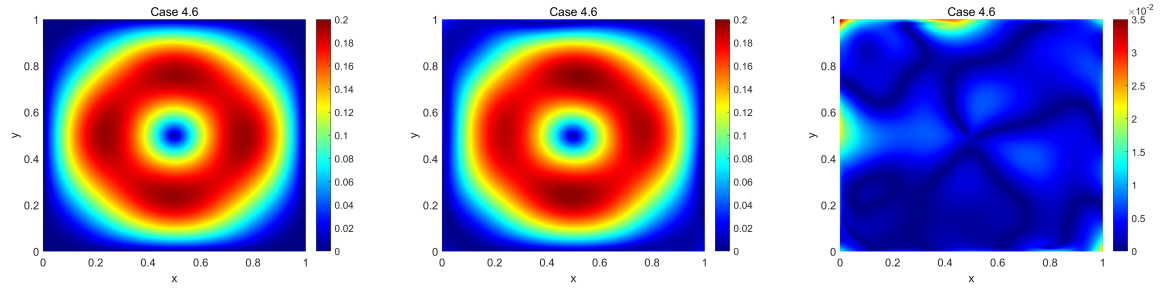


j: Reference solution k: Predicted solution l: Absolute error

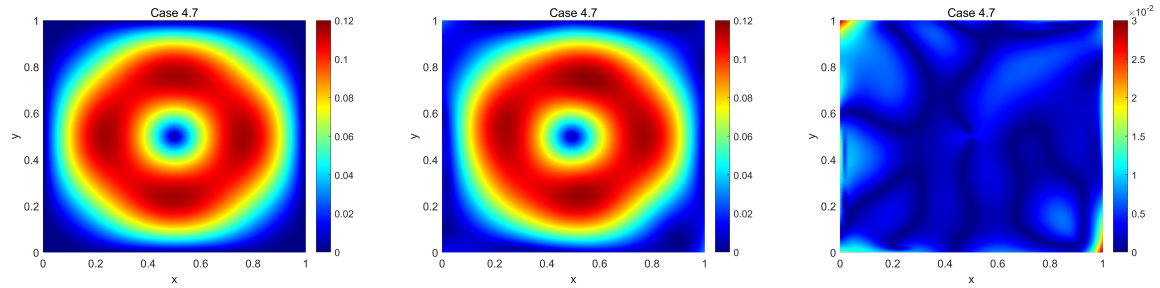
Figure 9: Numerical results for Navier-Stokes equations with discontinuously time varying coefficients $\nu(t)$, from Case 4.1 to Case 4.4.



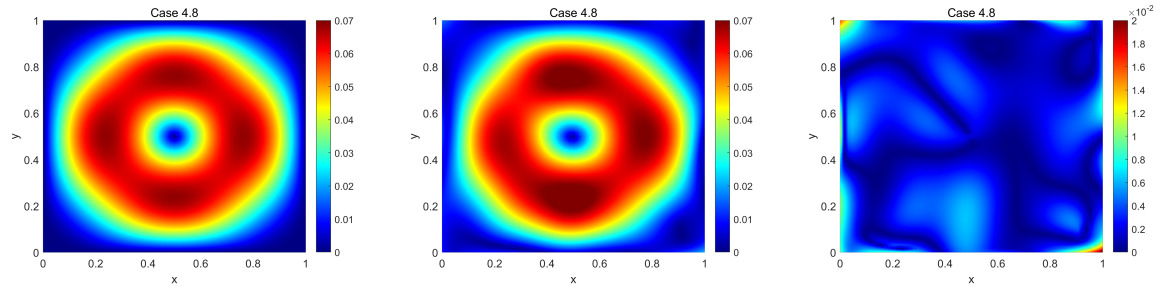
a: Reference solution b: Predicted solution c: Absolute error



d: Reference solution e: Predicted solution f: Absolute error



g: Reference solution h: Predicted solution i: Absolute error



j: Reference solution k: Predicted solution l: Absolute error

Figure 10: Numerical results for Navier-Stokes equations with discontinuously time varying coefficient $\nu(t)$, from Case 4.5 to Case 4.8.

present smooth transition layers near the jump due to the continuity of the neural approximation, while the Stage 2 results recover sharp step-function estimators and refined change points.

The quantitative coefficient estimation results are reported in Table 1. The temporal change-point detection results are presented in Table 2, where the Stage 1 column gives the candidate change-point intervals inferred by GMM-BDMC and the Stage 2 column gives the refined change-point estimates obtained by CCD-PINNs. The solution approximation errors of the main-network in both stages are summarized in Table 4. For the Navier-Stokes equation, the solution MSE reported in Table 4 is computed only for the velocity field $\mathbf{u} = (u_1, u_2)$, and the pressure field p is not included. These results show that the proposed framework can accurately estimate the viscosity coefficient across different jump magnitudes, from a small change in Case 4.2 to a large change in Case 4.8. For visualization of the flow field, the scalar velocity magnitude is used as

$$\|\mathbf{u}\| := \sqrt{u_1^2 + u_2^2}. \tag{3.25}$$

Taking into account the cumulative effect of nonlinear error propagation, a representative evolutionary end-time instant $t = 1$ is selected to display the reconstructed solution fields. The solution reconstructed by the second-stage main-network $\tilde{\mathbf{u}}$, the reference solution, and the corresponding absolute error are shown in Figure 9 and Figure 10. These figures demonstrate that the refined solution network can reconstruct the velocity magnitude with small error even when the hidden viscosity coefficient undergoes discontinuous temporal changes. Meanwhile, a gradual degradation of the solution approximation accuracy can be observed as the viscosity coefficient ν decreases, which corresponds to an increase in the Reynolds number. This phenomenon is consistent with mainstream numerical methods for the Navier-Stokes equations, since lower viscosity generally enhances convection-dominated behavior and increases the numerical stiffness and complexity of the flow dynamics.

The Navier-Stokes examples further demonstrate the adaptability of the proposed JVC-PINNs framework to complex nonlinear spatiotemporal systems. The Stage 1 GWS-PINNs sampler provides stable continuous approximations of the viscosity coefficient, the GMM-BDMC learner automatically distinguishes constant and jump-varying cases through the inferred component number $\widehat{K}$, and the Stage 2 CCD-PINNs estimator refines both the viscosity values and the change point into an explicit piecewise-constant representation. The accurate reconstruction of $\tilde{\mathbf{u}}$ further confirms that the inferred jump-varying viscosity coefficients satisfy the governing PDE and are consistent with the observed dynamical behavior. These results suggest potential applications in fluid mechanics and aerodynamics, such as parameter inference from limited experimental data in wind tunnel simulations or flow systems modeled by Navier-Stokes equations.

3.5. Helmholtz Equation

The previous examples mainly focus on parabolic and hyperbolic PDEs. As another fundamental class of PDEs, elliptic equations are also considered to further validate the applicability of the proposed framework. Although elliptic problems do not contain a physical time variable, the spatial coefficient samples generated by the first-stage GWS-PINNs sub-network can still be flattened into a one-dimensional coefficient sample set. After this transformation, the GMM-BDMC statistical learner can be applied to infer the discrete coefficient states, admissible coefficient intervals, and candidate discontinuity regions. The second-stage CCD-PINNs then refines the hard piecewise-constant coefficient field and its spatial jump boundary under these statistical constraints.

A 2D Helmholtz equation with a 2D space-varying coefficient $k(x, y)$ is considered as a representative elliptic example as

$$\Delta u + k(x, y)^2 u = f(x, y), \quad (x, y) \in U \subset \mathbb{R}^2, \tag{3.26}$$

where $u(x, y) = (v(x, y), w(x, y)) \in \mathbb{R}^2$. This example is taken from [44]. The Sommerfeld-type radiation condition is given by

$$\left| \frac{\partial u}{\partial r} - \mathrm{i}\, k(x, y)\, u \right| = o\big(r^{-1/2}\big), \quad r \to \infty, \tag{3.27}$$

where $r = \sqrt{x^2 + y^2}$. In this experiment, the computational domain is set as

$$U = [-1, 1] \times [-1, 1], \tag{3.28}$$

and the right-hand side function is

$$f(x, y) = \begin{cases} -\dfrac{1}{2a\sqrt{\pi}} \exp\left[-\left(\dfrac{|(x, y) - (0.5, 0)|}{a} \right)^2 \right], & |(x, y) - (0.5, 0)| < 0.5, \\ 0, & |(x, y) - (0.5, 0)| \geq 0.5, \end{cases} \tag{3.29}$$

where $a = \pi / k_0$. In this numerical experiment, $k_0 = 20$ is used. A regular square open region $U_1 \subset U$ is located on the left side of the spatial domain, where the coefficient differs from that in the exterior region. The spatially varying coefficient $k(x, y)$ is set as follows.

Case 5.1:

$$k(x, y) = \begin{cases} \dfrac{k_0}{1.5}, & (x, y) \in U_1, \\ k_0, & (x, y) \in U \setminus U_1. \end{cases} \tag{3.30}$$

For Case 5.1, $\theta_p = k(x, y)$ on $(x, y) \in [-1, 1]^2$. Stage 1 networks used tanh networks. The complex-valued main-network used layers $[2, 60, 60, 60, 60, 60, 60, 60, 60, 2]$, and the coefficient network used layers $[2, 20, 20, 1]$. With seed 314, Adam for 2.0×10^5 iterations, learning rates 10^{-3} for both networks, reduce

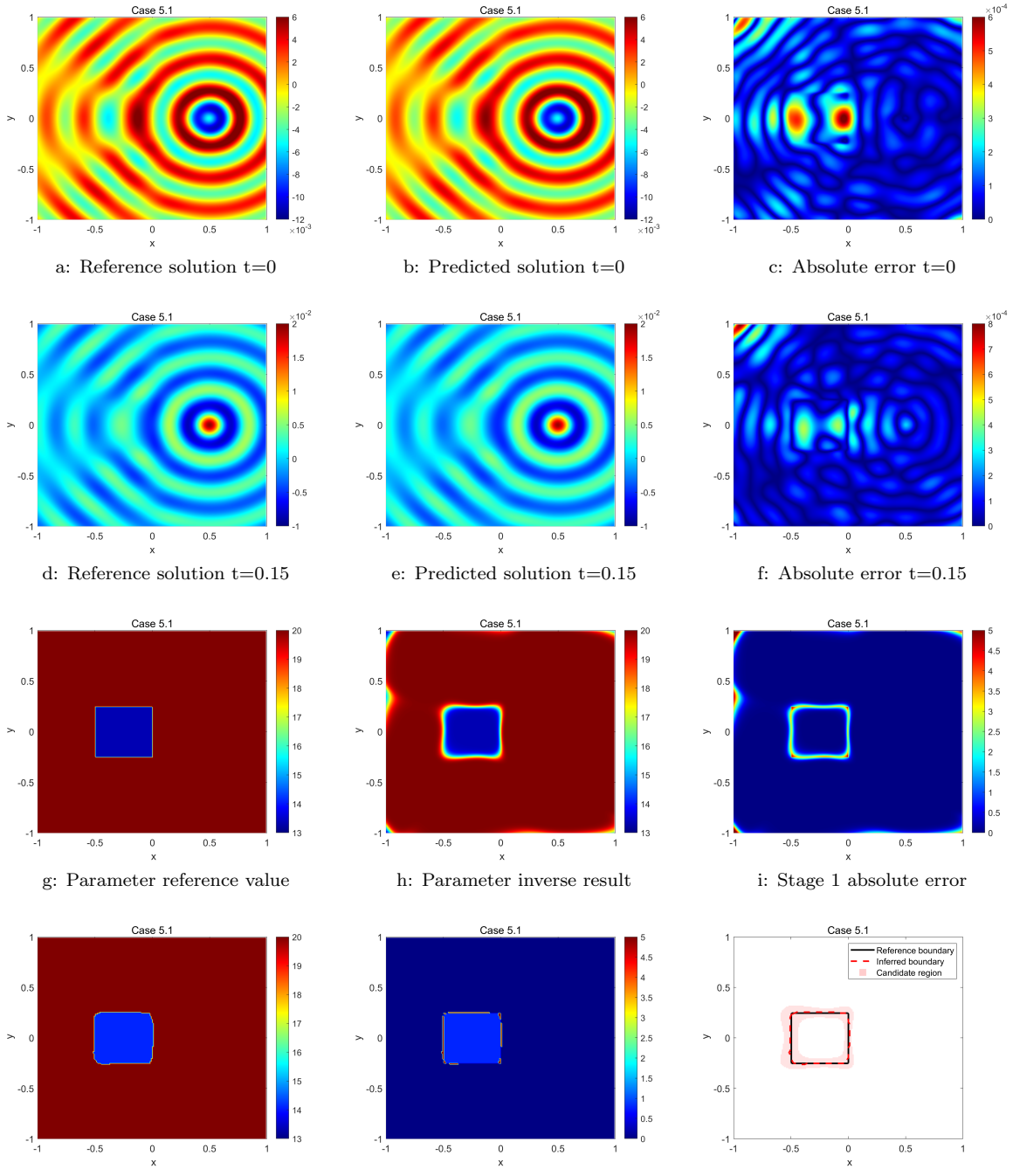
factor 0.6, 5000 interior residual/observation points, and 2048 Dirichlet boundary points. There were no separate initial-condition points, corresponding to $\gamma_1 = 1$, $\gamma_2 = 0$, $\gamma_3 = 1$. Stage 2 used a 32×32 patchwise hard field, applied GMM-BDMC in the box $[-0.8, 0.8] \times [-0.8, 0.8]$, and then refined the transferred main-network at learning rate 10^{-4} and sub-network at learning rate 10^{-3} for 20000 Adam iterations.

The comparison between the reconstructed solution from the second-stage main-network and the reference solution, together with the corresponding absolute error, is shown in the first two rows of Figure 11. The spatial coefficient inversion results are shown in the third and forth row of Figure 11, including the reference coefficient field, the Stage 1 relaxed continuous approximation produced by the GWS-PINNs coefficient sub-network, and the Stage 2 hard piecewise-constant reconstruction refined by CCD-PINNs. The admissible coefficient intervals inferred by GMM-BDMC constrain the possible values of the two coefficient states, while the candidate discontinuity region guides the refinement of the square jump boundary. The quantitative coefficient estimation results are reported in Table 1 and Table 2, the jump-boundary detection error is reported in Table 3, and the solution approximation errors of the main-network in the two stages are summarized in Table 4.

The results show that the proposed JVC-PINNs framework can accurately reconstruct both the solution field and the discontinuously varying spatial coefficient for the Helmholtz equation. The Stage 1 GWS-PINNs as coefficient sampler captures the global spatial distribution of $k(x, y)$ but smooths the discontinuity near the boundary of U_1. Based on the statistical constraints supplied by GMM-BDMC, the Stage 2 CCD-PINNs refinement estimator sharpens the transition and produces an explicit hard piecewise-constant coefficient estimator. The predicted jump boundary is close to the reference square interface, demonstrating the ability of the proposed framework to handle elliptic PDEs with spatially discontinuous coefficients.

From the spatially varying coefficient examples, the proposed JVC-PINNs framework successfully completes parameter estimation for PDEs with spatial jump coefficients in both irregular and regular subdomains. In addition, the MSEs of the identified discontinuity boundary functions are of the same order of magnitude for both the irregular case and the regular case, indicating that the proposed method maintains comparable boundary-reconstruction accuracy under different geometric structures. These results demonstrate that the combination of GWS-PINNs coefficient sampling, GMM-BDMC statistical inference, and CCD-PINNs constrained refinement is effective for multi-dimensional spatial parameter identification. This capability has significant potential for practical applications involving heterogeneous media.

Furthermore, Table 6 reports the computational time of the three main components of JVC-PINNs: the first-stage GWS-PINNs sampler, the GMM-BDMC statistical learner, and the second-stage CCD-PINNs estimator. The results show that, although JVC-PINNs adopts a two-stage framework with both



a: Reference solution t=0 b: Predicted solution t=0 c: Absolute error t=0

d: Reference solution t=0.15 e: Predicted solution t=0.15 f: Absolute error t=0.15

g: Parameter reference value h: Parameter inverse result i: Stage 1 absolute error

j: Parameter estimate result k: Stage 2 absolute error l: Change boundary detection

Figure 11: Numerical results for the the Helmholtz equation with discontinuously 2D space varying coefficient $k(x, y)$.

Table 1: Sampling and estimating results of sub-network in two stage PINNs.

Equation	Case	Parameter	True	Stage 1	Stage 2	Relative error
Wave	1.1	$\alpha(t)$	1	$[0.9997, 1.0001]$	0.9999	-0.0098%
	1.2	$\alpha(t)$	0.5	$[0.4727, 0.5362]$	0.4991	-0.1700%
			1	$[0.9516, 1.0222]$	0.9980	-0.1955%
	1.3	$\alpha(x, y)$	2.5	$[2.3359, 2.8350]$	2.5114	$+0.4572\%$
			3	$[2.9669, 3.0164]$	3.0000	$+0.0000\%$
Heat	2.1	$c(t)$	0.1	$[0.0904, 0.1095]$	0.0980	-2.0034%
			0.2	$[0.1875, 0.2044]$	0.1981	-0.9534%
	2.2	$c(t)$	0.05	$[0.0462, 0.0592]$	0.0498	-0.3936%
			0.1	$[0.0861, 0.1143]$	0.0988	-1.1741%
			0.2	$[0.1792, 0.2077]$	0.2000	$+0.0168\%$
Burgers	3.1	$\lambda_1(t)$	1.5	$[1.4957, 1.5036]$	1.4996	-0.0249%
		$\lambda_2(t)$	0.1	$[0.0994, 0.1006]$	0.1000	$+0.0021\%$
	3.2	$\lambda_1(t)$	0.5	$[0.4856, 0.5172]$	0.4998	-0.0387%
			1	$[0.9833, 1.0140]$	0.9998	-0.0152%
		$\lambda_2(t)$	0.1	$[0.0997, 0.1003]$	0.1000	-0.0183%
	3.3	$\lambda_1(t)$	0.5	$[0.4802, 0.5367]$	0.5013	$+0.2570\%$
			0.75	$[0.7250, 0.7796]$	0.7498	-0.0313%
			1	$[0.9837, 1.0126]$	0.9999	-0.0113%
		$\lambda_2(t)$	0.1	$[0.0994, 0.1006]$	0.1000	-0.0041%
	3.4	$\lambda_1(t)$	0.5	$[0.4833, 0.5388]$	0.5083	$+1.6584\%$
			0.75	$[0.7201, 0.7921]$	0.7483	-0.2311%
			1	$[0.9620, 1.0296]$	1.0003	$+0.0329\%$
		$\lambda_2(t)$	1	$[0.9578, 1.0314]$	0.9842	-1.5758%
			1.3333	$[1.2642, 1.4001]$	1.3274	-0.4474%
			2	$[1.9169, 2.0353]$	1.9958	-0.2116%
Navier-Stokes	4.1	$\nu(t)$	0.01	$[0.0095, 0.0101]$	0.0098	-2.0083%
	4.2	$\nu(t)$	0.01	$[0.0088, 0.0117]$	0.0101	$+1.4376\%$
			0.02	$[0.0180, 0.0212]$	0.0198	-0.7740%
	4.3	$\nu(t)$	0.01	$[0.0080, 0.0130]$	0.0102	$+1.7357\%$
			0.03	$[0.0264, 0.0324]$	0.0297	-0.8514%
	4.4	$\nu(t)$	0.01	$[0.0064, 0.0144]$	0.0103	$+2.6291\%$
			0.04	$[0.0352, 0.0440]$	0.0402	$+0.4476\%$
	4.5	$\nu(t)$	0.01	$[0.0057, 0.0156]$	0.0103	$+2.7598\%$
			0.05	$[0.0449, 0.0551]$	0.0506	$+1.1087\%$
	4.6	$\nu(t)$	0.01	$[0.0055, 0.0165]$	0.0103	$+2.8712\%$
			0.06	$[0.0541, 0.0658]$	0.0607	$+1.1240\%$
	4.7	$\nu(t)$	0.01	$[0.0002, 0.0209]$	0.0103	$+2.8796\%$
			0.08	$[0.0698, 0.0909]$	0.0802	$+0.3077\%$
	4.8	$\nu(t)$	0.01	$[0.0011, 0.0218]$	0.0105	$+4.7731\%$
			0.1	$[0.0891, 0.1093]$	0.0996	-0.4467%
Helmholtz	5.1	$k(x, y)$	13.3333	$[13.3333, 13.5019]$	13.3333	$+0.0001\%$
			20	$[19.6164, 20.0000]$	19.9734	-0.1329%

Table 2: Change-point detection results for 1D temporal coefficients of sub-network in two stage PINNs.

Equation	Case	Parameter	Change point	True	Stage 1	Stage 2	Relative error
Wave	1.2	$\alpha(t)$	τ_1	5	$[4.1750, 5.9950]$	5.0413	+0.8257%
Heat	2.1	$c(t)$	τ_1	5	$[4.6400, 5.3300]$	4.9846	−0.3074%
	2.2	$c(t)$	τ_1	2	$[1.6700, 2.3600]$	2.0416	+2.0781%
			τ_2	4	$[3.8000, 4.4900]$	4.0787	+1.9678%
			τ_3	6	$[5.6700, 6.3500]$	5.9211	−1.3145%
			τ_4	8	$[7.6300, 8.3300]$	7.9585	−0.5187%
Burgers	3.2	$\lambda_1(t)$	τ_1	5	$[4.4706, 5.3725]$	4.9995	−0.0093%
	3.3	$\lambda_1(t)$	τ_1	2	$[1.6471, 2.3529]$	2.0002	+0.0099%
			τ_2	4	$[3.6078, 4.3922]$	3.9838	−0.4054%
			τ_3	6	$[5.5686, 6.3922]$	6.0021	+0.0345%
			τ_4	8	$[7.6078, 8.3922]$	8.0029	+0.0368%
	3.4	$\lambda_1(t)$	τ_1	2	$[1.6863, 2.4314]$	2.0392	+1.9608%
			τ_2	4	$[3.4510, 4.3529]$	4.0392	+0.9804%
			τ_3	6	$[5.6863, 6.3922]$	5.9749	−0.4179%
			τ_4	8	$[7.6863, 8.5490]$	8.0784	+0.9804%
		$\lambda_2(t)$	τ_1	2	$[1.6471, 2.3529]$	2.0105	+0.5236%
			τ_2	4	$[3.5686, 4.4314]$	4.0184	+0.4612%
			τ_3	6	$[5.6471, 6.3529]$	5.9986	−0.0242%
			τ_4	8	$[7.5686, 8.3137]$	7.9827	−0.2159%
Navier-Stokes	4.2	$\nu(t)$	τ_1	0.5	$[0.4492, 0.5508]$	0.4998	−0.0489%
	4.3	$\nu(t)$	τ_1	0.5	$[0.4570, 0.5430]$	0.5049	+0.9883%
	4.4	$\nu(t)$	τ_1	0.5	$[0.4648, 0.5430]$	0.5040	+0.8037%
	4.5	$\nu(t)$	τ_1	0.5	$[0.4727, 0.5430]$	0.5056	+1.1242%
	4.6	$\nu(t)$	τ_1	0.5	$[0.4727, 0.5430]$	0.5060	+1.2078%
	4.7	$\nu(t)$	τ_1	0.5	$[0.4805, 0.5273]$	0.5050	+0.9965%
	4.8	$\nu(t)$	τ_1	0.5	$[0.4805, 0.5273]$	0.5047	+0.9405%

Table 3: Jump boundary detection MSE results for 2D spatial coefficients of sub-network in CCD-PINNs.

Equation	Case	Parameter	MSE	Equation	Case	Parameter	MSE
Wave	1.3	$\alpha(x, y)$	1.2592e-4	Helmholtz	5.1	$k(x, y)$	9.3683e-5

Table 4: MSE results of PDEs solution approximation of main-network in two stage PINNs.

Equation	Case	Stage 1	Stage 2	Equation	Case	Stage 1	Stage 2
Wave	1.1	1.3684e-6	1.3482e-6	Burgers	3.6	5.6432e-10	–
Wave	1.2	9.3052e-6	5.1713e-6	Navier-Stokes	4.1	1.7214e-5	1.5892e-5
Wave	1.3	1.1071e-4	1.0886e-4	Navier-Stokes	4.2	2.1269e-5	2.1226e-5
Heat	2.1	6.4613e-6	6.3578e-6	Navier-Stokes	4.3	2.9634e-5	2.0634e-5
Heat	2.2	1.8888e-6	1.7903e-6	Navier-Stokes	4.4	3.4843e-5	2.3094e-5
Burgers	3.1	1.3476e-8	4.8732e-9	Navier-Stokes	4.5	4.2367e-5	2.6175e-5
Burgers	3.2	7.8007e-10	7.5590e-10	Navier-Stokes	4.6	4.8325e-5	2.3883e-5
Burgers	3.3	3.6277e-9	3.5863e-9	Navier-Stokes	4.7	5.4288e-5	3.0744e-5
Burgers	3.4	4.0232e-8	3.9129e-8	Navier-Stokes	4.8	5.6403e-5	3.0631e-5
Burgers	3.5	8.5891e-10	–	Helmholtz	5.1	1.3884e-9	7.9232e-10

Table 5: Sub-network approximation error of GWS-PINNs for continuous time-varying coefficients in Burgers' equations.

Equation	Case	Parameter	MSE	Equation	Case	Parameter	MSE
Burgers	3.5	$\lambda_1(t)$	7.5088e-6	Burgers	3.6	$\lambda_1(t)$	3.2288e-7
		$\lambda_2(t)$	8.3945e-8			$\lambda_2(t)$	3.7786e-8

Table 6: Computational time of GWS-PINNs, GMM-BDMC and CCD-PINNs in all numerical experiments.

Equation	Case	GWS-PINNs	GMM-BDMC	CCD-PINNs	Total
Wave	1.1	2417.4	10.1	98.6	2526.1
	1.2	2481.7	19.5	103.8	2605.1
	1.3	12600.3	37.2	105.4	12742.9
Heat	2.1	3320.0	20.2	175.7	3515.9
	2.2	13265.0	26.2	181.4	13472.6
Burgers	3.1	8064.8	19.8	107.8	8192.4
	3.2	8082.1	20.4	99.6	8202.1
	3.3	8076.4	20.2	101.1	8197.7
	3.4	8108.0	20.2	102.0	8230.2
Navier-Stokes	4.1	4160.3	17.7	704.0	4882.0
	4.2	4255.1	17.5	725.6	4998.2
	4.3	4209.3	17.7	674.6	4901.6
	4.4	4290.4	17.6	694.2	5002.2
	4.5	4269.1	17.9	697.6	4984.5
	4.6	4194.9	17.6	755.2	4967.7
	4.7	4246.9	18.0	858.3	5123.2
	4.8	4194.0	17.8	614.5	4826.3
Helmholtz	5.1	7581.1	84.2	941.7	8606.9

solution and coefficient networks, its total computational cost remains comparable to that of a single-stage neural-network solver. Most of the cost is spent on the first stage joint physics-informed training, while GMM-BDMC incurs only a small overhead since it operates on coefficient samples rather than the full PDE solution space. The second stage CCD-PINNs is also efficient because it uses transfer learning from the trained GWS-PINNs solution network and restricts the optimization of coefficients and jump locations to the admissible intervals and candidate regions inferred by GMM-BDMC. Therefore, the proposed framework improves coefficient identification and discontinuity localization with only moderate additional computational cost, supporting its practical applicability to PDE inverse problems with jump-varying coefficients.

In summary, the core idea of this framework is to first use a PINN with a coefficient subnetwork and gradient adaptive weighting to learn a smooth approximation of a jump varying coefficient, then apply GMM and BDMC to automatically identify the discrete coefficient states and candidate jump regions, and finally build a constrained piecewise constant PINN to refine the coefficient values and discontinuity locations. The main research value lies in the integrated framework that combines PINN based sampling, Bayesian mixture model detection, and constrained PINN refinement, enabling accurate

identification and reconstruction of unknown jump coefficients in PDEs while avoiding the introduction of erroneous discontinuities in parameters. The following sections and experiments will further illustrate the framework's superior performance and other applications.

4. Ablation Study of Neural Networks

This section evaluates the contribution of each component in the proposed two-stage framework. Starting from standard PINNs, JVC-PINNs framework progressively add the coefficient sub-network, the gradient-adaptive residual weighting strategy, the GMM-BDMC regime extractor, the classification-based refinement mechanism, and the second-stage constrained parameter refinement. In addition, a direct only Stage 2 variant is included to examine whether the statistical information provided by Stage 1 is necessary for stable piecewise-constant reconstruction.

The ablation groups are defined as follows. A0 is standard PINNs, where the unknown coefficient is treated as a global trainable constant. This group serves as the baseline for parameter inversion and illustrates the limitation of standard PINNs when the true coefficient exhibits jump discontinuities. A1 augments A0 with the coefficient sub-network $\hat{\theta}_p(\mathbf{x}, t)$, allowing the model to learn a continuous spatiotemporally varying coefficient field. Comparing A1 with A0 isolates the effect of replacing a global constant parameter with a learnable coefficient function. A2 further introduces the gradient-adaptive residual weighting strategy in the physics loss. Comparing A2 with A1 isolates the contribution of stabilizing coefficient sampling and suppressing oscillations near discontinuity regions. A3 incorporates the GMM-BDMC statistical learner and the CCD-PINNs refinement stage, but removes the classification loss $\mathcal{L}_{\text{cec}}$. The coefficient values are refined using the admissible intervals $\{\mathcal{I}_k\}$ and candidate discontinuity regions $\{\mathcal{X}_l\}$ inferred from Stage 1, while the final piecewise-constant reconstruction is obtained without classification-based sharpening. Comparing A3 with A2 evaluates the contribution of the statistical-learning-guided constrained refinement framework. A4 corresponds to the complete proposed JVC-PINNs framework. In addition to all components in A3, the classification loss is activated to refine the region-to-state assignment and sharpen discontinuity boundaries. Comparing A4 with A3 directly quantifies the contribution of the classification-based refinement mechanism and evaluates whether explicit discontinuity classification improves coefficient reconstruction and solution accuracy. A5 uses only the CCD-PINNs stage without any Stage 1 parameter information. The piecewise-constant estimator is trained directly without Stage 1 initialization, admissible coefficient intervals, or candidate discontinuity regions. This group tests whether the first-stage GWS-PINNs and GMM-BDMC analysis constitute an essential preprocessing step rather than merely an optional initialization strategy.

All ablation groups use the same observation data, initial-boundary data, residual-point budget, optimizer setting, and network architecture in Section 3. The reported metric is the MSE of the predicted solution, denoted by second-stage CCD-PINNs. The numerical results are summarized in Table 7. To

ensure a fair comparison, all ablation groups are evaluated under the same experimental setting. Specifically, the observation data, initial and boundary data, residual-point budget, neural-network architecture, optimizer, learning-rate schedule, and training epochs are kept identical for each PDE case. Therefore, the differences in Table 7 mainly reflect the effect of the removed or added algorithmic component rather than changes in data density or training configuration.

Compared with A0, A1 significantly reduces the solution MSE in all tested cases. This confirms that representing the unknown coefficient by a sub-network is essential for PDEs with jump-varying parameters. Since A0 can only learn a single global constant, it fails to describe the regime-dependent coefficient structure and therefore produces biased solution approximations. By contrast, A1 provides a continuous coefficient surrogate over the spatiotemporal domain, which substantially improves the flexibility of the inverse model. The comparison between A1 and A2 shows the effect of the gradient-adaptive residual weighting strategy. In the Burgers, Navier-Stokes, and Helmholtz cases, A2 clearly improves the solution accuracy, indicating that adaptive weighting helps stabilize training near discontinuity regions and reduces the influence of high-gradient transition samples. In the Wave and Heat cases, the improvement is less pronounced or nearly neutral, suggesting that the benefit of this strategy depends on the strength of discontinuity and the sensitivity of the PDE residual to coefficient jumps. Overall, A2 provides a more reliable Stage 1 sampler for subsequent statistical learning.

A3 further introduces the GMM-BDMC statistical learner and the second-stage constrained refinement, but without the classification loss. Compared with A2, A3 improves the MSE in most cases, especially for the Navier-Stokes and Helmholtz equations. This shows that replacing the smooth coefficient surrogate with a constrained piecewise-constant representation is beneficial for discontinuous coefficient inverse problems. The statistical learner provides admissible coefficient intervals and candidate jump regions, which reduce the search space of the second-stage inverse problem and improve the physical consistency of the recovered coefficient. A4 corresponds to the complete JVC-PINNs framework. It achieves the best or nearly best MSE in all tested cases. The improvement from A3 to A4 demonstrates the contribution of the classification-based refinement mechanism. By activating the classification loss, the model sharpens the region-to-state assignment and improves the localization of discontinuity boundaries. This effect is particularly important when the Stage 1 coefficient surrogate contains smoothed transition zones, because classification refinement converts these soft transitions into a hard piecewise-constant structure.

The A5 results further demonstrate the necessity of Stage 1 sampling and statistical guidance. Although A5 uses the CCD-PINNs formulation, it removes the Stage 1 initialization, admissible coefficient intervals, and candidate discontinuity regions. Its performance is consistently worse than A4 and can even be worse than A1 or A2 in complex cases. This indicates that directly training a piecewise-constant estimator without prior information is unstable, because the optimizer must simultaneously search for coefficient values and discontinuity locations in a large nonconvex space. Therefore, Stage 1 is not merely

Table 7: Ablation study of neural-network components on different PDE cases about MSE and calculation time.

MSE	Case	A0	A1	A2	A3	A4*	A5
Wave	1.2	1.0290e-4	6.2964e-6	9.3052e-6	6.0437e-6	5.1713e-6	1.5737e-3
Heat	2.1	4.9993e-5	6.4613e-6	6.4613e-6	6.7663e-6	6.3578e-6	7.2919e-6
Burgers	3.2	2.0570e-5	5.2924e-9	7.8007e-10	8.3660e-10	7.5590e-10	8.6359e-8
Navier-Stokes	4.8	6.2474e-4	2.8990e-4	5.6403e-5	3.5349e-5	3.0631e-5	2.6029e-4
Helmholtz	5.1	3.3242e-8	2.9684e-9	1.3884e-9	9.3906e-10	7.9232e-10	1.8144e-8
Time/s	Case	A0	A1	A2	A3	A4*	A5
Wave	1.2	2306.6	2373.7	2481.7	2569.8	2605.1	2320.0
Heat	2.1	2560.0	2960.0	3320.0	3382.2	3515.9	2965.8
Burgers	3.2	7347.6	7825.0	8082.1	8184.0	8202.1	7706.2
Navier-Stokes	4.8	3928.9	4100.2	4194.0	4746.9	4826.3	3948.0
Helmholtz	5.1	6910.7	7089.3	7581.1	8447.0	8606.9	7004.2

Table 8: Grid resolution sensitivity study with respect to data and physics residual points.

Equation	Case	Data points	Residual points	MSE	λ_1	λ_2	τ
Burgers	3.2	2000	4000	1.6248e−9	0.4993/1.0006	0.0992	4.9979
Burgers	3.2	4000*	4000*	7.5590e−10	0.4998/0.9998	0.1000	4.9995
Burgers	3.2	10000	4000	4.9824e−10	0.4901/0.9984	0.1000	4.9996
Burgers	3.2	20000	4000	4.7316e−10	0.5233/1.0122	0.1000	4.9997
Burgers	3.2	4000	2000	1.0123e−9	0.4968/1.0032	0.0991	4.9864
Burgers	3.2	4000*	4000*	7.5590e−10	0.4998/0.9998	0.1000	4.9995
Burgers	3.2	4000	10000	7.6881e−10	0.4998/0.9998	0.1000	4.9995
Burgers	3.2	4000	20000	1.1126e−9	0.4996/0.9980	0.1000	4.9994

an initialization step, but an essential preprocessing stage that provides reliable structural information for constrained refinement.

The computational time in Table 7 shows that adding components gradually increases the training cost. A1 is slightly more expensive than A0 due to the coefficient sub-network, A2 introduces additional cost from gradient computation in the adaptive weights, and A3–A4 require extra statistical inference and second-stage refinement. However, the increase in computational cost is moderate compared with the gain in accuracy and interpretability. In particular, A4 only requires a small additional cost over A3, but consistently improves the final reconstruction. This indicates that the classification-based refinement is computationally efficient.

Table 8 further reports the sensitivity of JVC-PINNs to the numbers of observation and residual points using Burgers' equation in Case 3.2. The baseline setting, marked by $\star$, uses 4000 data points and 4000 residual points. When the number of data points is reduced to 2000, the MSE increases and the coefficient estimates become slightly less accurate, indicating that insufficient observations weaken the data constraint. Increasing the number of data points to 10000 or 20000 further reduces the solution MSE, but the improvement in parameter estimation is not monotonic, which suggests that simply adding observation points does not always lead to better coefficient recovery once the data constraint is already sufficient.

A similar phenomenon is observed for residual points. Reducing the residual points to 2000 leads to

a less accurate change-point estimate, while increasing them to 10000 maintains stable parameter and change-point recovery. However, further increasing the number to 20000 does not produce additional improvement and may slightly increase the MSE. This indicates that excessive residual points are not necessarily beneficial, because the optimization balance between data fitting and physics residuals may change. Overall, the selected baseline resolution provides a favorable balance between solution accuracy, coefficient recovery, change-point localization, and computational cost.

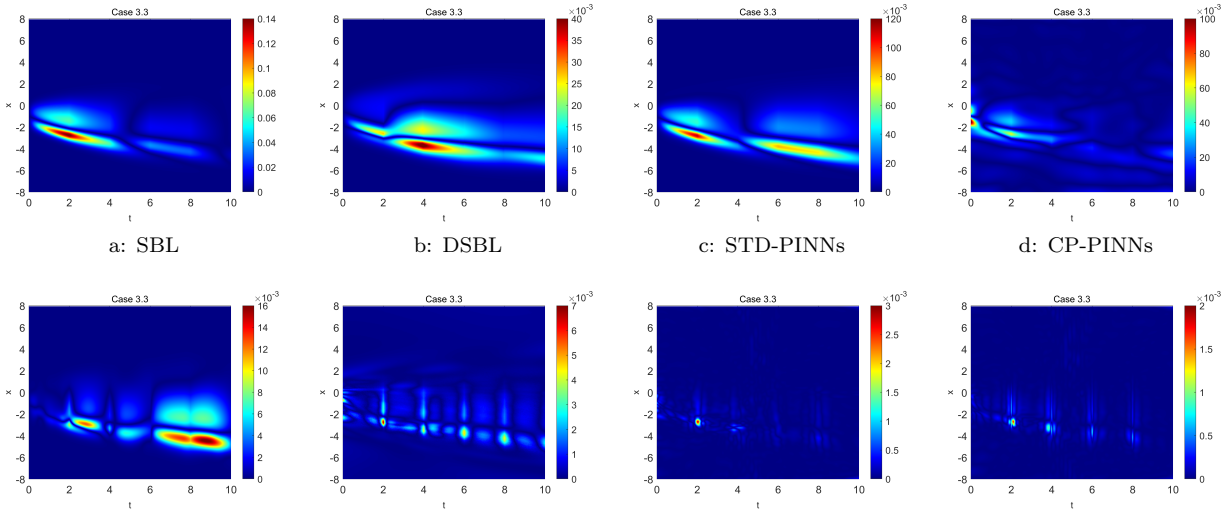
These ablation results confirm the necessity of the main components in JVC-PINNs. The coefficient sub-network improves representational capacity, the gradient-adaptive weighting stabilizes Stage 1 sampling, the GMM-BDMC module provides structural prior information, the second-stage constrained refinement enforces the hard piecewise-constant form, and the classification loss sharpens discontinuity boundaries. Under unified experimental settings, the complete A4 model achieves the most reliable performance across different PDE types.

5. Comparison with Existing Algorithms

This section compares the proposed JVC-PINNs framework with representative existing algorithms from three aspects. First, evaluating different neural-network and Bayesian inverse methods for recovering PDE coefficients from observed solution data, with emphasis on their ability to approximate solutions and sample jump-varying parameters. Second, comparing statistical learning methods for extracting discrete coefficient regimes from the sampled coefficient values, including their performance in state estimation, uncertainty characterization, and candidate jump-region detection. Third, analyzing the computational efficiency of different model-selection strategies, especially the advantage of the proposed GMM-BDMC module over exhaustive AIC/BIC-based selection. These comparisons show that JVC-PINNs combines accurate neural-network sampling, robust statistical regime identification, and efficient constrained refinement, leading to improved performance in inverse problems governed by PDEs with discontinuous coefficients.

5.1. Bayesian and Neural Networks

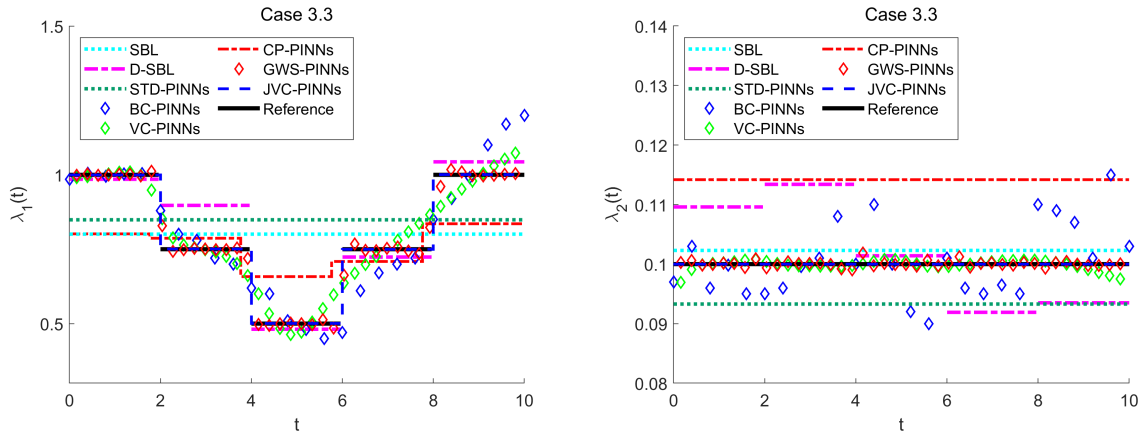
First, this part compare the proposed framework with representative methods for PDE parameter inverse problems, including sparse Bayesian learning (SBL) [41], discrete sparse Bayesian learning (DSBL) [39], standard physics-informed neural networks (STD-PINNs) [25], change-point detection physics-informed neural networks (CP-PINNs) [36], backward compatible physics-informed neural networks (BC-PINNs) [34], variable coefficient physics-informed neural networks (VC-PINNs) [35], the first-stage GWS-PINNs sampler, and the complete JVC-PINNs framework proposed in this work. To ensure a fair baseline comparison, all methods are evaluated using the same observation data generated from the same reference solution. For statistical optimization methods such as SBL and DSBL, the



a: SBL b: DSBL c: STD-PINNs d: CP-PINNs

e: BC-PINNs f: VC-PINNs g: GWS-PINNs h: JVC-PINNs

Figure 12: Comparison of absolute errors between predicted solution and reference solution by different inverse methods for time-varying coefficients of Burgers' equation in Case 3.3.



a: Parameter λ_1 b: Parameter λ_2

Figure 13: Comparison of JVC-PINNs sampling results for time-varying coefficients of Burgers' equation in Case 3.3 with other methods.

amount of available data is kept identical. For physics-informed neural-network methods, the numbers of observation points, initial-boundary points, and physics residual points are fixed across all models, and the network architectures, optimizer settings, learning rates, and training epochs are kept consistent whenever applicable. Therefore, the observed differences mainly reflect the algorithmic design rather than variations in data availability or training configuration.

SBL and STD-PINNs are mainly designed for inverse problems with constant coefficients. When the true coefficient varies over time or space, these methods tend to identify only an averaged effective parameter, which leads to large errors in different coefficient regimes. DSBL improves the classical Bayesian framework by introducing a discrete switching mechanism, but it usually requires prior information about possible switching times or state transitions. Therefore, its applicability is limited when the number and locations of jumps are unknown.

Among PINN-based methods, BC-PINNs and VC-PINNs can approximate time-varying or spatially varying coefficients to some extent. However, their coefficient representations are still continuous or locally smooth, making them less suitable for recovering sharp jumps. BC-PINNs also relies on a prescribed time-domain decomposition. Too few subdomains may lead to inaccurate jump localization, whereas too many subdomains increase the computational burden and may introduce unstable local estimates. CP-PINNs directly introduces change-point variables and is effective for temporal switching problems, but its performance is sensitive to initialization and to prior assumptions on the number of change points. Moreover, in this example, CP-PINNs does not impose effective constraints on the multi-change coefficient values during optimization. As a result, although it can introduce a discontinuous parameter representation, the estimated jump-varying coefficient function is not sufficiently accurate.

Compared with these methods, GWS-PINNs introduces an auxiliary coefficient sub-network to learn a continuous surrogate of the unknown coefficient field and further incorporates a gradient-adaptive residual weighting strategy. This design improves the reliability of coefficient sampling in approximately constant regimes and suppresses the adverse influence of high-gradient transition regions. Therefore, GWS-PINNs is more suitable as a neural-network sampler for PDEs with discontinuously varying coefficients. Then the complete JVC-PINNs framework further improves over GWS-PINNs by converting the smooth coefficient surrogate into an explicit hard piecewise-constant estimator. After first-stage sampling, the GMM-BDMC module infers the number of coefficient states, estimates admissible coefficient intervals, and identifies candidate jump regions. The second-stage CCD-PINNs then refines the coefficient values and discontinuity locations under these constraints. In this way, JVC-PINNs preserves the flexible sampling ability of GWS-PINNs while reducing the bias caused by smooth neural approximation near jumps.

The comparison is conducted on the Burgers' equation in Case 3.3, where $\lambda_1(t)$ is a jump-varying coefficient and $\lambda_2(t)$ is a constant coefficient. The absolute errors of the predicted solution fields are shown in Figure 12, and the corresponding coefficient recovery results are shown in Figure 13. Quantitative

Table 9: Comparison sampling and estimating results for identifying time-varying coefficients in Burgers' equation Case 3.3 with other Bayesian and neural networks methods.

Algorithm	MSE	Parameter	Reference	Predicted	Relative error	Time/s
SBL	2.3418e-4	$\lambda_1(t)$	0.5	0.8007	+60.1447%	2880.7
			0.75	0.8007	+6.7632%	
			1	0.8007	−19.9276%	
		$\lambda_2(t)$	0.1	0.1023	+2.2785%	
DSBL	4.0347e-5	$\lambda_1(t)$	0.5	0.4812	−3.7561%	5726.6
			0.75	0.8105	+8.0635%	
			1	1.0143	+1.4286%	
		$\lambda_2(t)$	0.1	0.1019	+1.9235%	
STD-PINNs	2.6651e-4	$\lambda_1(t)$	0.5	0.8488	+69.7526%	7432.4
			0.75	0.8488	+13.1684%	
			1	0.8488	−15.1237%	
		$\lambda_2(t)$	0.1	0.0933	−6.6713%	
BC-PINNs	5.8597e-6	$\lambda_1(t)$	0.5	0.4770	−4.5963%	8278.5
			0.75	0.6825	−8.9944%	
			1	0.9895	−1.0474%	
		$\lambda_2(t)$	0.1	0.1004	+0.3825%	
VC-PINNs	2.1545e-7	$\lambda_1(t)$	0.5	0.4804	−3.9147%	8012.7
			0.75	0.7378	−1.6251%	
			1	1.0252	+2.5184%	
		$\lambda_2(t)$	0.1	0.0998	−0.2035%	
CP-PINNs	4.7447e-5	$\lambda_1(t)$	0.5	0.6574	+31.4877%	7714.7
			0.75	0.7477	−0.3084%	
			1	0.8184	−18.1609%	
		$\lambda_2(t)$	0.1	0.1142	+14.1632%	
GWS-PINNs	3.6277e-9	$\lambda_1(t)$	0.5	0.4994	−0.1297%	8076.4
			0.75	0.7512	+0.1634%	
			1	1.0010	+0.0962%	
		$\lambda_2(t)$	0.1	0.1000	−0.0150%	
JVC-PINNs*	3.5863e-9	$\lambda_1(t)$	0.5	0.5013	+0.2570%	8197.7
			0.75	0.7498	−0.0313%	
			1	0.9999	−0.0113%	
		$\lambda_2(t)$	0.1	0.1000	−0.0041%	

results are reported in Table 9. The results show that SBL and STD-PINNs produce large errors because they cannot represent the temporal switching of $\lambda_1(t)$. DSBL, BC-PINNs, VC-PINNs, and CP-PINNs reduce the error to different degrees, but their errors remain concentrated near coefficient jump regions. In contrast, GWS-PINNs provides more accurate coefficient samples, and JVC-PINNs achieves the best overall reconstruction by further refining the sampled coefficient into a hard piecewise-constant form with acceptable computational burden.

For the solution field, JVC-PINNs achieves the best approximation accuracy among all compared methods for PDEs with jump-varying parameters. In terms of parameter identification, it accurately recovers the three plateau values of $\lambda_1(t)$ and the constant value of $\lambda_2(t)$, with relative errors close to zero. In addition, except for CP-PINNs, JVC-PINNs is the only method among the compared neural-

network approaches that can directly output explicit estimates of both coefficient values and change points. These results demonstrate that the proposed two-stage framework is effective not only for solution reconstruction, but also for interpretable identification of discontinuous coefficients and their switching locations.

5.2. Statistical Clustering Learning

The second comparison focuses on statistical learning methods for extracting discrete coefficient regimes from the first-stage GWS-PINNs samples. After the neural-network sampler produces the empirical coefficient values, the statistical module is required to identify the coefficient states, estimate their uncertainty, and provide candidate jump regions for the second-stage CCD-PINNs refinement. This part compare several representative clustering estimators, including K-nearest neighbor (KNN) [45], K-means [46], the expectation maximization (EM) [47] for GMMs, the Markov Chain Monte Carlo (MCMC) [40] for GMMs, the generative adversarial networks (GANs) [48] as a deep learning method, and the proposed GMM-BDMC model-selection strategy. For KNN, K-means, and GAN-based clustering, the reported mean and standard deviation are computed as the empirical average and empirical standard deviation of the samples assigned to each estimated cluster. In contrast, the GMM-based methods naturally provide these quantities through the mean and variance parameters of each Gaussian component.

For known-K estimation, Table 10 reports the estimated means, standard deviations, and computational time for different clustering or mixture-learning algorithms. KNN and K-means are computationally efficient, but their accuracy depends strongly on the separability of the sampled coefficient values. When transition samples or sampling noise are present, distance-based classification may merge nearby regimes or enlarge the estimated variance. EM is also efficient, but it is sensitive to initialization and may converge to local optima, especially when the mixture components are unbalanced or the first-stage samples contain biased transition values. GAN-based clustering provides competitive estimates in several cases, but it requires training additional neural networks and therefore introduces higher computational cost. MCMC improves robustness by posterior sampling, but its efficiency decreases when the sampled distribution is complex.

The proposed BDMC-based mixture learner achieves a favorable balance between accuracy, uncertainty estimation, and computational cost. In most cases in Table 10, BDMC gives coefficient means close to the reference values and maintains moderate variance estimates. More importantly, unlike KNN, K-means, EM, and GAN-based clustering with a prescribed number of clusters, BDMC is naturally compatible with unknown-K inference. This property is essential in the proposed JVC-PINNs framework, because the number of coefficient regimes is generally unavailable before solving the inverse problem.

For unknown-K estimation, Table 11 compares AIC/BIC-based GMM selection with BDMC. Both methods correctly identify the number of coefficient states in the tested cases, but they differ significantly

Table 10: Known-K comparison of coefficient-regime estimators.

Case	Algorithm	Reference	Mean	Sigma	Time/s	Algorithm	Reference	Mean	Sigma	Time/s
1.3	KNN	2.5 3	2.7162 2.9948	0.1476 0.0163	4.2	MCMC	2.5 3	2.8007 2.9998	0.1676 0.0041	34.6
	K-means	2.5 3	2.6318 2.9844	0.1163 0.0393	5.3	BDMC*	2.5 3	2.5854 2.9916	0.2495 0.0248	37.2
	EM	2.5 3	2.9051 2.9722	0.1606 0.0789	6.9	GANs	2.5 3	2.6318 2.9844	0.1163 0.0393	60.1
2.2	KNN	0.05 0.1 0.2	0.0517 0.0984 0.1930	0.0048 0.0148 0.0149	3.1	MCMC	0.05 0.1 0.2	0.0509 0.0965 0.1932	0.0053 0.0175 0.0154	24.4
	K-means	0.05 0.1 0.2	0.0531 0.1002 0.1926	0.0070 0.0130 0.0155	3.9	BDMC*	0.05 0.1 0.2	0.0527 0.1002 0.1935	0.0065 0.0141 0.0142	26.2
	EM	0.05 0.1 0.2	0.0702 0.0831 0.1666	0.0267 0.0358 0.0465	5.9	GANs	0.05 0.1 0.2	0.0531 0.1002 0.1926	0.0070 0.0130 0.0155	43.3
3.4	KNN	0.5 0.75 1	0.5087 0.7560 0.9970	0.0225 0.0397 0.0318	2.3	MCMC	0.5 0.75 1	0.5098 0.7559 0.9971	0.0444 0.0458 0.0409	18.6
	K-means	0.5 0.75 1	0.5111 0.7561 0.9958	0.0278 0.0360 0.0338	3.8	BDMC*	0.5 0.75 1	0.5111 0.7561 0.9958	0.0277 0.0360 0.0338	20.2
	EM	0.5 0.75 1	0.6247 0.8011 0.9385	0.1398 0.1555 0.1125	5.2	GANs	0.5 0.75 1	0.5111 0.7561 0.9958	0.0278 0.0360 0.0338	40.6
3.4	KNN	1 1.3333 2	0.9961 1.3339 1.9761	0.0398 0.0660 0.0592	2.3	MCMC	1 1.3333 2	0.9954 1.3283 1.9648	0.0623 0.0753 0.1057	18.6
	K-means	1 1.3333 2	0.9961 1.3307 1.9699	0.0398 0.0577 0.0735	3.8	BDMC*	1 1.3333 2	0.9946 1.3321 1.9761	0.0368 0.0679 0.0592	20.2
	EM	1 1.3333 2	1.1287 1.2291 1.8287	0.1871 0.2498 0.2874	5.2	GANs	1 1.3333 2	0.9961 1.3307 1.9699	0.0398 0.0577 0.0735	40.6
4.4	KNN	0.01 0.04	0.0122 0.0384	0.0044 0.0046	2.0	MCMC	0.01 0.04	0.0116 0.0378	0.0042 0.0058	16.6
	K-means	0.01 0.04	0.0120 0.0382	0.0041 0.0049	2.9	BDMC*	0.01 0.04	0.0122 0.0384	0.0044 0.0046	17.6
	EM	0.01 0.04	0.0145 0.0349	0.0087 0.0099	4.7	GANs	0.01 0.04	0.0120 0.0382	0.0041 0.0049	35.7
5.1	KNN	13.3333 20	13.9595 19.8903	0.9486 0.3681	7.1	MCMC	13.3333 20	17.8638 19.9898	2.5606 0.0210	76.8
	K-means	13.3333 20	14.0549 19.8971	1.0651 0.3387	8.4	BDMC*	13.3333 20	13.4176 19.8082	0.0843 0.1918	84.2
	EM	13.3333 20	19.3572 19.7141	1.7473 1.0963	9.4	GANs	13.3333 20	14.0549 19.8971	1.0651 0.3387	145.4

Table 11: Unknown-K comparison of AIC/BIC-based GMM estimators with BDMC.

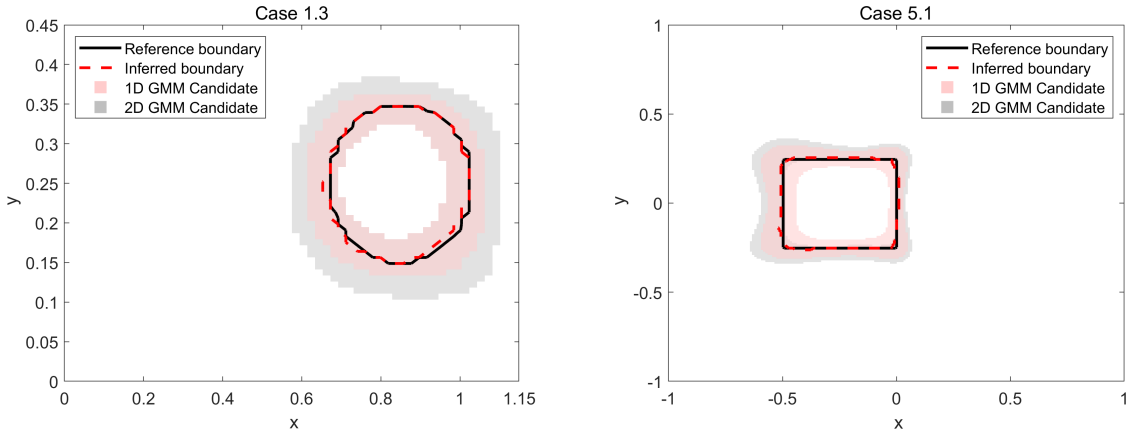
Case	GMM method	$\hat{K}$	Reference	Mean	Sigma	Time/s	GMM method	$\hat{K}$	True	Mean	Sigma	Time/s
1.3	1D AIC/BIC	2	2.5 3	2.9217 2.9586	0.1482 0.1035	148.6	1D BDMC*	2	2.5 3	2.5854 2.9916	0.2495 0.0248	37.2
	2D AIC/BIC	2	2.5 3	2.5915 2.9780	0.2594 0.1811	301.3	2D BDMC	2	2.5 3	2.5854 2.9916	0.4367 0.0433	76.8
2.2	1D AIC/BIC	3	0.05 0.1 0.2	0.0700 0.0845 0.1628	0.0269 0.0375 0.0488	132.9	1D BDMC*	3	0.05 0.1 0.2	0.0527 0.1002 0.1935	0.0065 0.0141 0.0142	26.2
3.4	1D AIC/BIC	3	0.5 0.75 1	0.6265 0.7987 0.9359	0.1410 0.1567 0.1144	101.9	1D BDMC*	3	0.5 0.75 1	0.5111 0.7561 0.9958	0.0277 0.0360 0.0338	20.2
3.4	1D AIC/BIC	3	1 1.3333 2	1.1235 1.2465 1.8034	0.1856 0.2650 0.3058	101.9	1D BDMC*	3	1 1.3333 2	0.9946 1.3321 1.9761	0.0368 0.0679 0.0592	20.2
4.4	1D AIC/BIC	2	0.01 0.04	0.0147 0.0352	0.0089 0.0097	70.1	1D BDMC*	2	0.01 0.04	0.0122 0.0384	0.0044 0.0046	17.6
5.1	1D AIC/BIC	2	13.3333 20	19.5033 19.5572	1.5254 1.4305	347.5	1D BDMC*	2	13.3333 20	13.4176 19.8082	0.0843 0.1918	84.2
	2D AIC/BIC	2	13.3333 20	14.4090 19.9165	2.6695 2.5034	657.9	2D BDMC	2	13.3333 20	13.4176 19.8082	0.1475 0.3357	170.8

in estimation stability and computational cost. AIC/BIC requires fitting multiple independent GMMs with different component numbers and then selecting the optimal model according to the information criterion. In contrast, BDMC treats the number of components as a random variable and explores different models through birth and death moves. The main complexity difference can be summarized as

$$\begin{aligned} N^{1D}_{\mathrm{AIC/BIC}} &= \sum_{k=1}^{K}(3k-1) = \mathcal{O}(K^2), \\ N^{1D}_{\mathrm{BDMC}} &= 4K = \mathcal{O}(K), \\ N^{dD}_{\mathrm{AIC/BIC}} &= \sum_{k=1}^{K}\left(k\left(\frac{d(d+1)}{2}+d+1\right)-1\right) = \mathcal{O}(d^2K^2), \\ N^{dD}_{\mathrm{BDMC}} &= K\left(\frac{d(d+1)}{2}+d+2\right) = \mathcal{O}(d^2K). \end{aligned} \tag{5.1}$$

Here, the terms include the component means, variances or covariance matrices, mixture weights, and the additional birth-death rates in BDMC. Therefore, the use of BDMC reduces the model-selection complexity from quadratic to linear with respect to the maximum number of candidate regimes.

The numerical results in Table 11 are consistent with this analysis. For the one-dimensional GMM setting, 1D BDMC achieves much shorter computational time than 1D AIC/BIC in all tested cases. For example, in Case 5.1, the 1D AIC/BIC procedure requires repeated model fitting and takes substantially longer, whereas 1D BDMC identifies $\widehat{K} = 2$ with accurate coefficient estimates and much lower cost. Similar improvements are observed in Cases 2.2, 3.4, and 4.4. These results indicate that BDMC is more suitable for the statistical connection between the first-stage sampler and the second-stage constrained estimator.



a: 1D/2D GMM result

b: 1D/2D GMM result

Figure 14: Comparison of 1D and 2D GMM-BDMC inference results for 2D space-varying coefficients of wave equation Case 1.3 and Helmholtz equation Case 5.1.

Since the GMM-BDMC learner depends only on the empirical distribution of the sampled coefficient values, different bijective flattening strategies lead to identical statistical targets up to permutation of sample indices. Consequently, flattening serves only as a computational representation and does not affect the subsequent recovery of discontinuity regions in the original spatiotemporal domain. For the multi-dimensional discontinuous coefficient problems considered in Case 1.3 and Case 5.1, the numerical testing experiments further have been verified that row-major flattening, column-major flattening, and random flattening produce identical estimates of the number of coefficient states $\widehat{K}$, the admissible coefficient intervals $\mathcal{I}_k$, and the candidate discontinuity regions $\mathcal{X}_l$ obtained by the GMM-BDMC module. Therefore, the statistical information passed to the second-stage CCD-PINNs remains unchanged under different flattening strategies, indicating that the proposed framework is insensitive to the ordering of sampled coefficients.

For multi-dimensional spatial coefficients, two implementation strategies are considered. The first strategy flattens the sampled coefficient field into a one-dimensional sequence and then applies 1D GMM-BDMC. The second strategy directly applies a 2D GMM-BDMC to the spatial samples without flattening. Figure 14 compares these two strategies for Case 1.3 and Case 5.1. The results show that direct 2D GMM inference is feasible and can avoid the flattening operation. However, its estimates are generally less stable than those of the flattened 1D GMM-BDMC. Although the estimated means are close to the reference coefficient values, the estimated variances become larger. For the 2D GMM, each component contains a covariance matrix, and the reported standard deviations are obtained from the leading diagonal entries of this covariance matrix.

This increase in variance affects the construction of candidate jump regions. Since the candidate regions $\{\mathcal{X}_l\}_{l=1}^{\widehat{L}}$ are determined from the uncertainty intervals of the inferred mixture components, larger

variance estimates usually lead to wider visualized jump candidates. This phenomenon can be observed in the $\{\mathcal{X}_l\}_{l=1}^{\widehat{L}}$ estimates for Case 1.3 and Case 5.1 in Figure 14. Nevertheless, this does not necessarily degrade the final JVC-PINNs result. The statistical learner is only required to provide candidate regions that contain the true discontinuity interfaces. Then the second-stage CCD-PINNs can further refine the discontinuity location and recover an accurate hard piecewise-constant coefficient function if the true jump boundary is included in the candidate set. However, this still increases the risk of model estimation mistakes in constrained parameter learning of CCD-PINNs.

Overall, the comparison demonstrates that GMM-BDMC is more appropriate than conventional clustering or AIC/BIC-based selection for the proposed framework. It identifies the number of coefficient regimes automatically, provides uncertainty intervals for coefficient values, localizes candidate jump regions, and reduces the computational burden of model selection. The flattened 1D GMM-BDMC is therefore adopted as the default statistical learner in JVC-PINNs, while direct 2D GMM-BDMC can be used as an alternative when preserving spatial sample geometry is preferred.

6. Physical Field Reconstruction

Based on the two-stage JVC-PINNs framework established in Section 2 and the numerical results reported in Section 3, this section demonstrates the practical applicability of the proposed method to high-resolution reconstruction of PDE solution fields. The reconstruction is performed using the refined main-network $\tilde{u}(\mathbf{x}, t)$ obtained from the second-stage CCD-PINNs. The refined network $\tilde{u}(\mathbf{x}, t)$ can generate high-resolution solution images from sparse or discrete observations by evaluating the trained neural surrogate on a dense spatiotemporal grid. Compared with the first-stage GWS-PINNs output $\hat{u}(\mathbf{x}, t)$, the second-stage solution network is trained together with an explicitly constrained piecewise-constant coefficient representation. Therefore, it incorporates not only the physical information learned from the PDE residual and observation data, but also the refined discontinuous coefficient structure obtained through statistical mixture modeling and constrained parameter refinement.

Unlike conventional interpolation of discrete solution data, the reconstruction produced by $\tilde{u}(\mathbf{x}, t)$ is physics-informed. The dense-grid solution values are generated by the trained neural surrogate rather than by a prescribed interpolation stencil. Consequently, the reconstructed physical field is consistent with the governing PDE, the initial and boundary conditions, and the inferred discontinuous coefficient field. The selected examples are the wave equation in Case 1.3 with a spatially varying coefficient and the Navier-Stokes equations in Cases 4.1-4.8 with time-varying coefficients. The quantitative descriptions corresponding to the two figures are in Table 1-4.

For Case 1.3, corresponding to a 2+1D wave equation, Figure 15 shows the reconstructed solution fields over the time interval $[0, 0.2]$ and training data uses only three time slices $t = 0$, $t = 0.015$, and $t = 0.15$. In this example, the lower boundary is set as a restricted boundary, while the other boundaries

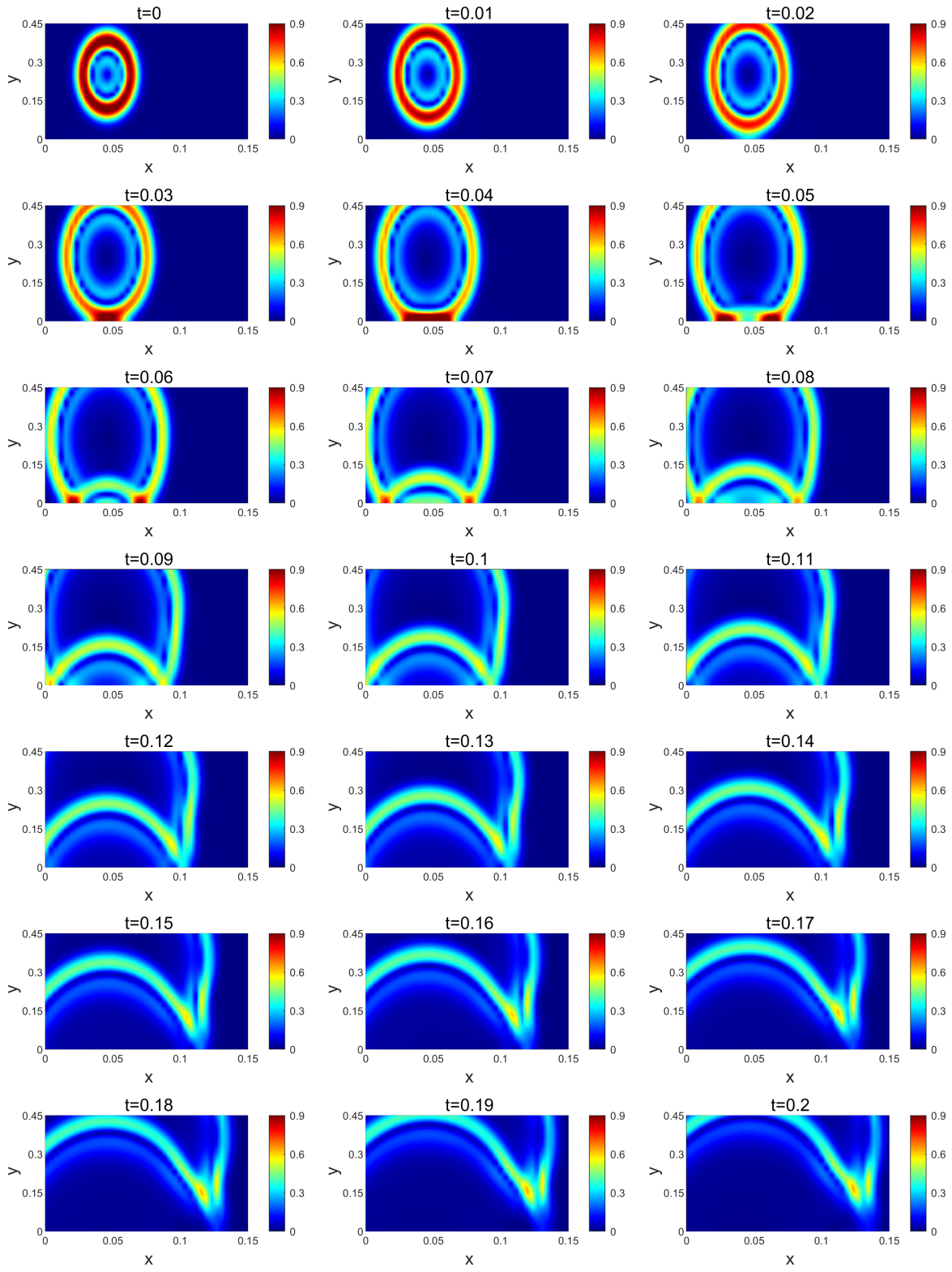


Figure 15: Physical field reconstruction for the wave equation Case 1.3 with discontinuously space-varying coefficients $\alpha(x, y)$.

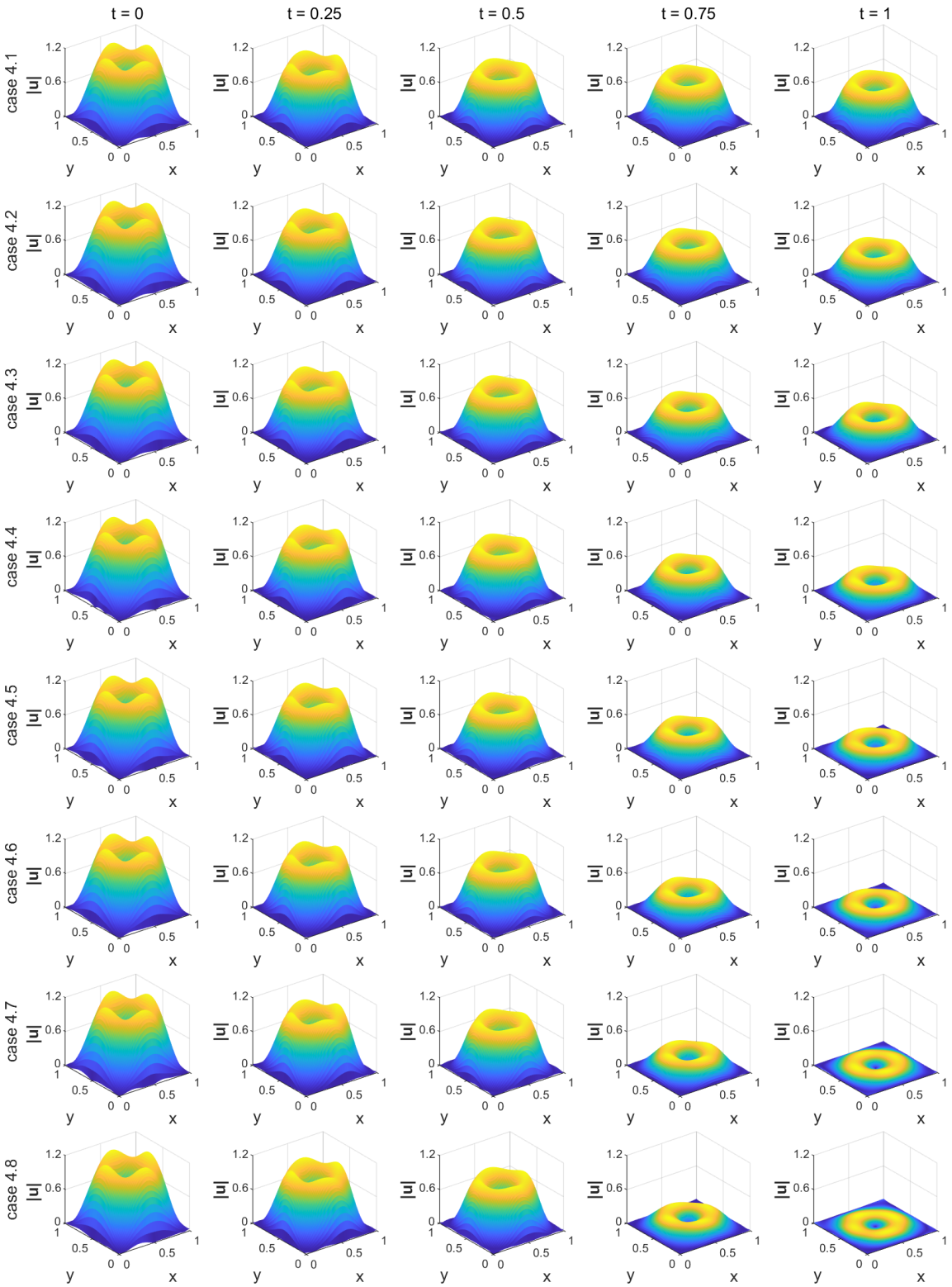


Figure 16: Physical field reconstruction for Navier-Stokes equation Case 4.1-4.8 with discontinuously time-varying coefficients $\nu(t)$.

are free. At the initial time, a solitary wave is generated inside the domain. As time evolves, the wave propagates through the heterogeneous medium, crosses the free boundaries, and rebounds at the restricted boundary. Since the reconstruction is based on the second-stage network $\tilde{u}(\mathbf{x}, t)$, the solution field is obtained under the refined discontinuous coefficient estimator $\tilde{\theta}_p(\mathbf{x}, t)$, which improves the physical consistency of the reconstructed high-resolution images.

For Cases 4.1-4.8, corresponding to the 2+1D Navier-Stokes equations, Figure 16 presents the reconstructed solution fields over the time interval $[0, 1]$. As expected from the experimental setup, the reconstructed fields from Case 4.1 to Case 4.8 are almost identical before $t = 0.5$. After $t = 0.5$, however, these solutions exhibit clearly different dynamics. In particular, Case 4.8 shows a much stronger variation process than Case 4.1, because the coefficient in Case 4.8 undergoes a large temporal jump while the coefficient in Case 4.1 remains unchanged. This comparison shows that the proposed framework can capture the influence of discontinuous parameter changes on the evolution of complex spatiotemporal physical fields.

This reconstruction capability is potentially useful in fluid mechanics, aerodynamics, and other engineering applications where high-resolution experimental data are expensive or difficult to obtain. For instance, data collected from wind tunnel experiments are often sparse due to measurement cost and sensor limitations. If the discontinuous parameter structure of the governing PDE can be inferred from limited observations, the refined neural surrogate $\tilde{u}(\mathbf{x}, t)$ can be used to efficiently reconstruct the physical field and simulate the system response under different initial and boundary conditions.

7. Robustness with Observation Noise

This section investigates the robustness of JVC-PINNs under noisy observations. Compared with the noise-free setting, different levels of relative additive Gaussian noise are imposed on the observed solution data to evaluate the degradation process of the proposed framework. The tested noise variances are from 0.01 to 0.25, which allows us to observe not only the stable regime of the algorithm but also its failure behavior under severe noise contamination.

The robustness of JVC-PINNs comes from the combination of physics-informed learning, Bayesian statistical inference, and constrained refinement. In the first stage, GWS-PINNs suppresses observational noise by enforcing the governing PDE, boundary conditions, and initial conditions, so that the learned solution and coefficient surrogate are not determined solely by noisy data. The gradient-adaptive residual weighting further reduces the influence of unstable high-gradient regions near discontinuities, where noise and jump-induced non-smoothness are most easily mixed. In the statistical stage, GMM-BDMC converts noisy coefficient samples into regime-wise posterior summaries and provides uncertainty intervals for coefficient values and candidate jump regions. In the second stage, CCD-PINNs refines the coefficient

values and change points only within the inferred admissible intervals and transition regions, which reduces the search space and improves stability.

Three time-dependent coefficient cases from Section 3 are selected for the noise robustness test. The results are reported in Table 12. When the noise variance is small or moderate, especially below 0.04, JVC-PINNs maintains accurate solution approximation, coefficient estimation, and change-point localization. The MSE of the predicted solution increases gradually with the noise level, while the relative errors of the recovered coefficients and change points remain within an acceptable range. This indicates that the physics constraints and statistical regularization effectively prevent overfitting to noisy observations.

As the noise variance further increases to 0.16 and 0.25, the degradation becomes more evident. The coefficient estimates become more biased, and the change-point errors increase significantly. This reflects the failure mechanism of the framework under severe noise: the first-stage coefficient samples are strongly distorted, causing the GMM-BDMC intervals and candidate jump regions to deviate from the true regimes. Consequently, the second-stage constrained refinement is initialized from less reliable statistical information. Nevertheless, the gradual deterioration shown in Table 12 indicates that the framework fails in a traceable manner rather than through abrupt numerical instability.

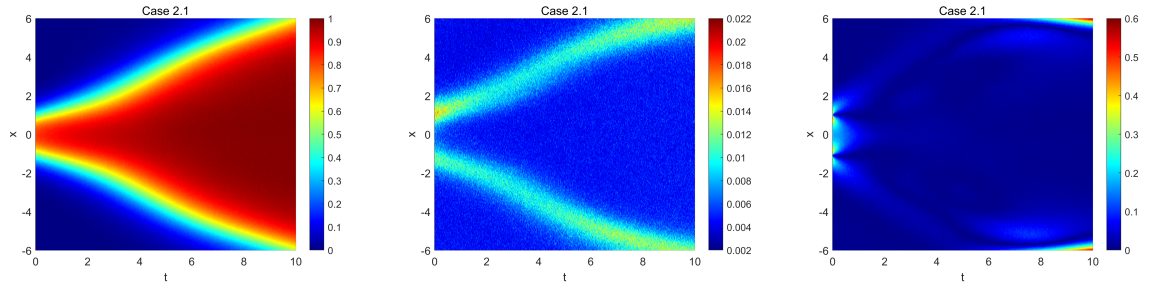
In addition to point estimates, the framework naturally provides uncertainty information for discontinuous coefficients through the statistical learning stage. The posterior statistical inference results obtained by GMM-BDMC define uncertainty intervals for coefficient levels as $\{\mathcal{I}_k\}_{k=1}^{\widehat{K}}$, while the candidate regions $\{\mathcal{X}_l\}_{l=1}^{\widehat{L}}$ describe uncertainty in possible jump locations. Therefore, the parameter estimates and change-point estimates are accompanied by explicit uncertainty information before entering the final constrained refinement stage.

To further quantify the uncertainty of the reconstructed solution field with observation noise, this part introduce a lightweight uncertainty quantification mechanism inspired by Bayesian PINNs [49], where neural-network parameters are treated as random variables and Bayesian inference is used to obtain posterior statistics of the PDE solution. The Monte Carlo dropout is adding to Jvc-PINNs framework as an efficient Bayesian approximation. The dropout technology is introduced only into the hidden-layer activations of the Stage 2 main-network, namely the solution network, while the coefficient refinement and GMM-BDMC settings remain unchanged. This design is particularly suitable for the proposed two-stage framework. The Stage 2 solution network is initialized from the trained first-stage main-network and mainly performs local refinement, hence its weights of networks are already relatively stable. Introducing dropout at this stage mildly perturbs the trained solution surrogate and allows the predictive uncertainty of the solution field to be estimated without retraining a full Bayesian neural network.

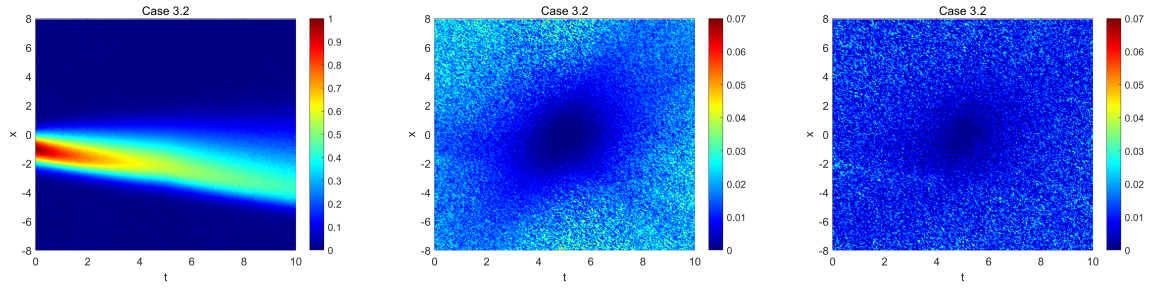
In this uncertainty quantification experiment, all observed data are contaminated by 4% relative additive Gaussian noise, where the noise scale is normalized by the standard deviation of the clean observations. The dropout probability is set to $p = 0.05$, and 100 stochastic forward passes are performed

Table 12: Testing the impact of relative Gaussian observation noise on JVC-PINNs framework.

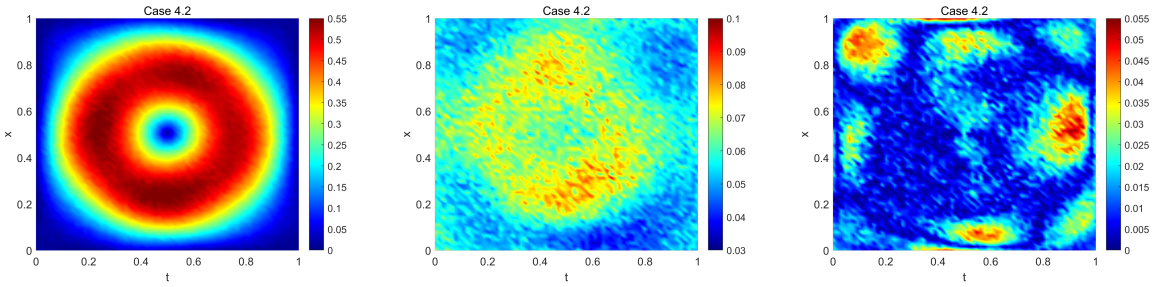
Case	Noise variance	MSE of solution	Parameter	Coefficient True	Coefficient Predicted	Relative error	Change point True	Change point Predicted	Relative error
2.1	0	6.3578e-06	$c(t)$	0.1 0.2	0.0980 0.1981	−2.0034% −0.9534%	5	4.9846	−0.3074%
	0.01	7.3178e-06	$c(t)$	0.1 0.2	0.0954 0.1901	−4.6441% −4.9322%	5	4.9152	−1.6967%
	0.04	1.2118e-05	$c(t)$	0.1 0.2	0.0930 0.1852	−7.0342% −7.4204%	5	4.8095	−3.8102%
	0.09	2.6518e-05	$c(t)$	0.1 0.2	0.0907 0.1806	−9.2647% −9.7205%	5	4.5923	−8.1541%
	0.16	6.0118e-05	$c(t)$	0.1 0.2	0.0774 0.1524	−22.6142% −23.7829%	5	3.9380	−21.2409%
	0.25	1.2636e-04	$c(t)$	0.1 0.2	0.0604 0.1163	−39.6312% −41.8608%	5	6.6709	+33.4175%
3.2	0	7.5590e-10	$\lambda_1(t)$	0.5 1	0.4998 0.9998	−0.0387% −0.0152%	5	4.9995	−0.0093%
			$\lambda_2(t)$	0.1	0.1000	−0.0183%			
	0.01	1.2208e-06	$\lambda_1(t)$	0.5 1	0.4906 0.9584	−1.8731% −4.1602%	5	5.0114	+0.2271%
			$\lambda_2(t)$	0.1	0.0951	−4.9228%			
	0.04	6.3208e-06	$\lambda_1(t)$	0.5 1	0.4727 0.9258	−5.4619% −7.4153%	5	4.9443	−1.1142%
			$\lambda_2(t)$	0.1	0.0926	−7.4098%			
	0.09	1.9621e-05	$\lambda_1(t)$	0.5 1	0.4624 0.9028	−7.5218% −9.7157%	5	5.1559	+3.1172%
			$\lambda_2(t)$	0.1	0.0903	−9.7104%			
	0.16	4.8321e-05	$\lambda_1(t)$	0.5 1	0.4267 0.8321	−14.6534% −16.7872%	5	4.4893	−10.2144%
			$\lambda_2(t)$	0.1	0.0762	−23.7578%			
	0.25	1.0250e-04	$\lambda_1(t)$	0.5 1	0.3226 0.6152	−35.4733% −38.4778%	5	6.4227	+28.4544%
			$\lambda_2(t)$	0.1	0.0536	−46.4055%			
4.2	0	2.1226e-05	$\nu(t)$	0.01 0.02	0.0101 0.0198	+1.4376% −0.7740%	0.5	0.4998	−0.0489%
	0.01	2.3966e-05	$\nu(t)$	0.01 0.02	0.0096 0.0190	−4.2495% −4.9231%	0.5	0.4988	−0.2304%
	0.04	3.5066e-05	$\nu(t)$	0.01 0.02	0.0093 0.0185	−7.1653% −7.4102%	0.5	0.4947	−1.0563%
	0.09	6.3166e-05	$\nu(t)$	0.01 0.02	0.0091 0.0181	−9.4374% −9.7108%	0.5	0.5411	+8.2204%
	0.16	1.2267e-04	$\nu(t)$	0.01 0.02	0.0077 0.0152	−23.0368% −23.7596%	0.5	0.6070	+21.3957%
	0.25	2.3373e-04	$\nu(t)$	0.01 0.02	0.0059 0.0116	−41.4715% −42.1305%	0.5	0.3575	−28.4959%



a: Mean field estimation b: Variance field estimation c: Mean field absolute error



d: Mean field estimation e: Variance field estimation f: Mean field absolute error



g: Mean field estimation h: Variance field estimation i: Mean field absolute error

Figure 17: Uncertainty quantification under 4% relative Gaussian observation noise using Monte Carlo dropout in main-network of second-stage CCD-PINNs.

during testing. The predictive mean field, predictive variance field, and absolute error between the predictive mean and the reference solution are then computed from these stochastic predictions. Except for settings of uncertainty quantification part, others including observation noise, dropout, and Monte Carlo sampling, all network architectures, training points, optimizers, learning rates, stage divisions, GMM-BDMC detection procedures, and parameter initializations are kept the same as in the previous numerical experiments.

Under noisy observations, relying only on a single deterministic output of the main-network may be unreliable, because local perturbations in the data can be amplified during the inverse reconstruction process. Providing both the predictive mean field and the predictive variance field reduces the risk of misinterpreting an uncertain reconstruction as a reliable physical field. The uncertainty visualizations in Figure 17 show that the predictive variance is spatially nonuniform and tends to increase in regions where

the solution has stronger local variation or where the inverse reconstruction is more sensitive to noisy observations. Meanwhile, the predictive mean remains close to the reference solution in most regions, and the absolute error is broadly consistent with the high-variance areas. These results indicate that JVC-PINNs can provide not only accurate point estimates for discontinuous coefficients and solution fields, but also uncertainty quantification under noisy observations by Monte Carlo dropout technology. The variance field also provides practical guidance for subsequent data acquisition and numerical refinement. In regions with large predictive variance, one may deploy sensors with stronger noise resistance, collect additional observation points, or increase the sampling density of physics residual points during training. Therefore, the proposed uncertainty quantification mechanism can be used not only as a diagnostic tool for assessing reconstruction reliability, but also as an adaptive indicator for improving experimental design and computational accuracy.

8. Limitations

The proposed JVC-PINNs framework is developed mainly for PDE inverse problems with finite piecewise-constant coefficients. This design is most explicit in the CCD-PINNs stage, where the unknown coefficient is replaced by a hard piecewise-constant representation. For constant coefficients, the JVC-PINNs framework does not incorrectly identify regions of change, such as wave equation Case 1.1 and Navier-Stokes equation Case 4.1. For smoothly varying coefficients, or coefficients that are only approximately piecewise constant, the GWS-PINNs stage may already provide a satisfactory continuous approximation of the parameter function, such as Burgers' equation Case 4.5 and Case 4.6. In these cases, imposing a hard discontinuous structure in the second stage may not always be necessary, and may even introduce additional approximation bias.

A complete theoretical analysis of the proposed framework is still missing. The present work does not provide results on identifiability, convergence, or error bounds as theorems. Existing theory for PINNs has already established many approximation, optimization, and generalization results for smooth PDE settings. The problems considered here have an additional difficulty, the PDE coefficient field is discontinuous, and derivatives of the PDE solution not exist across jump boundaries. However, the PDE solution is still continuous over the whole domain in the examples studied in this work. This structure suggests that parts of the existing PINNs theory may be extendable to the current setting by treating the discontinuity interfaces separately or by using piecewise regularity arguments. Establishing identifiability conditions, convergence guarantees, and quantitative error estimates for JVC-PINNs remains an important topic for future research.

The accuracy of CCD-PINNs relies heavily on the coefficient samples produced by GWS-PINNs. The statistical mixture learner estimates parameter regimes, admissible intervals, and candidate jump regions from the first-stage sub-network outputs. Poor Stage 1 sampling may therefore propagate directly into

the second-stage refinement. Large observational noise, sparse data, or unstable optimization can blur the sampled coefficient levels and distort transition regions, leading to incorrect GMM-BDMC inference and unreliable constrained estimation.

The numerical studies in this work are based on synthetic data generated from prescribed PDE models. Such settings make it possible to evaluate coefficient values and jump locations in a controlled manner. Real measured heterogeneous physical fields may contain sensor bias, correlated noise, missing observations, unmodeled forcing terms, or more complicated material structures. The performance of the proposed framework on experimental or field data remains to be examined.

The present experiments use regular computational domains and standard initial-boundary configurations. Parameter jumps are assumed to occur inside the spatiotemporal domain, away from the initial slice and spatial boundary. Irregular geometries, complex boundary conditions, moving interfaces, and coefficient variations intersecting the initial or boundary surfaces are not considered in the current implementation.

The governing PDE, source term, and initial-boundary data are assumed to be known and correctly specified. This is a strong model prior. When the PDE form is unknown, one may need symbolic learning or PDE discovery techniques to identify the governing equation before applying the proposed framework. Model mismatch, incorrect boundary conditions, and inaccurate initial data are also not included in the present study. Since the physics-informed loss is built directly on the prescribed PDE prior, JVC-PINNs can be sensitive to errors in the assumed model. Improving robustness under imperfect physical priors is an important direction for future work.

These limitations also indicate several directions for future work. Further studies on noisy real-world measurements, irregular domains, boundary-involved jumps, unknown governing equations, and model mismatch would substantially broaden the applicability of the proposed framework. Since this work mainly focuses on methodological development, the present study serves as a first introduction of the JVC-PINNs framework and validates its feasibility through numerical experiments on representative PDE models. More extensive theoretical analysis and application-oriented investigations will be pursued in future research.

9. Conclusion and Discussion

This study developed a two-stage physics-informed learning framework, termed JVC-PINNs, for inverse problems governed by PDEs with discontinuously varying coefficients. The proposed method addresses the central difficulty of recovering jump-discontinuous parameter fields from limited and possibly noisy observations, where the coefficient values, the number of regimes, and the transition locations are all unknown. In the first stage, a dual-network GWS-PINNs architecture is constructed, in which the

main-network approximates the PDE solution and the auxiliary coefficient network provides a relaxed continuous soft approximation of the true discontinuous coefficient field. A gradient-adaptive weighting strategy is incorporated into the physics residual to improve training stability and enhance the reliability of coefficient sampling near potential jump regions. The sampled coefficient values are further analyzed by Bayesian statistical mixture modeling combined with birth-death Markov dynamics model selection, which adaptively identifies the number of coefficient states and provides candidate intervals for both parameter values and transition regions. In the second stage, the inverse problem is reformulated as a constrained CCD-PINNs estimator, where the smooth coefficient surrogate is replaced by a form-consistent hard piecewise-constant approximation. The coefficient values and discontinuity locations are then refined within the admissible intervals and candidate regions inferred from the statistical learning stage, thereby reducing the search space. Comprehensive numerical experiments on different PDE systems with jump-discontinuous coefficients demonstrate that the proposed framework can accurately identify parameter regimes, locate transition regions, and reconstruct the corresponding solution fields, showing improved adaptability and accuracy compared with existing methods, especially in the presence of abrupt temporal or spatial transitions and observational noise. These results indicate that JVC-PINNs provides a flexible and generalizable computational approach for inverse problems involving discontinuous parameter structures in non-stationary and heterogeneous spatiotemporal systems.

The study of inverse problems for non-stationary and heterogeneous spatiotemporal systems still presents many directions for future work. A deeper theoretical understanding of the proposed framework, including convergence, identifiability, error propagation, and uncertainty quantification, is needed to further support its reliability. Improving computational efficiency and scalability is also important for high-dimensional PDEs, multi-parameter systems, and large-scale datasets, where adaptive sampling, parallel computing, reduced-order modeling, or dimensionality reduction may be useful. Future studies should further test the framework on real measured heterogeneous physical fields, irregular domains, complex boundary conditions, unknown governing equations, and cases with model mismatch or boundary-involved parameter jumps. These extensions may require combining JVC-PINNs with PDE discovery, symbolic learning, robust optimization, or uncertainty-aware inference. Broader applications in aerospace, transportation, geophysics, biological systems, materials, and smart manufacturing are also worth exploring, especially for online parameter estimation and real-time decision-making. Since this work mainly focuses on the first methodological introduction of JVC-PINNs and its validation on representative synthetic PDE examples, addressing these issues would greatly expand the application scope and practical impact of the proposed framework.

Acknowledgements

This work was supported by supported by "the Fundamental Research Funds for the Central Universities".

References

[1] V. Isakov, On uniqueness of recovery of a discontinuous conductivity coefficient, Communications on Pure and Applied Mathematics 41 (7) (1988) 865–877.

[2] G. Uhlmann, Inverse problems: Seeing the unseen, Bulletin of Mathematical Sciences 4 (2014) 209–279.

[3] T. F. Chan, X.-C. Tai, Identification of discontinuous coefficients in elliptic problems using total variation regularization, SIAM Journal on Scientific Computing 25 (3) (2003) 881–904.

[4] T. F. Chan, X.-C. Tai, Level set and total variation regularization for elliptic inverse problems with discontinuous coefficients, Journal of Computational Physics 193 (1) (2004) 40–66.

[5] D. N. Hào, T. N. T. Quyen, Convergence rates for total variation regularization of coefficient identification problems in elliptic equations I, Inverse Problems 27 (7) (2011) 075008.

[6] Y. A. Erlangga, C. Vuik, C. W. Oosterlee, On a class of preconditioners for solving the Helmholtz equation, Applied Numerical Mathematics 50 (3-4) (2004) 409–425.

[7] B. S. Guru, H. R. Hiziroglu, Electromagnetic field theory fundamentals, Cambridge University Press, Cambridge, UK, 2009.

[8] J. Metcalfe, D. Tataru, Global parametrices and dispersive estimates for variable coefficient wave equations, Mathematische Annalen 353 (4) (2012) 1183–1237.

[9] Z. Ning, C. Shen, X. Zhao, H. Li, C. Lin, Y. Zhang, Nonlinear boundary stabilization of the wave equations with variable coefficients and time dependent delay, Applied Mathematics and Computation 232 (2014) 511–520.

[10] P. Tong, D. Yang, Q. Liu, X. Yang, J. Harris, Acoustic wave-equation-based earthquake location, Geophysical Journal International 205 (1) (2016) 464–478.

[11] J. F. Hammond, D. M. Bortz, Analytical solutions to Fisher equation with time-variable coefficients, Applied Mathematics and Computation 218 (6) (2011) 2497–2508.

[12] O. Costin, H. Park, Y. Takei, Borel summability of the heat equation with variable coefficients, Journal of Differential Equations 252 (4) (2012) 3076–3092.

[13] Z. Bednarova, J. Kuta, L. Kohut, J. Machat, J. Klanova, I. Holoubek, J. Jarkovsky, L. Dusek, K. Hilscherova, Spatial patterns and temporal changes of heavy metal distributions in river sediments in a region with multiple pollution sources, Journal of Soils and Sediments 13 (2013) 1257–1269.

[14] S. H. Bader, Z. Yin, P. A. Durbin, A hybrid model for turbulence and transition, with a locally varying coefficient, Flow, Turbulence and Combustion 108 (4) (2022) 935–954.

[15] C. Ferguson, A. Bowman, E. Scott, L. Carvalho, Multivariate varying-coefficient models for an ecological system, Environmetrics: The Official Journal of the International Environmetrics Society 20 (4) (2009) 460–476.

[16] H. Sato, M. C. Fehler, T. Maeda, Seismic wave propagation and scattering in the heterogeneous earth, Vol. 496, Springer, Berlin, Heidelberg, 2012.

[17] M. Farkas, B. Deconinck, Solving the heat equation with variable thermal conductivity, Applied Mathematics Letters 135 (2023) 108395.

[18] T. Han, Z. Chen, S. Guo, W. Xu, W. Ouyang, L. Bai, Climate science data can be compressed efficiently by dual-stage extreme compression with a variational auto-encoder transformer, Communications Earth & Environment 6 (1) (2025) 955.

[19] H. W. Engl, J. Zou, A new approach to convergence rate analysis of tikhonov regularization for parameter identification in heat conduction, Inverse Problems 16 (6) (2000) 1907.

[20] V. Druskin, M. Zaslavsky, On combining model reduction and gauss–newton algorithms for inverse partial differential equation problems, Inverse Problems 23 (4) (2007) 1599.

[21] B. Jin, Fast Bayesian approach for parameter estimation, International Journal for Numerical Methods in Engineering 76 (2) (2008) 230–252.

[22] X. Xun, J. Cao, B. Mallick, A. Maity, R. J. Carroll, Parameter estimation of partial differential equation models, Journal of the American Statistical Association 108 (503) (2013) 1009–1020.

[23] G. Frasso, J. Jaeger, P. Lambert, Parameter estimation and inference in dynamic systems described by linear partial differential equations, AStA Advances in Statistical Analysis 100 (2016) 259–287.

[24] S. Yuan, S. Wang, M. Ma, Y. Ji, L. Deng, Sparse bayesian learning-based time-variant deconvolution, IEEE Transactions on Geoscience and Remote Sensing 55 (11) (2017) 6182–6194.

[25] M. Raissi, P. Perdikaris, G. E. Karniadakis, Physics-informed neural networks: A deep learning framework for solving forward and inverse problems involving nonlinear partial differential equations, Journal of Computational Physics 378 (2019) 686–707.

[26] G. E. Karniadakis, I. G. Kevrekidis, L. Lu, P. Perdikaris, S. Wang, L. Yang, Physics-informed machine learning, Nature Reviews Physics 3 (6) (2021) 422–440.

[27] A. D. Jagtap, K. Kawaguchi, G. E. Karniadakis, Adaptive activation functions accelerate convergence in deep and physics-informed neural networks, Journal of Computational Physics 404 (2020) 109136.

[28] J. Yu, L. Lu, X. Meng, G. E. Karniadakis, Gradient-enhanced physics-informed neural networks for forward and inverse PDE problems, Computer Methods in Applied Mechanics and Engineering 393 (2022) 114823.

[29] W. Zhang, J. Li, Cpinns: A coupled physics-informed neural networks for the closed-loop geothermal system, Computers & Mathematics with Applications 132 (2023) 161–179.

[30] S. Wang, Y. Teng, P. Perdikaris, Understanding and mitigating gradient flow pathologies in physics-informed neural networks, SIAM Journal on Scientific Computing 43 (5) (2021) A3055–A3081.

[31] L. D. McClenny, U. M. Braga-Neto, Self-adaptive physics-informed neural networks, Journal of Computational Physics 474 (2023) 111722.

[32] G. Zhang, H. Yang, G. Pan, Y. Duan, F. Zhu, Y. Chen, Constrained self-adaptive physics-informed neural networks with ResNet block-enhanced network architecture, Mathematics 11 (5) (2023) 1109.

[33] S. J. Anagnostopoulos, J. D. Toscano, N. Stergiopulos, G. E. Karniadakis, Residual-based attention in physics-informed neural networks, Computer Methods in Applied Mechanics and Engineering 421 (2024) 116805.

[34] R. Mattey, S. Ghosh, A novel sequential method to train physics-informed neural networks for Allen-Cahn and Cahn-Hilliard equations, Computer Methods in Applied Mechanics and Engineering 390 (2022) 114474.

[35] Z. Miao, Y. Chen, VC–pinn: Variable coefficient physics-informed neural network for forward and inverse problems of PDEs with variable coefficient, Physica D: Nonlinear Phenomena 456 (2023) 133945.

[36] Z. Dong, P. Polak, Cp-pinns: Data-driven changepoints detection in pdes using online optimized physics-informed neural networks, in: 2024 Conference on AI, Science, Engineering, and Technology, IEEE, 2024, pp. 90–97.

[37] G. Zhang, Y. Duan, G. Pan, Q. Chen, H. Yang, Z. Zhang, Data-driven discovery of state-changes in underlying system from hidden change-points in partial differential equations with spatiotemporal varying coefficients, Journal of Computational and Applied Mathematics (2025) 116962.

[38] C. Wu, M. Zhu, Q. Tan, Y. Kartha, L. Lu, A comprehensive study of non-adaptive and residual-based adaptive sampling for physics-informed neural networks, Computer Methods in Applied Mechanics and Engineering 403 (2023) 115671.

[39] J. Li, Z. Zhang, M. Dai, J. Ming, X. Wang, Diffusion equations with Markovian switching: Well-posedness, numerical generation and parameter inference, Chaos, Solitons & Fractals 171 (2023) 113488.

[40] S. Frühwirth-Schnatter, Finite mixture and Markov switching models, Vol. 425, Springer, New York, NY, 2006.

[41] Y. Yuan, X. Li, L. Li, F. J. Jiang, X. Tang, F. Zhang, J. Goncalves, H. U. Voss, H. Ding, J. Kurths, Machine discovery of partial differential equations from spatiotemporal data: A sparse Bayesian learning framework, Chaos: An Interdisciplinary Journal of Nonlinear Science 33 (11) (2023) 113122.

[42] M. Rasht-Behesht, C. Huber, K. Shukla, G. E. Karniadakis, Physics-informed neural networks (PINNs) for wave propagation and full waveform inversions, Journal of Geophysical Research: Solid Earth 127 (5) (2022) e2021JB023120.

[43] L. Chen, M. Xiong, J. Ming, X. He, Efficient mini-batch stochastic gradient descent with centroidal voronoi tessellation for PDE-constrained optimization under uncertainty, Physica D: Nonlinear Phenomena 467 (2024) 134216.

[44] G. Zhang, G. Pan, I. T. Leong, H. Yang, Z. Xu, Identification of unknown space-varying wavenumber in Helmholtz equation using physics-informed neural networks, in: Fifth International Conference on Artificial Intelligence and Computer Science, Vol. 12803, SPIE, 2023, pp. 973–978.

[45] M. Agarwal, K. K. Rao, K. Vaidya, S. Bhattacharya, ML–MOC: Machine learning (kNN and GMM) based membership determination for open clusters, Monthly Notices of the Royal Astronomical Society 502 (2) (2021) 2582–2599.

[46] S. Chawla, A. Gionis, K-means: A unified approach to clustering and outlier detection, in: Proceedings of the SIAM International Conference on Data Mining, SIAM, 2013, pp. 189–197.

[47] M. Yang, C. Lai, C. Lin, A robust EM clustering algorithm for Gaussian mixture models, Pattern Recognition 45 (11) (2012) 3950–3961.

[48] S. Mukherjee, H. Asnani, E. Lin, S. Kannan, Clustergan: Latent space clustering in generative adversarial networks, in: Proceedings of the AAAI Conference on Artificial Intelligence, Vol. 33, 2019, pp. 4610–4617.

[49] L. Yang, X. Meng, G. E. Karniadakis, B-pinns: Bayesian physics-informed neural networks for forward and inverse PDE problems with noisy data, Journal of Computational Physics 425 (2021) 109913.